TARGETING TUMOUR MICROENVIRONMENT: DEVELOPMENT OF CARBONIC ANHYDRASE IX NUCLEAR IMAGING AGENTS

by

Joseph Cheong Chun Lau

B.Sc., The University of British Columbia, 2011

A THESIS SUBMITTED IN PARTIAL FULFILLMENT OF

THE REQUIREMENTS FOR THE DEGREE OF

DOCTOR OF PHILOSOPHY

in

THE FACULTY OF GRADUATE AND POSTDOCTORAL STUDIES

(Interdisciplinary Oncology)

THE UNIVERSITY OF BRITISH COLUMBIA

(Vancouver)

August 2016

Abstract

Tumour hypoxia has long been recognized as an impediment to radiotherapy and chemotherapy. Cancers that are hypoxic tend to be aggressive, with high propensity for distant metastasis. As hypoxia is a salient feature of most solid cancers, targeting components of the hypoxia-induced signaling cascade has been proposed as a means for oncologic treatment. The key enzyme mediating hypoxia-induced stress response in cancers is carbonic anhydrase IX (CA-IX). Regulated by hypoxia-inducible factor 1α (HIF-1α), CA-IX catalyzes the reversible hydration of carbon dioxide to bicarbonate ion. CA-IX promotes cancer cell survival by transporting bicarbonate ions into the cell to maintain pH homeostasis during glycolysis. CA-IX is well-established as a surrogate marker for cellular hypoxia. Overexpression of CA-IX has been observed in a broad spectrum of cancers including: breast, cervix, ovarian, bladder, brain, colon, lung, kidney, head and neck cancers. In healthy individuals, CA-IX is expressed at low levels except in the gastrointestinal tract where it is involved in the process of cell differentiation. As CA-IX is pathologically expressed by cancer cells and located at the cell surface, it has emerged as a promising imaging/therapeutic target.

In this thesis, we communicate the development of molecular antigen recognition molecules as potential radiotracers for CA-IX targeted nuclear imaging. We identified two classes of sulfonamide derivatives that successfully delineated CA-IX expression in tumour-bearing mice. Isoform selectivity, the major challenge for small molecule inhibitor-based imaging, was achieved via a multivalent approach or by conjugating pharmacophores to polyaminocarboxylate chelators. With good tumour-to-nontarget ratios and fast pharmacokinetics, some of these agents warrant further investigation as surrogate hypoxia imaging agents. Additionally we radiolabeled three novel monoclonal antibodies (mAbs) and one affibody for CA-IX imaging, with one mAb in particular showing significant accumulation in tumours. Collectively, this research provides a non-invasive platform to characterize and quantify expression of CA-IX in primary lesions and across metastatic sites. The diagnostic information can be readily integrated with emergent pharmaceuticals to increase effectiveness and safety of CA-IX or hypoxia-directed treatments for cancer patients.

Preface

A version of Chapter 2 has been published [Pan J, **Lau J**, Mesak F, Hundal N, Pourghiasian M, Liu Z, Bénard F, Dedhar S, Supuran CT, Lin KS. Synthesis and evaluation of ^{18}F-labeled carbonic anhydrase IX inhibitors for imaging with positron emission tomography. J Enzyme Inhib Med Chem, 2014; 29(2):249-255]. Pan J and I were the lead investigators, responsible for all major areas of concept formation, data collection and analysis, as well as the majority of manuscript composition. Mesak F, Hundal N, Pourghiasian M, and Liu Z were involved in radiochemistry and imaging experiments. Supuran CT provided the binding affinity measurements. Bénard F, Dedhar S, Supuran CT, and Lin KS were the supervisory authors on this project and were involved throughout the project in concept formation and manuscript composition.

A version of Chapter 3 has been published [**Lau J**, Pan J, Zhang Z, Hundal N, Liu Z, Bénard F, Lin KS. Synthesis and Evaluation of ^{18}F-Labeled Tertiary Sulfonamides for Imaging Carbonic Anhydrase IX expression in Tumours with Positron Emission Tomography. Bioorg Med Chem Lett, 2014; 24(14):3064-3068]. I was the lead investigator, responsible for all major areas of concept formation, data collection and analysis, as well as the majority of manuscript composition. Pan J, Zhang Z, Hundal N, and Liu Z were involved in radiochemistry and imaging experiments. Bénard F and Lin KS were the supervisory authors on this project and were involved throughout the project in concept formation and manuscript composition.

A version of Chapter 4 has been published [**Lau J**, Liu Z, Lin KS, Pan J, Zhang Z, Vullo D, Supuran CT, Perrin DM, Bénard F. Trimeric Radiofluorinated Sulfonamide Derivatives to Achieve In Vivo Selectivity for Carbonic Anhydrase IX-Targeted Cancer Imaging. J Nuc Med, 2015;56(9): 1434-1440]. Liu Z and I were the lead investigators, responsible for all major areas of concept formation, data collection and analysis, as well as the majority of manuscript composition. Pan J, Zhang Z, and Vullo D were involved in binding affinity and radiochemistry experiments. Lin KS, Supuran CT, Perrin DM, and Bénard F were the supervisory authors on

this project and were involved throughout the project in concept formation and manuscript composition.

A version of Chapter 5 has been published [**Lau J**, Zhang Z, Jenni S, Kuo HT, Liu Z, Vullo D, Supuran CT, Lin KS, Bénard F. ET Imaging of Carbonic Anhydrase IX Expression of HT-29 Tumor Xenograft Mice with ^{68}Ga-Labeled Benzenesulfonamides. Mol Pharm, 2016;13(3): 1137-1146]. Zhang Z and I were the lead investigators, responsible for all major areas of concept formation, data collection and analysis, as well as the majority of manuscript composition. Jenni S, Kuo HT, Liu Z, and Vullo D were involved in binding affinity, radiochemistry, and imaging experiments. Supuran CT, Lin KS, and Bénard F were the supervisory authors on this project and were involved throughout the project in concept formation and manuscript composition.

In Chapter 6, the CA-IX monoclonal antibodies were obtained through a collaboration with Drs. Shoukat Dedhar (BC Cancer Agency), Anne Lenferink (National Research Council), and Maureen O'Connor (National Research Council). Internal names are used for the antibodies. The biological and physical characterizations of the antibodies were performed by Dr. Paul McDonald (Dedhar's Lab).

The research in this thesis was conducted under animal protocols A11-0238 and A11-0185, which were approved by the Institutional Animal Care Committee of the University of British Columbia in compliance with the Canadian Council on Animal Care Guidelines.

Table of Contents

List of Tables

List of Figures

List of Abbreviations and Symbols

%ID/g	Percentage of injected radioactive dose per gram of tissue
α	Alpha particle
β^+	Positron
β^-	Beta particle
γ	Gamma ray
°C	Degrees Celsius
A	Ampere
aa	Amino acid
ABS	4-Aminobenzenesulfonamide
ADC	Antibody-drug conjugate
ADCC	Antibody-dependent cell-mediated cytotoxicity
ADCP	Antibody-dependent cell phagocytosis
AEBS	4-(2-Aminoethyl)benzenesulfonamide
AMP	Adenosine monophosphate
ANOVA	Analysis of variance
Au	Arbitrary unit
AU	Absorbance unit
AZA	Acetazolamide
BCCA	British Columbia Cancer Agency
Bn	Benzyl
Boc	*tert*-Butyloxycarbonyl protecting group
Bq	Becquerel
BRCA1/2	Breast cancer 1/2 gene
CA	Carbonic anhydrase
Calcd	Calculated
cc	Cubic centimeter
CCRCC	Clear cell renal cell carcinoma

CDC	Complement dependent cytotoxicity
$CDCl_3$	Deuterated chloroform
CH_2Cl_2	Dichloromethane
CH_3CN	Acetonitrile
Ci	Curie
Cl^-	Chloride ion
CML	Chronic myeloid leukemia
CO_2	Carbon dioxide
CT	Computed tomography
$CuSO_4$	Copper sulfate
Cys	Cysteine
d	Day
Da	Dalton
DAST	Diethylaminosulfur trifluoride
DCC	*N*,*N*'-Dicyclohexylcarbodiimine
DI	Deionized
DIEA	*N*,*N*-Diisopropylethylamine
Df	Desferrioxamine
DMF	*N*,*N*-Dimethylformamide
DNA	Deoxyribose nucleic acid
DOTA	1,4,7,10-Tetraazacyclododecane-*N*,*N*′,*N*″,*N*‴-tetraacetic acid
DTPA	Diethylenetriaminepentaacetic acid
E-I	Enzyme-Inhibitor
EC	Electron capture
ECOD	7-Ethoxycoumarin O-deethylase
EDC•HCl	*N*-(3-Dimethylaminopropyl)-*N*′-ethylcarbodiimide hydrochloride
EDT	Ethane dithiol
EF5	2-(2-Nitro-1*H*-imidazol-1-yl)-*N*-(2,2,3,3,3-pentafluoropropyl)acetamide
EGF	Epidermal growth factor
EGFR	Epidermal growth factor receptor

ELISA	Enzyme-linked immunosorbent assay
EMT	Epithelial mesenchymal transition
EOS	End of synthesis
EPR	Enhanced permeability and retention
eq	Equivalent
ER	Estrogen receptor
ESI	Electronspray ionization
EtOAc	Ethyl acetate
eV	Electron volt
FAZA	Fluoroazomycin-arabinofuranoside
FEC	7-(2-Fluoroethoxy)coumarin
FDA	The Food and Drug Administration
^{18}F-FDG	2-Deoxy-2-[^{18}F]fluoro-D-glucose
Fe_3O_4	Iron oxide
FMISO	Fluoromisonidazole
Fmoc	Fluorenylmethyloxycarbonyl
g	Gram
GLP	Good laboratory practice
h	Hour
H^+	Hydrogen ion/proton
H_2O	Water
HBTU	3-[Bis(dimethylamino)methyliumyl]-3*H*-benzotriazol-1-oxide hexafluorophosphate
HCl	Hydrochloric acid
HCO_3^-	Bicarbonate ion
He	Helium gas
HEPES	4-(2-Hydroxyethyl)-1-piperazineethanesulfonic acid
HER2	Human epidermal growth factor 2 receptor
HER3	Human epidermal growth factor 3 receptor
HIF-1α/β	Hypoxia-inducible factor 1 alpha/beta

HIF-2α	Hypoxia-inducible factor 2 alpha
HF	Hydrogen fluoride
HOBt	Hydroxybenzotriazole
HPLC	High performance liquid chromatography
HRE	Hypoxia response element
HRP	Horseradish peroxidase
HX4	Flortanidazole
i.v.	Intravenous
IC_{50}	Half maximal inhibitory concentration
IHC	Immunohistochemistry
IGF-1R	Insulin-like growth factor 1 receptor
IgG	Immunoglobulin
IND	Investigational New Drug
IRW	Inveon Research Workplace software
IT	Isomeric transition
K_{222}	Kryptofix 222
K_i	Inhibition constant
K_d	Dissociation constant
K_2CO_3	Potassium carbonate
L	Litre
LET	Linear energy transfer
$LogD_{7.4}$	Log value of distribution coefficient at pH 7.4,
M	Molar concentration
m	Meter
m/z	Mass-to-charge ratio
mAb	Monoclonal antibody
MAG3	Mercaptoacetyltriglycine
MBHA	4-Methylbenzhydrylamine
MeOH	Methanol
MIBG	Metaiodobenzylguanidine

min	Minute
$MgSO_4$	Magnesium sulfate
mmHg	Millimeter of mercury
mol	Mole
mp	Melting point
MR	Magnetic resonance
MTT	Molecular targeted therapies
MW	Molecular weight
N_2	Nitrogen gas
Na^+	Sodium ion
$NaBH_4$	Sodium borohydride
NaCl	Sodium chloride
$NaHCO_3$	Sodium bicarbonate
NaH_2PO_4	Monosodium phosphate
NaI	Sodium iodide
NaN_3	Sodium azide
NaOH	Sodium hydroxide
Na_2CO_3	Sodium carbonate
Na_2HPO_4	Disodium phosphate
NH_4OH	Ammonium hydroxide
NHS	*N*-Hydroxysuccinimde
NMR	Nuclear magnetic resonance
NOTA	1,4,7-Triazacyclononane-1,4,7-trisacetic acid
NOTGA	1,4,7-Triazacyclononane-1,4,7-tris-(glutaric acid)
NIR	Near-infrared
NRC	National Research Council
NSCLC	Non-small cell lung carcinoma
NSG	NOD.Cg-*Prkdc*^{scid} *Il2rg*^{tm1Wjl}/SzJ
PBS	Phosphate-buffered saline
Pd/C	Palladium on carbon

PDGFRβ	Beta-type platelet-derived growth factor receptor
PDX	Patient derived xenograft
PET	Positron emission tomography
PG	Proteoglycan-like
pH_i	Intracellular pH
p.i.	Post-injection
PI3K	Phosphoinositide 3-kinase
PKA	Protein kinase A
pO_2	Partial pressure of oxygen
ROI	Region of interest
rpm	Revolutions per minute
s	Second
SbF_5	Antimony pentafluoride
SCN	Isothiocyanate
SD	Standard deviation
SEC	Size-exclusion column
SPECT	Single photon emission computed tomography
$t_{1/2}$	Physical half-life
t_R	Retention time
TBAF	Tetrabutylammonium fluoride
$TBAHCO_3$	Tetrabutylammonium bicarbonate
TCEP	Tris(2-carboxyethyl)phosphine hydrochloride
TFA	Trifluoroacetic acid
THF	Tetrahydrofuran
TIS	Triisopropylsilane
TMA	Trimethylamine
TNFα	Tumour necrosis factor alpha
TOF	Time of flight
UBC	University of British Columbia
UV	Ultraviolet

VEGF	Vascular endothelial growth factor
VHL	von Hippel-Lindau gene
WHO	World Health Organization

Acknowledgements

I would like to thank my supervisor Dr. François Bénard for his guidance and support during my research. Thank you for believing in me, and giving me the academic freedom to pursue my research interests. I was constantly inspired by your passion and sagacity for cancer research. You hold your students to the highest standard and I thank you for always demanding the best of me.

My sincerest gratitude to the members of my supervisory committee: Drs. Kuo-Shyan Lin, Paul Schaffer, and Urs Hafeli. Thank you for enriching my understanding of nuclear medicine, and providing me with research and career advice. Special thanks to Dr. Samuel Aparicio for introducing me to medical research as a Co-op student, and encouraging me to pursue a graduate degree. I would like to thank all past and present members of the Bénard (NH, NC, MP, GMD, HL, ID, GA, MC, FM, SJ, HM, KS, JZ, CCZ, JR, PT, JG, MV, WE, and JK) and Lin (JP, ZZ, HTK, and SP) labs. Without your support and camaraderie, this project would not have been successful.

I would like to acknowledge our collaborators, Drs. Shoukat Dedhar, Claudiu T. Supuran and David M. Perrin, Anne Lenferink, Maureen O'Connor, and generous scholarship support from the Canadian Institutes of Health Research Frederick Banting and Charles Best Canada Graduate Scholarship Doctoral Award, the University of British Columbia Four Year Doctoral Fellowship, and the RIX Family Leading Edge Student Award.

The research presented in this thesis was funded by the following granting agencies: Canadian Institutes of Health Research, Canadian Cancer Society Research Institute, BC Cancer Foundation, and BC Leading Edge Endowment Fund.

Finally, my deepest thanks to my friends and family for their unwavering love and support throughout my years of education. Thank you for all of your sacrifices.

Dedication

To my parents, Anne Lau and James Lau.

Chapter 1: Introduction

1.1 Nuclear Imaging

Nuclear imaging modalities like positron emission tomography (PET) and single photon emission tomography (SPECT) enable the visualization of pathological processes at high resolution in real time[1, 2]. Both modalities use radioactive biomolecules (small molecule inhibitors, peptides, antibodies, antibody mimetics etc.) as imaging agents to offer high sensitivity and quantification capabilities[2]. Depending on the imaging agent administered, PET and SPECT can be used to annotate drug target expression, or to understand biological mechanisms that underlie different disease states. In combination with either computed tomography (CT) or magnetic resonance (MR) to increase anatomic resolution or soft tissue contrast respectively, PET plays an increasingly important role in cancer diagnosis and management[3]. Functional imaging is particularly useful in the case of recurrent or metastatic cancer, where biopsies may be scarce or unavailable. Given that inter- and intra-tumoural heterogeneity can significantly affect potential response to treatment, the ability to systemically characterize primary and metastatic lesions can improve patient outcomes. Figure 1.1 shows the two preclinical nuclear imaging systems used in this thesis, while Table 1.1 is a list of commonly used radioisotopes for imaging applications.

Figure 1.1 MicroPET and microSPECT scanners used for preclinical imaging studies at the BC Cancer Research Centre. Left: Inveon PET/CT scanner with 1.3 mm spatial resolution. Right: MiLabs USPECT/CT II scanner with 0.4 mm spatial resolution. Of note, preclinical SPECT scanners have better spatial resolution than their clinical counterparts due to the use of highly focused multipinhole collimators.

Table 1.1 Properties of common nuclear imaging radioisotopes. Adapted with permissions from Fani and Maecke[4], and Holland *et al*.[5]

Isotope	$t_{1/2}$	Decay mode (%)	E_γ or $E_{\beta+}$ (keV) (%)	Production method
SPECT			**E_γ**	
^{67}Ga	3.26 d	EC (100)	93 (39)	Cyclotron
		Auger, γ	184 (21)	
			300 (17)	
^{99m}Tc	6.02 h	IT (100), γ	141 (91)	^{99}Mo/^{99m}Tc generator
^{111}In	2.80 d	EC (100)	171 (90)	Cyclotron
		Auger, γ	245 (94)	
^{123}I	13.2 h	EC (100), γ	159 (84)	Cyclotron
			27 (71)	
			31 (16)	
PET			**$E_{\beta+}$**	
^{11}C	20.4 min	β^+ (100)	961 (100)	Cyclotron
^{13}N	9.97 min	β^+ (100)	1198 (100)	Cyclotron
^{15}O	2.04 min	β^+ (100)	1735 (100)	Cyclotron
^{18}F	1.83 h	β^+ (97)	634 (97)	Cyclotron
		EC (3)		
^{64}Cu	12.7 h	β^+ (19)	656 (18)	Cyclotron
		β^- (40)		
		EC (41)		
^{68}Ga	1.13 h	β^+ (89)	1899 (88)	^{68}Ge/^{68}Ga generator
		EC (11)		
^{89}Zr	3.27 d	β^+ (23)	908 (23)	Cyclotron
		EC (76)		
^{124}I	4.18 d	β^+ (23)	1314 (7)	Cyclotron
		EC (77)	1409 (14)	
			1474 (9)	
			1545 (6)	
			1988 (4)	
			2242 (13)	
			3160 (24)	
			2556 (25)	
			2137 (11)	
			1535 (12)	
			866 (11)	

β^+ decay is accompanied by 511 keV annihilation gamma radiation
EC = electron capture; IT = isomeric transition

1.1.1 Single Photon Emission Computed Tomography

SPECT imaging is performed by administrating a gamma-emitting radioisotope into a patient, usually by an intravenous injection[2, 6]. The radioactive decay of the radionuclide emits single non-directional photons that are detected by gamma cameras. The detected signals are reconstructed using computer algorithms to generate 2D projections or 3D data sets. SPECT is widely used clinically due to the availability of ^{99m}Tc (^{99}Mo/^{99m}Tc generators), an isotope used in over 80% of nuclear medicine procedures[7]. SPECT instruments have a large clinical base and are used routinely for procedures such as bone scans (^{99m}Tc-methyl disphosponate)[8, 9], myocardial perfusion imaging (^{99m}Tc-tetrofosmin or ^{99m}Tc-sestamibi)[10-12], and functional brain imaging (^{99m}Tc-exametazime)[13]. Since single photon emitters are non-directional, lead collimators are used in clinical instruments to block emissions that are not perpendicular to the detector. This leads to lower sensitivity and relatively poor spatial resolution, which reduces the detection rate of small tumours. However, SPECT remains a viable option for imaging selected cancers. For example, ^{123}I-metaiodobenzylguanidine (^{123}I-MIBG) is an iodinated norepinephrine analogue that targets the norepinephrine transporters[14]. An ^{123}I-MIBG scan is a highly specific test used to detect neuroectodermally derived tumours like pheochromocytoma, ganglioneuroma, ganglioneuroblastoma, paraganglioma, carcinoid tumour and neuroblastoma[15]. With continued improvement in collimation technologies, image reconstruction and processing methods, SPECT may soon have an expanded role in cancer management[6].

1.1.2 Positron Emission Tomography

PET imaging adheres to similar principles to SPECT, with the main difference being the utilization of positron emitters instead of single photon emitters[2]. Positron particles (β^+, anti-electrons) are emitted upon decay, and travel a short distance before interacting with electrons[2]. An interaction event leads to the annihilation of both a positron and an electron, and produces two 511 keV photons ejected at almost exactly 180° apart[2]. Simultaneous detection of these two photons enables the instrument to replace physical collimation with coincidence detection, greatly enhancing spatial resolution and sensitivity[2]. The paired coincidence events are used for image reconstruction to localize the source of β^+ emission in the patient[2]. Compared to SPECT instruments, clinical PET scanners are more sensitive, and produce higher contrast images,

leading to improved diagnostic accuracy[2]. Commonly used PET isotopes include ^{11}C ($t_{1/2}$: 20.4 min), ^{18}F ($t_{1/2}$: 1.83 h), ^{68}Ga ($t_{1/2}$: 1.13 h). ^{64}Cu ($t_{1/2}$: 12.7 h), ^{124}I ($t_{1/2}$: 4.18 d), ^{89}Zr ($t_{1/2}$: 3.27 d). ^{18}F is the most popular PET isotope due to its ease of production via a medical cyclotron, and the widespread use of ^{18}F-FDG for cancer assessment. ^{68}Ga is obtained from commercially available $^{68}Ge/^{68}Ga$ generator. Together with ^{64}Cu, these isotopes are commonly used for radiolabeling peptide derivatives/small molecules for cancer imaging. With relatively long half-lives, ^{89}Zr and ^{124}I are mainly used for labeling monoclonal antibodies that have long circulation times.

1.1.2.1 Cancer Patient Management with PET

PET has a significant role in cancer management including diagnosis and staging, treatment planning, and treatment monitoring. PET is widely considered as a cost-effective diagnostic modality for many cancers including lung cancer, colorectal cancer, and lymphomas[16]. In a large prospective study (22975 scans at 1178 centers in USA), Hillner *et al.* reported that PET imaging changed the intended patient management in > 36.5% of all cases[17]. A change in management strategy is defined as a change in intended treatment (ex. from surgery to chemotherapy) or in treatment intent (ex. from curative to palliative). Up to 70% of the patients were able to avoid invasive surgical procedures after imaging[17]. While the primary objective of a PET scan is to facilitate informed decision making by patients and oncologists, this does not always result in improved outcomes. Patient outcomes are mostly predicated on the efficacy of available therapeutic options, and there are situations where the best medical course for a patient is palliative care.

In Canada, there are currently 45 publicly funded PET scanners in 34 centers across the ten provinces[18]. Based on a national report, 62668 PET scans were performed from 2011 to 2012[18]. The primary application for PET is oncology, with selected provinces offering scanning services for cardiology and neurology[18]. Our institution, the British Columbia Cancer Agency (BCCA), houses 2 clinical scanners and is funded to perform a total of 7775 scans per year. The demand and utilization for PET/CT is expected to grow with the continually increasing cancer incidence rates.

1.1.2.2 ^{18}F-FDG Imaging

The uptake mechanism of ^{18}F-FDG is based on the enhanced metabolic and glycolytic rates of malignant tumours (Warburg effect)[19, 20]. As a glucose analogue, ^{18}F-FDG is taken up by cells via glucose transporters and phosphorylated by hexokinase to form ^{18}F-FDG-6-phosphate. Unable to be further catabolized, ^{18}F-FDG-6-phosphate becomes metabolically trapped inside the cell and provides the signal for image acquisition[21]. Although ^{18}F-FDG is considered the gold standard for cancer imaging, it is not a cancer-specific agent[22]. ^{18}F-FDG uptake has been described in hypermetabolic brown adipose-tissues[23], as well as in non-neoplastic inflammatory processes like sarcoidosis, fungal infections, and tuberculosis[24-26]. Tumours with low glucose metabolism, such as prostate cancer, low-grade sarcomas, low-grade non-Hodgkin's lymphomas, and lobular breast carcinoma, may also have low avidity for ^{18}F-FDG (Figure 1.2)[27]. The latter serves as an impetus to develop novel radiopharmaceuticals to target cancers when ^{18}F-FDG imaging is insufficient for addressing clinical needs.

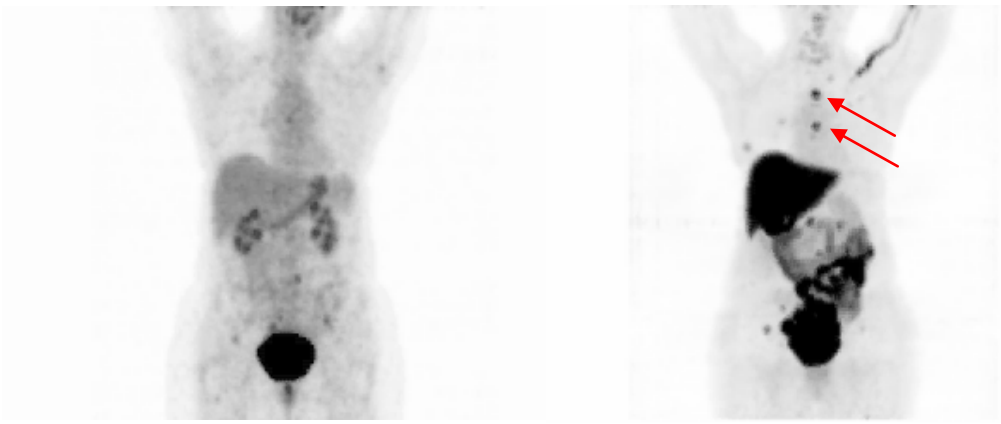

Figure 1.2 Breast cancer PET imaging with ^{18}F-FDG and ^{18}F-fluoroestradiol. A patient suspected of recurrent breast cancer that underwent ^{18}F-FDG (left) and ^{18}F-fluoroestradiol (right) imaging. The scans identified ER positive metastatic mediastinal lymph nodes, indicated by red arrows, which were non-FDG avid. This case study shows how PET allows for molecular correlation and scientific hypothesis generation. Images courtesy of Dr. François Bénard (BCCA).

1.1.3 Role of Functional Imaging in Personalized Cancer Medicine

Personalized cancer medicine is a medical model that seeks to provide intervention, treatment, and care based on individual patient profiles[28, 29]. Conventional cancer treatment

focuses on factors such as age, familial history, tumour stage, nodal status, histological subtype and hormonal status[28, 29]. This treatment model fails to account for the genetic aberrations and molecular mechanisms that drive the complex phenotypes of cancer[30, 31]. The advent of molecular profiling techniques like next generation DNA sequencing, transcriptome analysis, proteome analysis, and metabolic assays, has provided tools to investigate the complex biology underpinning cancer[30, 31]. Germline mutations in genes may predispose individuals to specific cancers. For example, females with *BRCA1/2* mutations have greater a risk of developing familial breast and ovarian cancer[32]. With personalized cancer medicine, at risk individuals may elect to have prophylactic mastectomy or oophorectomy[33]. Another extension of personalized cancer medicine is molecular targeted therapies (MTT). MTT specifically targets molecules or pathways that promote tumourigenesis and tumour growth[34], and is best exemplified by the success of imatinib for chronic myeloid leukemia (CML) patients[35-37]. Patients diagnosed with CML are screened for reciprocal translocation between chromosomes 9 and 22. This genomic rearrangement known as the Philadelphia chromosome results in the expression of BCR-Abl, an oncofusion protein found exclusively in malignant cells and is inhibited by imatinib[35-37]. Continued research has led to the FDA approval and clinical adoption of an assortment of MTT regimens for cancer[38].

So how does functional imaging fit with personalized cancer medicine? The non-invasive assessment of drug target expression across multiple sites assists physicians to select the most effective therapy based on the unique molecular properties of the tumour and the genetic makeup of the patient[39]. Functional imaging can be used to distinguish potential responders from non-responders. This stratification prevents patients from receiving ineffective treatments and expedites the allocation of medical resources. In addition to established regimens, functional imaging can be used to accelerate the drug development process. PET or SPECT imaging can be used to determine the pharmacokinetic (distribution, metabolism, and excretion) behaviour of a prospective drug, assuming a radiolabeled derivative is available[40]. In other cases, ^{18}F-FDG imaging can be used as a clinical endpoint to assess the efficacy of new drugs compared to current standards of care[40].

1.2 Cancer and Tumour Microenvironment

Cancer is a complex multifactorial disease. According to Hanahan and Weinberg, cells acquire biological attributes or hallmarks through genomic instability that potentiates incipient lesions to develop into full frank tumours[30, 31]. These hallmarks include sustained proliferation, desensitization to growth suppressors, apoptotic evasion, replicative immortality, angiogenesis promotion, and invasion and metastasis[30]. In 2011, two additional hallmarks were postulated: reprogramming of energy metabolism and immune system evasion[31]. Adding to the biological complexity is the dynamic tumour microenvironment which can exert selection pressures[41]. The tumour microenvironment can be divided into cellular and non-cellular components. The cellular component is made up of stromal cells (endothelial cells, pericytes, inflammatory cells and fibroblasts)[42], while the non-cellular component include gradients in nutrients, waste, signalling molecules, pH and hypoxia[43, 44].

1.2.1 Hypoxia

Hypoxia arises when oxygen supply is insufficient to meet the metabolic demands of a growing tumour[45]. Hypoxia can be classified as perfusion limited (acute hypoxia) or diffusion limited (chronic hypoxia)[46]. All solid tumours are susceptible to developing hypoxia, and this process is independent of tumour size, stage, grade, or histology[46]. According to Bennewith and Dedhar, the population of cells in a tumour that is exposed to low oxygen tension (pO_2 value < 10 mmHg, eq. to < 1.3% O_2 in vitro) can vary substantially from < 1% to > 50%[47]. Tumours that are hypoxic tend to be highly aggressive with enhanced propensity for metastasis[47]. Hypoxia has been well-studied because its negative effect on radiotherapy and chemotherapy.

In radiotherapy, radiolysis of water produces free radicals that induce DNA damage in cancer cells[48, 49]. Molecular oxygen reacts with damaged DNA to make damage less repairable[50, 51]. Gray *et al.* described that an approximate three-fold higher radiation dose is required to kill oxygen-deprived cells than well-oxygenated cells[52]. In chemotherapy, tumour vasculature or lack thereof limits the delivery and extravascular distribution of anti-cancer drugs[53]. Hypoxic tumours often upregulate drug efflux pumps like P-glycoprotein and multidrug resistance protein 1 to further reduce drug accumulation[54]. Tumour cells also adapt to low oxygen availability by reducing their growth rates. This confers resistance and insensitivity to chemotherapeutic drugs

that are anti-proliferation agents[55]. As hypoxia is a salient feature of most solid cancers, targeting components of the hypoxia-induced signaling cascade has been proposed as a means for oncologic treatment[56, 57].

1.2.1.1 Methods for Detection of Tumour Hypoxia

At present, oxygen electrodes are considered the gold standard for measuring hypoxia as they provide direct measurement of pO_2 level in tissues[58]. However, the sampling procedure is invasive and restricted to superficial or readily accessible tumours[59]. This methodology is further limited in the fact that it cannot differentiate between necrotic and hypoxic tissues[59]. In the past two decades, technological development for the detection of hypoxia has focused on the use of non-invasive imaging modalities like PET[59].

Many of the hypoxia PET imaging agents are based on fluorinated nitroimidazole analogues such as FMISO, FAZA, EF5 and HX4 (Figure 1.3)[55, 59, 60]. These tracers enter cells by passive diffusion and undergo reduction via a one-electron-transfer reaction to form reactive intermediate species[55, 59, 60]. Under normoxia this process is reversed as the nitro-radical anion is re-oxidized to reform the parent 2-nitroimidazole derivative, at which point the tracer can permeate out of the cell[55, 59, 60]. In hypoxic conditions, the nitro-radical anion is further reduced into metabolites that can bind to macromolecules like protein or DNA[55, 59, 60]. This intracellular trapping mechanism leads to accumulation of radioactivity within hypoxic cells[55, 59, 60]. Of the tracers mentioned, ^{18}F-FMISO is the tracer that has been utilized most extensively in the clinic[59]. However ^{18}F-FMISO is not used routinely due to its pharmacokinetic profile with slow clearance from normal tissues[59, 60]. Consequently, ^{18}F-FMISO often yields images with modest contrast. For example, Rajendran *et al.* used a tumour to background ratio of 1.2 at 2 h p.i. as a cut-off for defining tumour hypoxia with ^{18}F-FMISO in a cohort of sarcoma patients[61]. Novel hypoxia PET tracers with higher sensitivity and faster pharmacokinetic are needed to improve treatment planning and prognostic accuracy.

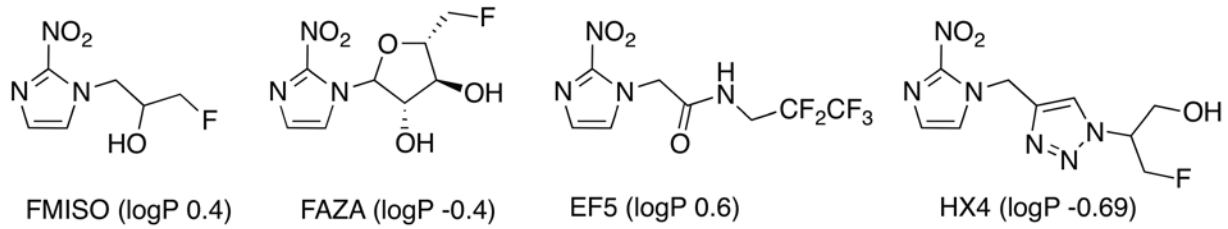

FMISO (logP 0.4) FAZA (logP -0.4) EF5 (logP 0.6) HX4 (logP -0.69)

Figure 1.3 Molecular structures of four commonly used ^{18}F-labeled hypoxia PET tracers in the clinic. These hypoxia tracers are 2-nitroimidazole derivatives and vary in their lipophilicity. Figure was adapted from Fleming *et al.*[59]

1.3 Carbonic Anhydrase IX as a Surrogate Marker of Hypoxia

To cope with stress associated with a hypoxic microenvironment, cancer cells undergo substantial gene expression changes. The hypoxia-inducible factor (HIF) family of transcription factors act as the principal regulators of this homeostatic response[57, 62]. Under hypoxia, HIF-1α is translocated into the nucleus where it binds to the constitutively expressed HIF-1β subunit to form a heterodimer[63]. The HIF-1α/β complex binds to hypoxia-response elements (HREs) within the promoter sequences of target genes, and recruits transcriptional co-activators to promote transcription (Figure 1.4)[63]. Depending on which genes are activated by HIF-1α, there is a wide range of biological responses that can occur including angiogenesis, erythropoiesis, apoptosis, cell proliferation and survival, proteolysis, pH homeostasis, and glucose metabolism[63].

Carbonic anhydrase IX (CA-IX) is the protein that is most strongly upregulated by hypoxia and HIF-1α[64]. Initially termed MN-protein, CA-IX was first identified by Pasterokova *et al.* as a membrane surface protein expressed in HeLa human cervical carcinoma cell line[65, 66]. As a member of the α-family of carbonic anhydrases, CA-IX is 1 of 15 unique but closely related zinc metalloenzymes (Table 1.2)[67]. Of the different isoforms, the expression of CA-IX is most strongly associated with cancer progression. In fact, CA-IX mediates several physiological responses within the hypoxic milieu of solid tumours (Section 1.3.2). CA-IX has a biological half-life of approximately 38 h in re-oxygenated cells[68], which raises concerns whether CA-IX can reliably infer hypoxia status without overestimating hypoxic fractions. By comparison, the time required for oxygen-dependent degradation of HIF-1α has been reported to be between 5-8 min[69]. According to Kulaz *et al.*, CA-IX expression reflects the transcriptional activity of HIF-1α, as opposed to the abundance of HIF-1α[70]. Indeed discordant expression between CA-IX and

HIF-1α has been described in vivo; however, CA-IX is still considered one of the most sensitive endogenous marker for cellular hypoxia[70]. Many research groups use CA-IX as an endogenous biomarker to complement pimonidazole staining to validate hypoxia status in tumours[71, 72]. It should be noted that there are scenarios where CA-IX may not be expressed under hypoxia. Mutations in HIF-1α leading to a loss of function has been previously described in cell lines[73], and there are certain cancers that preferentially express HIF-2α and HIF-2α-targeted genes[74, 75].

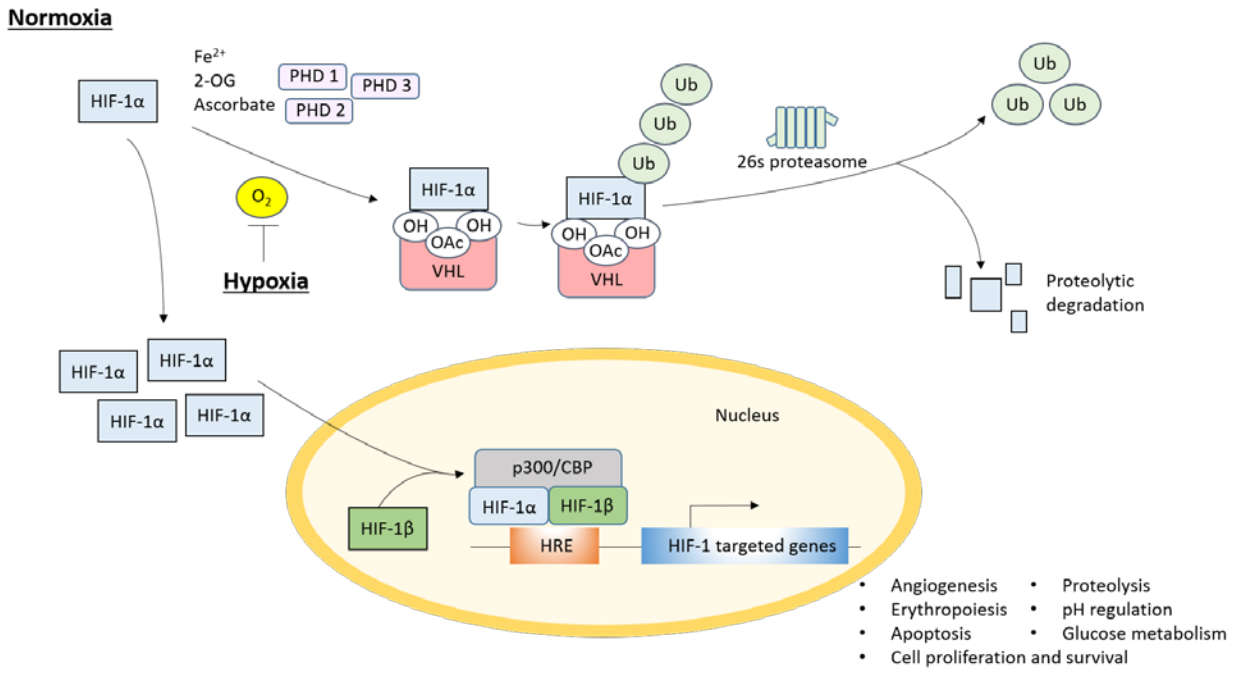

Figure 1.4 Regulation of HIF-1α by proline hydroxylation. Under normoxic conditions with O_2, Fe^{2+}, 2-oxoglutarate (2-OG) and ascorbate present, hypoxia-inducible factor (HIF)-1α is hydroxylated by proline hydroxylases (PHD1, 2 and 3). Hydroxylated HIF-1α becomes a binding partner of pVHL (von Hippel-Lindau tumour suppressor protein). The pVHL/HIF-1α complex is poly-ubiquitinated and targeted for degradation by proteasomes. In addition to hydroxylation (OH), HIF-1α can undergo acetylation (OAc) to facilitate pVHL binding. Under hypoxic conditions, HIF-1α hydroxylation is inhibited and HIF-1α accumulates in the cytosol. HIF-1α is translocated into the nucleus where it forms a heterodimer with HIF-1β. The HIF-1α/β heterodimer binds to hypoxia-response elements (HREs) within the promoter sequences of the target genes and recruits transcriptional co-activators (ex. p300/CREB binding protein) to enable transcription. As indicated, HIF-1α regulated genes mediate many cellular functions. Figure was adapted from Carroll and Ashcroft[63] with permission.

Table 1.2 Organ/tissue distribution, subcellular localization, CO_2 hydrase activity, and affinity for sulfonamides of the 15 human carbonic anhydrases. Table is adapted with permission from Alterio *et al.* [67] Copyright (2012) American Chemical Society.

Isoform	Organ/tissue distribution	Subcellular location	Catalytic activity (CO_2 hydration)	Affinity for sulfonamides
CA-I	erythrocytes, gastrointestinal tract, eye	cytosol	Low	medium
CA-II	erythrocytes, eye, gastrointestinal tract, bone osteoclasts, kidney, lung, testis, brain	cytosol	high	very high
CA-III	skeletal muscle, adipocytes	cytosol	very low	very low
CA-IV	kidney, lung, pancreas, brain capillaries, colon, heart muscle, eye	membrane-bound	medium	high
CA-VA	liver	mitochondria	Low	high
CA-VB	heart and skeletal muscle, pancreas, kidney, spinal cord, gastrointestinal tract	mitochondria	high	high
CA-VI	salivary and mammary glands	secreted into saliva and milk	Low	very high
CA-VII	central nervous system	cytosol	high	very high
CA-VIII	central nervous system	cytosol	acatalytic	ND[a]
CA-IX	**tumours, gastrointestinal mucosa**	**transmembrane**	**high**	**high**
CA-X	central nervous system	cytosol	acatalytic	ND[a]
CA-XI	central nervous system	cytosol	acatalytic	ND[a]
CA-XII	kidney, intestine, reproductive epithelia, eye, tumours	transmembrane	Low	very high
CA-XIII	kidney, brain, lung, gut, reproductive tract	cytosol	Low	high
CA-XIV	kidney, brain, liver, eye	transmembrane	Low	high

[a]ND = not determined.

1.3.1 Biochemical Structure of CA-IX

CA-IX is made up of 459 amino acids (aa), which comprises 5 different protein domains (Figure 1.5)[76]. The domains are classified as signal peptide domain, proteoglycan (PG)-like domain, catalytic domain, transmembrane domain, and intracellular domain, with each mediating different biological functions[76]. During protein maturation, the *N*-terminus signal peptide is truncated leaving the PG-like domain (59 aa) and catalytic domain (257 aa) to form the ectodomain[76]. The catalytic domain is highly conserved amongst the CA family[77], but the adjacent PG-like domain is unique to CA-IX and serves as a potential allosteric binding site (Section 1.3.2.2)[76]. CA-IX is localized at the cell surface, in a homodimer configuration[77].

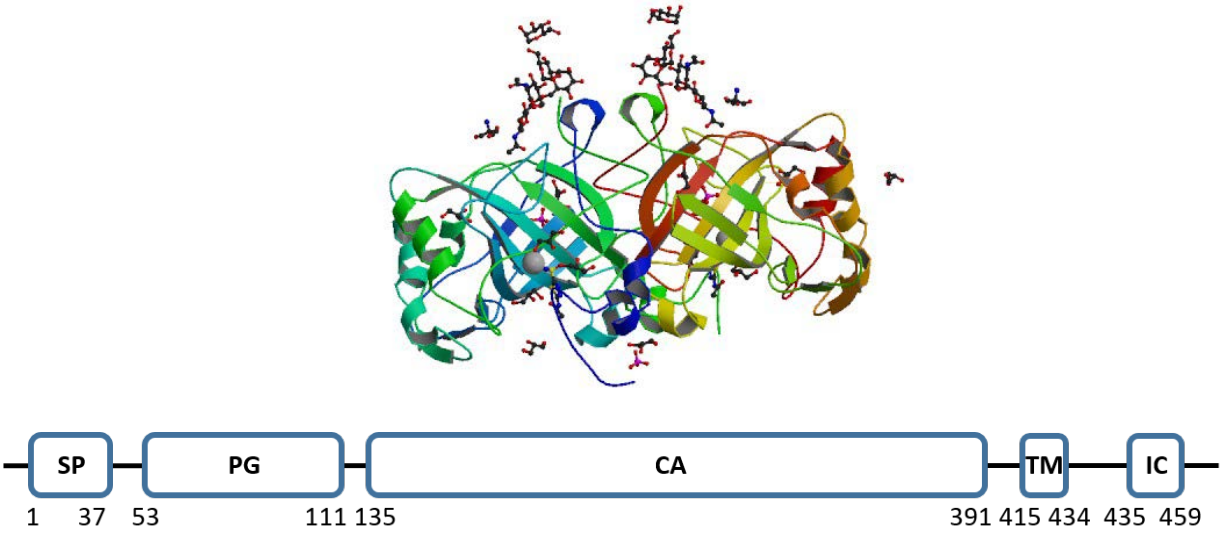

Figure 1.5 Crystal structure of the catalytic domain of CA-IX. Top: CA-IX forms an intermolecular disulfide bridge with another CA-IX subunit, and is observed as a homodimer at the cell surface. The crystal structure of the catalytic pocket was resolved by Alterio *et al.*[77], and is used to guide the design of CA-IX inhibitors (Protein Data Bank ID: 3IAI). Bottom: a schematic representation of the 5 protein domains of CA-IX. SP: signal protein, PG: proteoglycan-like, CA: catalytic, TM: transmembrane, IC: intracellular.

1.3.2 Physiological Function of CA-IX in Cancer

1.3.2.1 Intracellular pH Regulation and Survival

As oxidative phosphorylation is restricted under hypoxic conditions, HIF-1α activated tumour cells adapt by engaging in glycolysis for catabolism[42, 43]. Glycolysis offers a selective

advantage for cancer cells as byproducts can participate in downstream anabolic pathways[78, 79]. However, this glycolytic switch also produces acidic metabolites that lower intracellular pH (pH_i). Disruption of pH_i negatively impacts biological processes including membrane stability, proliferation, and metabolism[80]. CA-IX is part of the cellular machinery that maintains pH_i homeostasis[81-84]. Like other CA isoforms, CA-IX is an efficient catalyst for the reversible hydration of carbon dioxide to bicarbonate ion and proton ($H_2O + CO_2 \leftrightarrow HCO_3^- + H^+$)[81-84]. HCO_3^- ions are subsequently brought into the cell by transporter systems (ex. Na^+/ HCO_3^- cotransporter, Na^+ dependent Cl^-/ HCO_3^- exchanger, anion exchanger) to maintain an alkaline pH_i[80]. Attenuation of CA-IX activity within hypoxic niches by either small molecule inhibitors or RNA interference has been shown to reduce cell survival and proliferation[85].

1.3.2.2 Cell Adhesion, Migration, Invasion, and Metastasis

CA-IX is involved in the processes of cell adhesion, migration, invasion, and metastasis. It has been reported that CA-IX binds competitively to β-catenin via its PG-like domain, to modulate E-cadherin-mediated adherent junctions between cells[86]. By interfering with E-cadherin/β-catenin binding, CA-IX destabilizes cell-cell adhesions and promotes cell motility[86]. Cytoskeletal rearrangement occurs, followed by cellular detachment. The increase in migratory capability contributes to epithelial-mesenchymal transition (EMT) and metastasis[87]. CA-IX further initiates the metastatic cascade by acidifying the extracellular environment. In the process of converting CO_2 into HCO_3^-, CA-IX generates H^+ that can degrade the extracellular matrix and activate matrix metalloproteinases[88, 89]. Pharmacological inhibition of CA-IX has been shown by our collaborator, Dr. Shoukat Dedhar (BCCA), to obviate pulmonary metastasis in an aggressive preclinical breast cancer model[85].

1.3.3 Regulation of CA-IX Activity and Abundance

Studies have revealed that the intracellular domain of CA-IX is critical for enzymatic activity[90-92]. There are three aa residues (^{443}T, ^{448}S, and ^{449}Y) that serve as potential phosphorylation sites for protein interaction and signal transduction. Under hypoxia, cyclic-AMP activates PKA kinase which phosphorylates ^{443}T to increase CA-IX activity[91]. On the other hand, ^{449}Y phosphorylation is mediated by epidermal growth factor (EGF) and allows

CA-IX to interact with PI3K to activate Akt signaling in a positive feedback loop[92]. As for ^{448}S, its phosphorylation is considered a negative regulator for CA-IX activity[65].

A manner in which CA-IX abundance is regulated is through metalloproteinase-mediated cleavage of the extracellular domain. This cleavage, also called ectodomain shedding, can be carried out passively or actively by a TNFα-converting enzyme (TACE/ADAM17)[93]. Elevated levels of CA-IX in serum have been reported in renal, vulvar, and breast cancer patients[94-96], presumably as a result of ectodomain shedding. It is hypothesized that this process correlates with tumour burden in patients, and mediates autocrine and paracrine signaling at the cellular level. A recent preclinical study has shown that circulating CA-IX ectodomain can be an indicator of apoptosis in response to cytotoxic drugs[97]. It is plausible that this process can negatively impact therapy and imaging, as the accumulation of ectodomain in circulation may divert CA-IX targeting agents away from tumour sites[98].

1.3.4 Distribution of CA-IX in Normal Tissues and Malignancies

In normal physiological conditions, CA-IX expression is generally restricted to the gastrointestinal tract (duodenum, jejunum and ileum) where it is involved in the process of differentiation[99]. Diffuse expression of CA-IX has also been observed in male efferent epithelial ducts[100], and in the basolateral membrane of acinar and ductal epithelia of the pancreas[101]. In malignancies, overexpression of CA-IX has been observed in a broad spectrum of cancers including: breast, lung, colon, cervix, ovary, head and neck, bladder, and renal cancers[85, 102-113]. Several tumour microarray studies (Table 1.3) performed with IHC staining have shown that CA-IX expression is correlated with poor prognosis. CA-IX positivity and staining intensity depend on the tumour subtype being investigated. CA-IX staining is generally regional as opposed to a ubiquitous distribution. The pathological expression of CA-IX complemented with a limited profile in normal tissues makes it an attractive therapeutic target.

Table 1.3 CA-IX tissue microarray studies. Table reproduced from McDonald *et al*.[56]

Cancer subtype	# of Samples	Total CA-IX +ve %	Prognostic marker						Ref
			Univariate analysis			Multivariate analysis			
			DSS	OS	MFS	DSS	OS	MFS	
Breast	3630	16	Yes	NR	Yes	Yes	Yes	Yes	[85]
Breast	144	26	NR	Yes	NR	NR	Yes	NR	[114]
NSCLC	555	24	Yes	Yes	NR	Yes	NS	NR	[103]
Ovarian	205	26	NR	Yes	NR	NR	Yes	NR	[108]
Bladder	340	71	NR	Yes	NR	NR	Yes	NR	[111]
Astrocytoma	362	78	NR	Yes	NR	NR	Yes	NR	[115]

DSS = disease specific survival; OS = overall survival; MFS = metastasis free survival; NSCLC = non-small cell lung carcinoma; NS = not significant; NR = not reported

1.3.5 Tumour Models Used for CA-IX Imaging

Although the pathological role of CA-IX has been studied in many cancer subtypes, two human cancer models are used extensively in preclinical studies for the development of CA-IX imaging agents. They are the HT-29 colorectal adenocarcinoma cell line and the SK-RC-52 clear cell renal cell carcinoma (CCRCC) cell line. The HT-29 cell line was established in Dr. Jorgen Fogh's lab (Memorial Sloan Kettering Cancer Center)[116], while the SK-RC-52 cell line was established in Dr. Lloyd Old's lab (Memorial Sloan Kettering Cancer Center)[117]. For the HT-29 model, CA-IX expression is observed near perinecrotic areas because of low vasculature density and diffusion limited hypoxia[118]. In the SK-RC-52 model, a high expression of CA-IX is observed due to impaired functionality of the *VHL* gene leading to constitutive HIF-1α activation[113, 119, 120]. Biallelic mutations, loss of heterozygosity or epigenetic silencing are common causes of *VHL* inactivation in CCRCC[121, 122]. Although CA-IX is considered a good diagnostic/therapeutic target for CCRCC, its expression can be independent of the cellular hypoxia-response.

1.3.6 CA-IX Nuclear Imaging Agents

This section is meant to provide an overview of the different classes of pharmacological agents that have been radiolabeled for PET or SPECT imaging. The development and biological evaluations of CA-IX radiotracers by our group will be discussed in subsequent chapters.

1.3.6.1 Monoclonal Antibodies

Monoclonal antibodies (mAbs) are a highly successful class of antigen recognition molecules for cancer diagnosis and therapy. Given their high specificity to target antigens, mAbs were hailed as "magic bullets" for cancer. Today, many humanized mAbs like trastuzumab, bevacizumab, cetuximab, rituximab, and alemtuzumab are employed as cancer therapeutics[123, 124]. In the case of CA-IX, two mAbs have been at the forefront for clinical use: M75 and cG250. Both mAbs bind to the PG-like domain of CA-IX and have been evaluated as imaging agents. M75 was radiolabeled with ^{125}I for preclinical imaging studies[118, 125], and is now commercially available as part of an ELISA kit from Siemens[126]. On the other hand, cG250 (marketed by WILEX AG as Rencarex®) has been radiolabeled with an assortment of imaging isotopes including ^{124}I, ^{111}In, and ^{89}Zr[127-129]. In a phase III trial (REDUCTANE study), ^{124}I-cG250 had higher average sensitivity and specificity for the diagnosis of CCRCC compared to contrast-enhanced computed tomography alone (86.2% and 85.9% for PET/CT vs. 75.5% and 46.8% for CT)[127]. Despite the success of mAbs, there is significant interest in developing alternative approaches for imaging CA-IX in vivo. The high molecular weight of mAbs, combined with tumour interstitial pressure and aberrant vasculature, could limit tissue penetrance and ability to bind CA-IX in hypoxic niches[130]. Moreover, due to slow pharmacokinetic clearance mAb imaging typically requires a non-ideal delay of 4-7 days post-injection (p.i.) to achieve high contrast images.

1.3.6.2 Small Molecule Inhibitors

Small molecule inhibitors are promising alternatives to mAb-based imaging. Due to their low molecular weights, small molecules generally exhibit higher tumour penetration and faster pharmacokinetics. Furthermore, small molecules are non-immunogenic and easier and less expensive to produce. Sulfonamides and coumarins are two classes of small molecules that are efficacious in inhibiting CA-IX activity, but differ in their mechanism of action. Sulfonamides and isoether derivatives, sulfamates and sulfamides, inhibit CA-IX by forming coordination with Zn^{2+} ion of the catalytic domain and displacing H_2O[131]. In contrast, coumarins are suicide inhibitors that undergo hydrolysis to bind irreversibly at the entrance leading to the catalytic domain. By sterically hindering substrate binding, coumarins inhibit CA-IX activity[132]. However

given the large number of human CA isoenzymes and the homology shared for the catalytic domain, it is very challenging to design potent inhibitors specifically targeting a single isoform[67].

Of the small molecule inhibitors that have been radiolabeled for CA-IX imaging, only a subset of them has been evaluated in vivo (Figure 1.6). Apte *et al.* reported the synthesis of an ^{18}F-labeled sulfonamide derivative (compound A), but no biological data were presented[133]. Lu *et al.* reported the synthesis of a series of ^{99m}Tc/Re-labeled benzenesulfonamide derivatives[134]. Among them, ^{99m}Tc-3d (compound B) exhibited high binding affinity (IC_{50} = 9 nM) to hypoxic CA-IX expressing HeLa cells, but no further evaluation in animal imaging study was presented. Asakawa *et al.* reported ^{11}C-labeling of three potent benzenesulfonamides (compounds C), but no biological evaluation data were presented either. Akurathi *et al.* reported biodistribution data for ^{99m}Tc-labeled sulfonamide derivatives (compounds D-H) in HT-29 tumour xenografts[135, 136]. Tracers showed limited retention in tumours (≤ 0.5 %ID/g at 0.5 - 4 h p.i.) with low contrast (≤ 1.0 tumour-to-blood ratio). ^{18}F-VM4-037 (compound I) is an ethoxzolamide derivative developed by Siemens that completed phase II studies[137]. ^{18}F-VM4-037 showed moderate uptake in primary CCRCC lesions, but lesions were difficult to visualize without an accompanying CT due to high background uptake in normal renal parenchyma. ^{18}F-VM4-037 was able to detect extrarenal lesions for patients that had metastatic disease. Interestingly, Peeters *et al.* published preclinical biodistribution/imaging data for ^{18}F-VM4-037 with the tracer reportedly failing to detect CA-IX expression in either glioma or colorectal cancer xenograft models[138]. Krall *et al.* reported the synthesis and evaluation of a ^{99m}Tc-labeled acetazolamide derivative (compound J) with excellent tumour targeting (22 %ID/g at 3 h p.i.) and image contrast, but results were obtained with the CA-IX overexpressing SK-RC-52 tumour xenograft model[139].

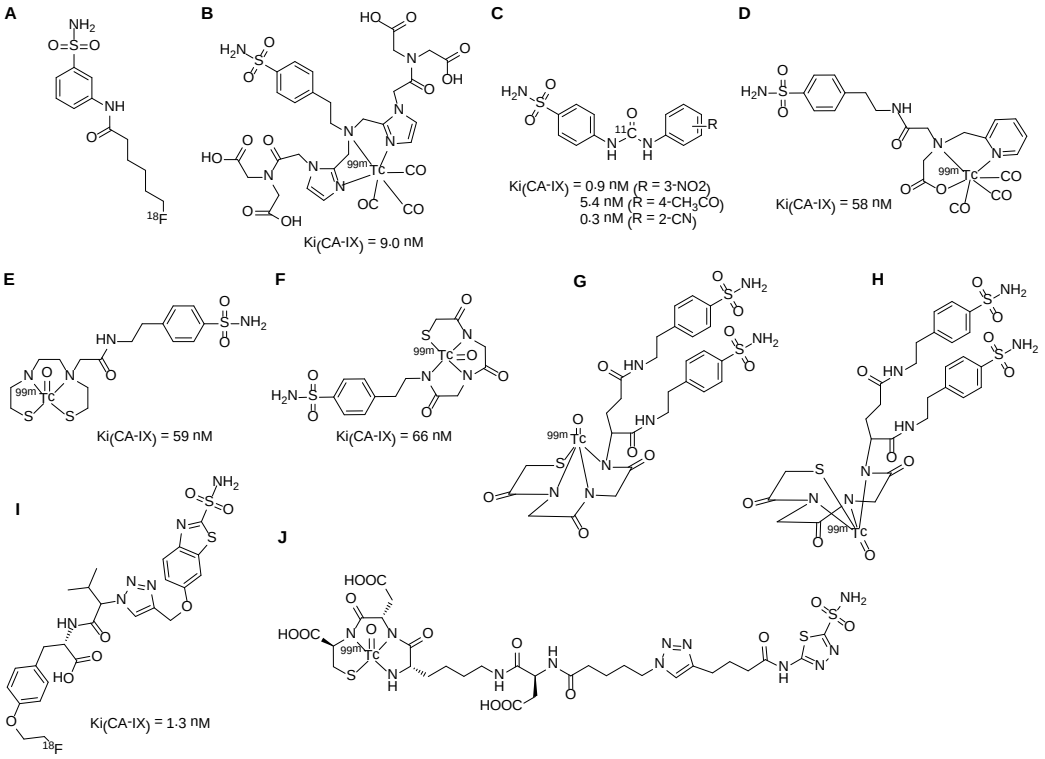

Figure 1.6 Structures of small molecule inhibitors proposed or used for CA-IX imaging. Binding affinities to CA-IX (K_i), where available, were taken from literature.

1.3.6.3 Peptides

Like small molecule inhibitors, peptides offer advantages as imaging vectors in terms of ease of production, lack of immunogenicity, rapid tumour targeting and pharmacokinetic properties[140]. The primary concerns of peptide-based imaging are metabolic lability and potential nephrotoxicity from renal retention[140-142]. As peptides can be subjected to peptidase degradation in vivo, common strategies to improve stability include substituting D-amino acids for L-amino acids, incorporating unnatural amino acids, pseudo-peptide bonds, or intramolecular cyclization[140]. As for nephrotoxicity, administration of positively charged aa like L-arginine and L-lysine, gelofusion or amifostine have been used to reduce renal uptake of peptide tracers[141, 143]. The efficacy of these strategies varies between individual peptide/target systems.

There is no natural peptide ligand for CA-IX; therefore, those that have been explored for molecular imaging have been derived from phage display technology. Askoxylakis *et al.* reported the isolation of CaIX-P1, a dodecapeptide (sequence: YNTNHVPLSPKY) that was raised against the extracellular domain of CA-IX[144]. In biodistribution studies with SK-RC-52

xenograft mice, ^{131}I-CaIX-P1 displayed modest tumour uptake (~2.5 %ID/g) with tumour to muscle ratio of 4.11 ± 2.44 at 1 h p.i. Attempts to optimize CaIX-P1 via alanine scanning and truncations led to the identification of CaIX-P1-4-10 (NHVPLSPy)[145]. Although CaIX-P1-4-10 had approximately 6-fold higher binding ratio than CaIX-P1 in vitro, planar scintigraphy with ^{125}I-CaIX-P1-4-10 was unable to delineate tumour xenografts from background. Due to concerns of isoform selectivity, the Heidelberg group performed a secondary screen against the PG-like domain of CA-IX and isolated the dodapeptide PGLR-P1 (NMPKDVTTRMSS)[146]. However, ^{125}I-PGLR-P1 exhibited micromolar affinity, and uptake value in tumour (0.48 ± 0.20 at 1 h p.i.) was lower than most normal tissues.

1.3.6.4 Affibodies

Affibody molecules are a class of antibody mimetics that were originally derived from the B-domain in the IgG-binding region of staphylococcal protein A[147]. Affibodies are cysteine free proteins of 58 aa residues (6-7 kDa) that fold into three alpha-helix bundle structures[147]. Target specificity is mediated by 13 aa residues[147]. Tolerant to high temperatures, extreme pHs, and structural modifications, these scaffolds typically exhibit nano to picomolar affinities to their targets of interest[147, 148]. Dr. Vladimir Tolmachev's group in Uppsula University, Sweden are experts of this technology, and successfully developed affibodies for imaging HER2, EGFR, IGF-1R, PDGFRβ, HER3, and CA-IX[149-154].

Honarvar *et al.* reported the successful affibody-mediated imaging of CA-IX expression in SK-RC-52 xenograft mice with ^{99m}Tc-HEHEHE-ZCAIX:1[154]. ^{99m}Tc-HEHEHE-ZCAIX:1 exhibited rapid clearance from blood and normal tissues. At 4 h p.i., tumour uptake was 9.7 ± 0.7 %ID/g, which corresponded to tumour-to-muscle and tumour-to-blood ratios of 104 ± 52 and 53 ± 10 respectively. ^{99m}Tc-HEHEHE-ZCAIX:1 generated high contrast SPECT images, despite high retention in kidneys (141 ± 45 %ID/g). The authors concluded that ^{99m}Tc-HEHEHE-ZCAIX:1 may not be suitable for imaging CCRCC; however, it represents a highly promising imaging vector for detecting CA-IX expression for other cancers pending further investigations. The high renal uptake of affibodies can be mitigated by the use of non-residualizing radionuclides or through pre-targeting approaches, with the latter showing great promise with a HER2-specific affibody[155, 156].

1.4 Other Imaging Modalities

1.4.1 Optical Imaging

Similar to SPECT and PET, optical imaging requires the administration of a targeting probe; however, the imaging probe is labeled with a fluorescent molecule in lieu of a radionuclide[157]. Following an uptake period, the target fluorescent molecule is excited by an external laser of appropriate wavelength[157]. This produces an emission of a longer-wavelength light, which is detected for acquisition and image processing[157]. Optical imaging agents are generally limited in terms of tissue penetrance (cm range) due to signal attenuation, but they have an emerging role as a complementary intraoperative imaging modality[158]. Optical agents can be used by surgeons to ensure that clean/negative surgical resection margins are reached[158].

Muselaers *et al.* used cG250 as a pharmacological vector to produce ^{125}I-labeled girentuximab-IRDye800CW, with optical images demonstrating good concordance with SPECT images (31.5 ± 9.6 %ID/g in SK-RC-52 tumours at 72 h p.i.)[159]. Tafreshi *et al.* took a commercially available CA-IX antibody and conjugated it with VivoTag-S 680, termed CA9Ab-680, for imaging breast cancer lymph node metastasis[160]. van Brussel *et al.* used a phage display library to identify a nanobody, single domain antibody, for optical imaging with IRDye800CW[161]. At 2 h p.i., the uptake in CA-IX overexpressing ductal carcinoma in situ mouse cancer model was 14.1 ± 1.1 %ID/g. Groves *et al.* reported a series of sulfonamide derivatives conjugated to near-infrared (NIR) fluorochromes[162]. One acetazolamide derivative in particular, HS680, generated high contrast fluorescence molecular tomography images for tumour-bearing mice (10 %ID in HT-29 tumours at 24 h p.i.) that underwent in vivo hypoxia induction (48 h at 8% O_2 levels)[163]. Wichert and colleagues decribed the use of a dual pharmacophore DNA-encoded chemical library to identify ligand pairs and facilitate affinity maturation for pharmacodelivery applications. They identified a novel CA-IX inhibitor consisting of a 4,4-bis(4-hydroxyphenyl)valeric acid and a succinyl acetazolamide group (A-493/B-202 pair). After conjugating the A-493/B-202 pair to a NIR dye (compound 8c), imaging studies were performed in SK-RC-52 tumour-bearing mice. Compound 8c showed high and sustained tumour uptake (10 ± 2 %ID/g) at 24 h p.i.[164]. More recently, Ly *et al.* reported the synthesis and evaluation of HypoxyFluor, a dimeric sulfonamide inhibitor conjugated to a S0456 NIR dye[165]. Although

biodistribution data was not available, high contrast images were obtained for HT-29 xenograft mice at 4 h p.i.

1.4.2 Magnetic Resonance

Magnetic resonance (MR) imaging is a diagnostic modality that can performed without exposing patients to ionizing radiation[166]. To perform a study, a patient rests in an MR scanner and is subjected to a magnetic field[166]. A radiofrequency pulse is applied to the body, which causes hydrogen atoms to alter their magnetization alignment relative to the magnetic field[166]. The radiofrequency pulse is subsequently switched off to allow the hydrogen atoms to return to their equilibrium or resting states[166]. This process emits radio waves that are detected by receiver coils surrounding the patient. An MR scan is made up of a series of such pulse sequences[166]. The contrast observed between tissues is dependent on the differences in relaxation rates[166]. As hydrogen atoms are found in abundance in fat and water, MR can produce high contrast images of soft tissues[166].

Probes containing exogenous contrast agents (ex. gadolinium or iron oxide) or stable isotopes (ex. ^{13}C or ^{15}N) can be used for molecular targeting with MR[167, 168]. Compared to optical imaging, there has been limited development for CA-IX targeted MR imaging. As CAs are responsible for catalyzing the interconversion of CO_2 and HCO_3^-, Gallagher *et al.* used ^{13}C-labelled HCO_3^- as a probe/substrate to assess the functional activity of CA-IX in colorectal cancer xenograft models[169]. Chen *et al.* conjugated CA-IX targeting sulfonamides onto Fe_3O_4 magnetic nanoparticles for tumour imaging[170]. According to the authors, higher uptake in HT-29 tumour xenograft was observed compared to control nanoparticles (Fe_3O_4 particles alone); however, no quantitative measurements were provided for in vivo studies. Rami *et al.* reported the synthesis of a series of sulfonamides that were conjugated to macrocyclic rings that can bind gadolinium(III), but no imaging experiments were performed[171].

1.5 CA-IX Therapeutics in Clinical Development

As summarized in Table 1.4, different CA-IX therapeutic agents have been investigated in clinical trials. cG250 advanced to a phase III trial (ARISER study), but failed to meet primary endpoint as an adjuvant therapy for CCRCC patients[172]. Meanwhile cG250 radiolabeled with

cytotoxic radionuclide ^{177}Lu recently concluded phase II clinical studies, with disease stabilization observed for 9 of 14 patients that had progressive metastatic CCRCC[173]. However, myelotoxicity prevented some patients from receiving additional treatment courses. BAY-79-4620 is an antibody-drug conjugate (ADC) with monomethyl auristatin E as a neoplastic agent[174]. During the phase I study, several patients experienced severe adverse events including death[175]. This led to the termination of the phase I study, and subsequent discontinuation of clinical development for BAY-79-4620. SLC-0111 is an ureido-sulfonamide inhibitor developed for solid tumours[176]. SLC-0111 is currently in phase I clinical study at three Canadian health institutions including the BC Cancer Agency. Dubois *et al.* developed DH-348, a dual-targeting bioreductive nitroimidazole based sulfonamide that can inhibit CA-IX activity and also act as a radiation sensitizer[177]. With promising preclinical results, phase I study for DH-348 is scheduled to commence in 2016.

Table 1.4 CA-IX therapeutic agents in clinical development.

Compound	Generic name	Category	Indication(s)	Stage[a]
cG250	Girentuximab or Rencarex®	Chimeric antibody	Kidney cancer	Phase III[b]
^{177}Lu-cG250	^{177}Lu-girentuximab	Radiolabeled antibody	Kidney cancer	Phase II
3ee9–MMAE	BAY-79-4620	Antibody–drug conjugate	Solid tumours	Phase I[b]
U-104	SLC-0111	Small molecule inhibitor	Solid tumours	Phase I
DH-348	DTP348	Small molecule inhibitor	Solid tumours, Head and neck neoplasms	-

[a]Highest clinical stage reached to date; [b]No longer in clinical development

1.6 Thesis Theme and Rationale

Pharmacologic inhibition of CA-IX is achievable through mAbs or small molecule inhibitors; however, there remains a need for an effective platform to screen for cancers that will respond to these drugs. Herein, we propose targeting CA-IX and for the diagnosis of aggressive cancers using PET or SPECT imaging. PET and SPECT are non-invasive imaging modalities that use radioisotopes to measure metabolic activities or cancer progression. The detection of

CA-IX in vivo will allow physicians to prescribe personalized therapeutic treatments, to monitor treatment response and in turn improve patient outcomes.

Moreover, considering the role of CA-IX in hypoxia-induced signaling, CA-IX radiotracers have the potential to be surrogate hypoxia imaging agents. The ability to delineate hypoxic volumes can improve radiation planning (ex. intensity modulated radiotherapy or image-guided radiotherapy) or direct hypoxia therapeutics (ex. Tirapazamine).

1.6.1 Objectives and Hypotheses

We studied existing and novel ligands which bind to CA-IX expressing tumours to develop tools to predict and monitor successful response to CA-IX inhibition. Ideal CA-IX radiotracers are ones that can be easily synthesized with high specific activity and radiochemical purity. The radiotracer(s) should be stable in plasma, and stay in circulation long enough to facilitate binding to target tissue. Most significantly, the radiotracer(s) should bind selectively to CA-IX expressing cancers and be rapidly cleared from non-target tissues (to provide good tumour to background signal and to reduce effective dose). Therefore, binding affinity, radiolabeling efficiency, plasma stability, pharmacokinetics, and image quality are criterions that were evaluated for each prospective CA-IX radiotracer.

For this thesis, we proposed the following **hypotheses**:

1) Antigen recognition molecules such as small molecule inhibitors, affibodies, and antibodies can be radiolabelled for in vivo imaging using ^{18}F, ^{68}Ga, ^{111}In, and ^{89}Zr.

2) By matching the appropriate isotope with the biological half-life of the targeting probe, the expression of CA-IX can be measured with high contrast in vivo by PET or SPECT imaging.

3) CA-IX tracers will show improved tumour-to-nontarget ratios and pharmacokinetics over established hypoxia PET tracers.

Chapter 2: ^{18}F-labeled Carbonic Anhydrase IX Inhibitors for Imaging with Positron Emission Tomography

2.1 Introduction

PET imaging can be used to guide the development of novel therapeutics by assessing their distribution and accumulation in tissues of interest, provided that radiolabeled analogues are available. In turn, promising therapeutic agents can serve as lead candidates for the development of novel radiotracers. As discussed, different small molecule inhibitors have been radiolabeled for CA-IX targeted imaging. In Chapter 2, we report the synthesis, ^{18}F labeling, and evaluation of two CA-IX inhibitors, 7-(2-fluoroethoxy)coumarin (FEC) and U-104 (Figure 2.1), as potential tracers for imaging CA-IX expression with PET. Coumarin and sulfonamide derivatives represent the two primary classes of small molecules that have been successful in inhibiting CA-IX activity. U-104, a sulfonamide that demonstrated anti-metastatic potential in preclinical breast cancer models, is currently under evaluation in a multi-center phase I clinical study to determine maximum tolerable dose and pharmacokinetics in cancer patients (ClinicalTrials.gov: Safety study of SLC-0111 in subjects with advanced solid tumours).

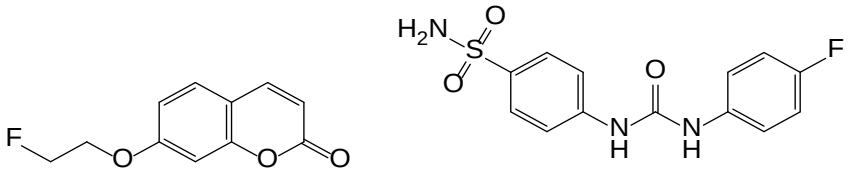

Figure 2.1 Chemical structures of 7-(2-fluoroethoxy)coumarin (Left) and U-104 (Right). Both tracers were radiolabeled with ^{18}F-fluoride for PET imaging.

Adapted from: Synthesis and evaluation of ^{18}F-labeled carbonic anhydrase IX inhibitors for imaging with positron emission tomography. J Enzyme Inhib Med Chem, 2014; 29(2):249-255.

Jinhe Pan[1], **Joseph Lau**[1], Felix Mesak[1], Navjit Hundal[1], Maral Pourghiasian[1], Zhibo Liu[2], Francois Benard[1], Shoukat Dedhar[3], Claudiu T. Supuran[4], Kuo-Shyan Lin[1]

[1] Department of Molecular Oncology, BC Cancer Research Centre, BC Cancer Agency, Vancouver, BC, Canada
[2] Department of Chemistry, University of British Columbia, Vancouver, BC, Canada
[3] Department of Integrative Oncology, BC Cancer Research Centre, BC Cancer Agency, Vancouver, BC, Canada
[4] Dipartimento Neurofarba and Laboratorio di Chimica Bioinorganica, Università degli Studi di Firenze, Florence, Italy

FB and KSL designed the study. JP, JL, FM, NH, MP, and ZL were involved in the experiments. CTS provided the affinity measurements. JP and JL were involved in acquisition of data and interpretation of the analysis. JP and JL wrote the manuscript.

2.2 Materials and Methods

2.2.1 Chemicals and Instrumentation

U-104[178] and its radiolabeling precursor 4-nitrophenyl 4-sulfamoylcarbanilate[179] were prepared according to previously published procedures. All other chemicals and solvents were obtained from commercial sources, and used without further purification. Proton NMR spectra were obtained using a Bruker (Billerica, MA, USA) Avance 400inv Spectrometer, and were reported in parts per million downfield from internal tetramethylsilane. Mass analyses were performed using a Bruker Esquire-LC/MS system with ESI ion source. Purification and quality control of ^{18}F-labeled CA-IX inhibitors were performed on an Agilent (Santa Clara, CA, USA) HPLC System equipped with a model 1200 quaternary pump, a model 1200 UV absorbance detector, and a Bioscan (Washington DC, USA) NaI scintillation detector. The radio-detector was connected to a Bioscan B-FC-1000 Flow-count System, and the output from the Bioscan Flow-count system was fed into an Agilent 35900E Interface which converted the analog signal to digital signal. The operation of the Agilent HPLC system was controlled using the Agilent ChemStation software. The HPLC columns used were a semipreparative column (Phenomenex C18, 5 µ, 250 × 10 mm) and an analytical column (Eclipse XOB-C18, 5 µ, 150 × 4 mm). ^{18}F-Fluoride was produced by the ^{18}O(p, n)^{18}F reaction using an Advanced Cyclotron Systems Inc. (Richmond, BC, Canada) TR19 cyclotron. Radioactivity of ^{18}F-labeled tracers were measured using a Capintec (Ramsey, NJ, USA) CRC®-25R/W dose calibrator, and the radioactivity of mouse tissues collected from biodistribution studies were counted using a Packard Cobra II 5000 Series auto-gamma counter. PET imaging experiments were conducted using a Siemens Inveon microPET/CT scanner.

2.2.2 Synthesis of 7-(2-fluoroethoxy)coumarin (FEC)

A mixture of 7-hydroxycoumarin (0.81 g, 5 mmol), 1-fluoro-2-tosyloxyethane (1.56 g, 7.1 mmol) and K_2CO_3 (3.45 g, 25 mmol) in DMF (15 mL) was heated at 70 °C for 24 h. After cooling to room temperature, CH_2Cl_2 (100 mL) was added to the mixture, and the resulted solution was washed with water (100 mL × 3). The CH_2Cl_2 phase was dried with anhydrous $MgSO_4$, concentrated under reduced pressure, and purified by flash column chromatography on

silica gel using 4:6 EtOAc/hexanes to obtain the desired product FEC as a white solid (0.918 g, 84%).

^{1}H NMR ($CDCl_3$) δ 4.28 (dt, J = 27.6, 4.0 Hz, 2H), 4.80 (dt, J = 47.2, 4.0 Hz, 2H), 6.27 (d, J = 9.2 Hz, 1H), 6.83 (d, J = 2.4 Hz, 1H), 6.89 (dd, J = 8.4, 2.4 Hz, 1H), 7.40 (d, J = 8.4 Hz, 1H), 7.65 (d, J = 9.2 Hz, 1H); MS (ESI) calculated for $C_{11}H_9FO_3$ $(M + H)^+$ 209.1, found 209.0.

2.2.3 Synthesis of 7-(2-tosyloxyethoxy)coumarin

A solution of 7-hydroxycoumarin (0.81 g, 5 mmol), 1,2-bis(tosyloxy)ethane (2.78 g, 7.5 mmol) and K_2CO_3 (3.45 g, 25 mmol) in DMF (15 mL) was heated at 70 °C for 18 h. After cooling to room temperature, CH_2Cl_2 (100 mL) was added and the solution was washed with water (100 mL × 3). The CH_2Cl_2 layer was dried with anhydrous $MgSO_4$, concentrated under reduced pressure, and chromatographed on silica gel using 1:99 CH_3CN/CH_2Cl_2 to obtain the desired product as a white solid (0.282 g, 16%). ^{1}H NMR ($CDCl_3$) δ 2.47 (s, 3H), 4.19-4.25 (m, 2H), 4.39-4.45 (m, 2H), 6.28 (d, J = 9.2 Hz, 1H), 6.68 (d, J = 2.4 Hz, 1H), 6.76 (dd, J = 8.4, 2.4 Hz, 1H), 7.34-7.39 (m, 3H), 7.64 (d, J = 9.2 Hz, 1H), 7.83 (d, J = 8.4 Hz, 1H); MS (ESI) calculated for $C_{18}H_{16}O_6S$ $(M + H)^+$ 361.1, found 361.1.

2.2.4 Binding Affinity Measurement

Inhibition constants (K_i) for CA-I, CA-II, CA-IX and CA-XII were determined following published procedures[178]. An Applied Photophysics stopped-flow instrument was used for assaying the CA catalyzed CO_2 hydration activity. Phenol red (at 0.2 mM) was used as indicator, working at the absorbance maximum of 557 nm, with 20 mM HEPES (pH 7.4) and 20 mM $NaBF_4$ (for maintaining constant the ionic strength), following the initial rates of the CA-catalyzed CO_2 hydration reaction for 10-100 s. The CO_2 concentrations ranged from 1.7 to 17 mM for the determination of the kinetic parameters and inhibition constants. For each inhibitor, at least six traces of the initial 5-10% of the reaction were used for determining the initial velocity. The uncatalyzed rates were determined in the same manner and subtracted from the total observed rates. Stock solutions of inhibitor (10 mM) were prepared in distilled-deionized water, and dilutions up to 0.01 nM were done thereafter with distilled-deionized water. Inhibitor and enzyme solutions were preincubated together for 15 min at room temperature prior to assay

in order to allow for the formation of the E-I complex. The inhibition constants were obtained by nonlinear least-squares methods using PRISM 3, whereas the kinetic parameters for the uninhibited enzymes were from Lineweaver-Burk plots, and represent the mean from at least three different determinations

2.2.5 Radiosynthesis of ^{18}F-FEC

The proton-bombarded $H_2[^{18}O]O$ was transferred via He gas push from the cyclotron target station to a Waters QMA light Sep-Pak cartridge set up in the hot cell. The ^{18}F-fluoride was trapped in the QMA cartridge, and eluted out into a 4-mL V-shaped reaction vial with a mixture of water (0.3 mL) and CH_3CN (0.3 mL) containing K_2CO_3 (7 mg) and kryptofix 222 (K_{222}). The uncapped reaction vial was placed in a heating block, and the solution was heated at 120 °C. After most of the solvents evaporated, CH_3CN (1mL × 2) was added to the reaction vial to facilitate complete removal of water. A solution of 7-(2-tosyloxyethoxy)coumarin (3 mg) in DMF (0.5 mL) was added to the reaction vial containing dry $K[^{18}F]F/K_{222}$. The vial was capped, and the mixture was heated at 70 °C for 30 min. At the end of heating, the mixture was diluted with water (1 mL) and purified by HPLC using the semipreparative column eluted with 35% CH_3CN/65% H_2O at a flow rate of 4.5 mL/min. The retention time of ^{18}F-FEC was 17.4 min. The eluting fraction containing ^{18}F-FEC was collected, diluted with water (50 mL), and trapped on a Waters tC18 light Sep-Pak cartridge. After washing the tC18 light Sep-Pak cartridge with water (10 mL), ^{18}F-FEC was eluted out with ethanol (0.4 mL), and formulated with saline (4 mL) for plasma stability study and μPET/CT imaging study. The quality control was performed by HPLC on the analytical column eluted with 25% CH_3CN/75% H_2O at a flow rate of 2 mL/min. The retention time of ^{18}F-FEC was 8.5 min. The specific activity of ^{18}F-FEC was measured using the analytical HPLC system. It was calculated by dividing the injected radioactivity in 0.2 mL of final ^{18}F-FEC solution by the mass of FEC in the injected solution. The mass of FEC was estimated by comparing the UV absorbance obtained from the injection with a previously prepared standard curve.

2.2.6 Radiosynthesis of ^{18}F-U-104

(1) Radiosynthesis of 1-[^{18}F]fluoro-4-nitrobenzene: A solution of 1,4-dinitrobenzene (4 mg) in DMSO (0.5 mL) was added to a 4-mL reaction vial containing dry K[^{18}F]F/K_{222}. The vial was capped, and the mixture was heated at 125 °C for 10 min. At the end of the heating, the mixture was diluted with water (10 mL). The resulted solution was passed through a Waters tC18 plus Sep-Pak cartridge, and the cartridge was washed with water (10 mL). The trapped 1-[^{18}F]fluoro-4-nitrobenzene was eluted out of Sep-Pak cartridge with methanol (1.5 mL).

(2) Radiosynthesis of 4-[^{18}F]fluoroaniline: The above solution of 1-[^{18}F]fluoro-4-nitrobenzene in methanol was added to a vial containing 10% palladium on carbon (4 mg) and sodium borohydride (10 mg). The resulted mixture was incubated at room temperature for 5 min. The reaction was quenched by adding 0.1 mL of concentrated HCl and diluted with 1 M NaOH (20 mL). The resulted solution was passed through a Lichrolut EN column (500 mg). The trapped 4-[^{18}F]fluoroaniline in the Lichrolut EN column was eluted out with THF (2 mL) and dried by passing the THF solution through a pre-packed column containing celite (125 mg) and anhydrous $MgSO_4$ (125 mg).

(3) Radiosynthesis of ^{18}F-U-104: The above solution of 4-[^{18}F]fluoroaniline in THF was added to a 4-mL reaction vial containing 4-nitrophenyl 4-sulfamoylcarbanilate (8 mg) and DIEA (10 μL) in DMF (0.5 mL). The resulted mixture was heated at 125 °C for 15 min, diluted with water (1 mL), and purified by HPLC using the semipreparative column eluted with 40% MeOH/60% H_2O at a flow rate of 4.5 mL/min. The retention time of ^{18}F-U-104 was 27.4 min. The eluting fraction containing ^{18}F-U-104 was collected, diluted with water (50 mL), and passed through a Waters tC18 light Sep-Pak cartridge. The trapped ^{18}F-U-104 on the Sep-Pak cartridge was eluted out with ethanol (0.4 mL), and formulated with saline (4 mL) for plasma stability and biodistribution studies. The quality control of ^{18}F-U-104 was performed on HPLC using the analytical column eluted with 25% CH_3CN/75% H_2O at a flow rate of 2 mL/min. The retention time of ^{18}F-U-104 was 7.7 min. The specific activity of ^{18}F-U-104 was measured following same procedures as described for the calculation of specific activity of ^{18}F-FEC.

2.2.7 Stability in Mouse Plasma

Aliquots (100 µL) of the ^{18}F-labeled tracer (^{18}F-FEC or ^{18}F-U-104) were incubated with 400 µL of BALB/c mouse plasma (Innovative Research) for 5, 15, 30, 60, and 120 minutes at 37°C. At the end of each incubation period, samples were passed through a 0.45 micron filter. The filtered sample was loaded onto the analytical HPLC to check for metabolite(s) formation, and analysis was conducted with Agilent ChemStation software.

2.2.8 In Vivo Experiments

HT-29 human colorectal cancer cells were obtained as a gift from Dr. Donald Yapp (BC Cancer Research Centre, Vancouver, Canada). Cells were cultured in Dulbecco's Modified Eagle's Medium supplemented with 10% fetal bovine serum, 100 U/mL penicillin-streptomycin, and non-essential amino acids. Mice were maintained and the experiments were conducted in accordance with the guidelines established by the Canadian Council on Animal Care and approved by the Animal Ethics Committee of the University of British Columbia.

2.2.8.1 Tumour Implantation

All experiments were performed using NOD.Cg-*Prkdc*^{scid}*Il2rg*^{tm1Wjl}/SzJ (NSG) mice bred in-house at the Animal Research Centre, British Columbia Cancer Research Centre, Vancouver, Canada. Mice were anesthetized briefly with 2.5% isoflurane in 2.0 L/min of oxygen during cell implantation. After wiping skin surrounding the injection site with an alcohol prep pad, a 28.5-Gauge needle was used to subcutaneously implant 5 x 10^6 HT-29 cells (in 100 µL of 1xPBS and BD Matrigel Matrix at 1:1 ratio) under the right shoulder. Biodistribution studies and PET/CT imaging were performed when tumours reached 5-7 mm in diameter.

2.2.8.2 Biodistribution Studies

Tumour bearing mice were injected with ~ 3.7 MBq of ^{18}F-U-104 (100 – 200 µL in saline, i.v.). After an uptake period of 1 h, mice were euthanized by CO_2 asphyxiation. Blood was promptly withdrawn, and organs/tissues of interest were harvested, rinsed with saline, blotted dry and

weighed. Radioactivity in collected tissues was counted, normalized to the injected dose and expressed as the percentage of the injected dose per gram of tissue (%ID/g).

2.2.8.3 PET Imaging and Data Analysis:

Under anesthesia, 3.7-7.4 MBq of ^{18}F-FEC was administered intravenously through the caudal vein into HT-29 tumour bearing mice (n = 4). CT scan was performed before a PET dynamic image sequence of 10 or 55 minutes. PET data were acquired in list mode acquisition. At 1 h p.i., mice were euthanized by CO_2 asphyxiation followed by cervical dislocation. The tissues of interest were harvested, weighed, and counted as described in the above Biodistribution Studies section. The PET data were reconstructed using the 3d-OSEM-MAP algorithm with CT-based attenuation correction. 3D regions of interest (ROI) were placed on the reconstructed images to determine the %ID/g of tissue using the Inveon Research Workplace software (IRW).

2.2.9 Immunohistochemistry

For validation of CA-IX expression in HT-29 tumours, histologic tissue analysis was performed. Tumours were harvested and fixed in 4% paraformaldehyde in PBS for 48 h at room temperature. After dehydration, tissues were embedded in paraffin and 4 µm sections were mounted onto poly-L-lysine slides. Immunostaining was performed by the Centre of Translational Applied Genomics at the BC Cancer Agency using the Ventana Discovery XT instrument. Slides were incubated with a goat anti-human CA-IX antibody (R&D AF2188) for 1 h without heat at a 1:200 dilution in CC1 antigen retrieval buffer. A rabbit anti-goat linker (1:500) was applied for 32 min followed by a 16-min incubation with Ultramap anti-rabbit HRP detection kit. The stained sections were examined and photographed with a Leica EC3 microscope.

2.3 Results and Discussion

FEC is a coumarin derivative, whereas U-104 is an ureido-substituted benzenesulfonamide. Both coumarins and benzenesulfonamides have been shown to be potent inhibitors of CA-IX[131, 132]. In addition, U-104 has been previously reported to inhibit tumour

growth and metastasis in spontaneous and experimental models of metastasis, without inhibitory effects on CA-IX-negative tumours[67]. As shown in Figure 2.2, the FEC standard was synthesized in 84% yield by coupling 7-hydroxycoumarin with 1-fluoro-2-tosyloxyethane[180].

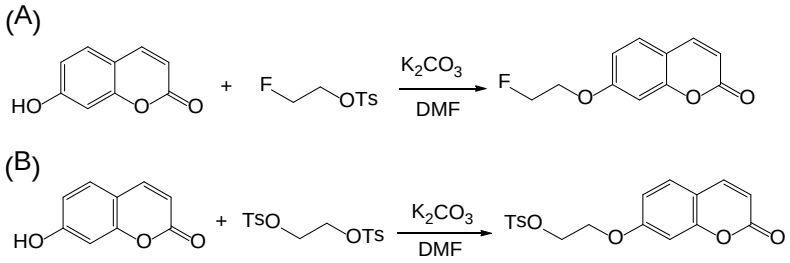

Figure 2.2 Synthetic scheme for the preparation of FEC and its radiolabeling precursor. (A) Cold standard. (B) Labeling precursor.

For the development of CA-IX targeted tracers, one concern is the binding to other major CA isoforms including I, II and XII. Cytosolic CA-I and CA-II are expressed in red blood cells[181, 182] and the binding of CA-IX targeted radiotracers to either isoform would increase background signal and reduce image contrast. On the contrary, binding of these CA-IX targeted radiotracers to CA-XII could be beneficial as CA-XII is expressed on membranes and is also up-regulated in hypoxic tumours[183]. The inhibition constants (K_i) for human CA isoenzymes I, II, IX, and XII were 4622, > 100000, 70, and 88 nM for FEC, respectively. The K_i values for U-104 have been previously reported to be 5080, 96, 45, and 4.5 nM for CA isoenzymes I, II, IX, and XII, respectively[85, 178].

The radiolabeling precursor, 7-(2-tosyloxyethoxy)coumarin, was prepared by coupling 7-hydroxycoumarin with 1,2-bis(tosyloxy)ethane in 16% yield (Figure 2.2B), while radiosynthesis of ^{18}F-FEC was prepared via the ^{18}F aliphatic nucleophilic substitution (Figure 2.3A). After HPLC purification, ^{18}F-FEC was obtained in 11-24% decay-corrected yield in 1.6 h synthesis time with 62.9 – 210.9 GBq/μmol specific activity at the end of synthesis (EOS), and > 99% radiochemistry purity. The preparation of ^{18}F-U-104 was depicted in Figure 2.3B. The radiosynthesis involved three reactions. First, 1-[^{18}F]fluoro-4-nitrobenzene was prepared in 40-60% radiochemical yield by direct aromatic nucleophilic substitution reaction using ^{18}F-fluoride and dinitrobenzene. The isolated 1-[^{18}F]fluoro-4-nitrobenzene was reduced to 4-

[^{18}F]fluoroaniline in > 90% yield following previously published procedure[184] using $NaBH_4$ and 10% Pd/C. At the final step, ^{18}F-U-104 was obtained in > 50% radiochemical yield by reacting 4-[^{18}F]fluoroaniline with 4-nitrophenyl 4-sulfamoylcarbanilate in DMF. However, due to multiple purification steps, ^{18}F-U-104 was isolated in only 3-9% overall decay-corrected yield in 2.5 h synthesis time with > 98% radiochemical purity, and 558.7-732.6 GBq/μmol specific activity at EOS. The reason that ^{18}F-U-104 had much higher specific activity than ^{18}F-FEC was because we used Teflon tubing as the H[^{18}F]F/H_2[^{18}O]O transfer line while preparing ^{18}F-FEC. Before working on ^{18}F-U-104, we replaced the Teflon transfer line with peek tubing. This change reduced the amount of fluoride leaching out from the transfer line, and significantly increased the specific activities of ^{18}F-labeled tracers including ^{18}F-U-104 prepared thereafter.

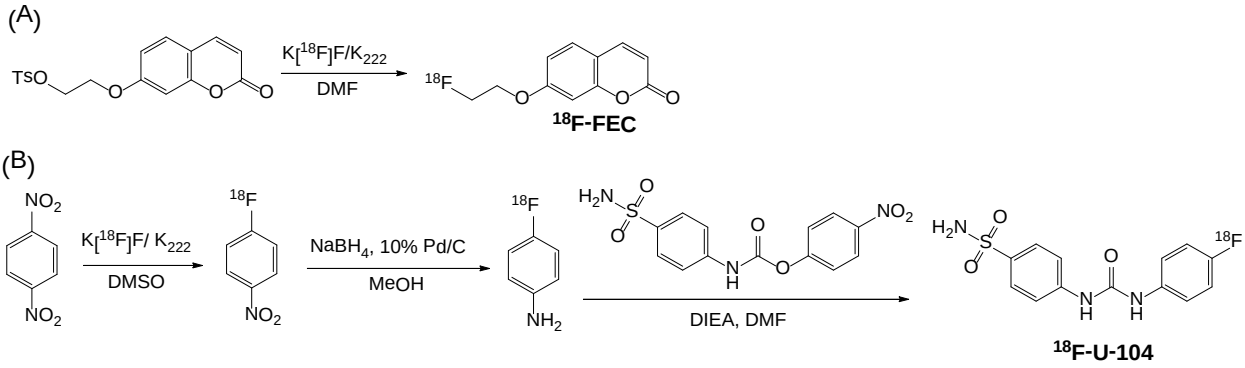

Figure 2.3 Radiosynthesis of (A) ^{18}F-FEC and (B) ^{18}F-U-104. ^{18}F-FEC required one-step fluorination, while the preparation of ^{18}F-U-104 was conducted in three-steps.

Both ^{18}F-U-104 and ^{18}F-FEC were stable in mouse plasma with > 99% of the tracers remaining intact after 2 h incubation at 37 °C. For the imaging/biodistribution studies, we used HT-29 colorectal tumour xenografts as our CA-IX-expressing tumour model, and the expression of CA-IX in the tumours was confirmed by immunohistochemistry (Figure 2.4). Due to its high expression of CA-IX, HT-29 cells have also been used by other investigators as a model for the development of CA-IX targeted tracers.

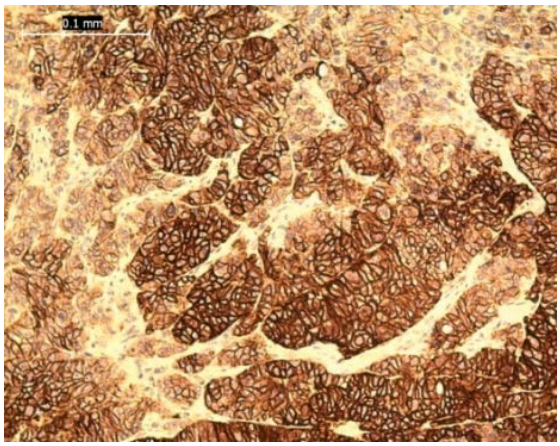

Figure 2.4 CA-IX expression in HT-29 colorectal cancer model. CA-IX expression in cell model was confirmed ex vivo with immunohistochemistry. Scale bar 0.1 mm.

The biodistribution data of ^{18}F-U-104 (Table 2.1) indicated that the radioactivity was excreted via both renal and hepatobiliary pathways. The uptake in intestines and kidneys at 1 h p.i. were 13.66 ± 1.23 and 9.71 ± 1.68 %ID/g, respectively. Tumour uptake (%ID/g) of ^{18}F-U-104 at 1 h p.i. was 0.83 ± 0.06 which was lower than blood (13.92 ± 3.07), muscle (1.19 ± 0.20), and major organs except brain (0.16 ± 0.01). High blood uptake of ^{18}F-U-104 is likely due to the binding to CA-II in erythrocytes. U-104 has good affinity (96 nM) for CA-II and it has been shown that erythrocytes express high level of CA-II[181, 182]. Due to minimal uptake of ^{18}F-U-104 in HT-29 tumours compared to normal tissues/organs, ^{18}F-U-104 is not suitable for use for CA-IX targeted imaging.

Biodistribution and PET imaging studies of ^{18}F-FEC showed that the radioactivity was excreted via both renal and hepatobiliary pathways (Table 2.1, Figure 2.5). In vivo defluorination of ^{18}F-FEC was likely as uptake in bone (2.09 ± 0.50 %ID/g) was higher than the uptake in both blood (1.54 ± 0.44 %ID/g) and muscle (0.73 ± 0.13 %ID/g) at 1 h p.i. Tumour uptake of ^{18}F-FEC was 1.16 ± 0.19 %ID/g at 1 h p.i. The tumours were not visualized from PET image (Figure 2.5) due to low tumour uptake and very high liver uptake (33.76 ± 8.31 %ID/g at 1 h p.i.). The high uptake in the liver was not simply due to the hepatobiliary excretion of ^{18}F-FEC as the uptake in intestines was low (3.14 ± 1.24 %ID/g) and the uptake in the liver did not decrease over time (Figure 2.6).

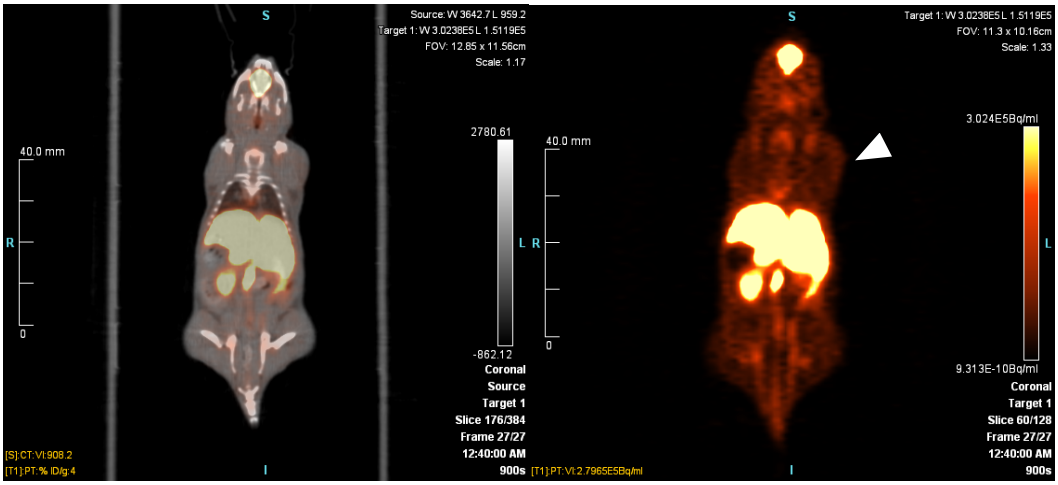

Figure 2.5 Representative PET image of ^{18}F-FEC in HT-29 xenograft mice at 55 min p.i. (Left) PET/CT overlaid image (Right) PET alone. Arrow indicates tumour.

Table 2.1 Biodistribution data (1 h p.i.; n = 4) of ^{18}F-FEC and ^{18}F-U-104 in NSG mice bearing HT-29 human colorectal tumour xenografts.

Tissues/Organs	**Radiotracers**	
	^{18}F-FEC	^{18}F-U-104
Blood	1.54 ± 0.44	13.92 ± 3.07
Intestine	3.14 ± 1.24	13.66 ± 1.23
Stomach	0.89 ± 0.46	2.94 ± 2.28
Spleen	1.89 ± 0.88	6.48 ± 0.74
Liver	33.76 ± 8.31	6.76 ± 0.22
Pancreas	0.77 ± 0.10	3.33 ± 0.11
Kidney	6.97 ± 3.34	9.71 ± 1.68
Lungs	1.18 ± 0.24	5.71 ± 0.42
Heart	1.16 ± 0.27	3.46 ± 0.57
Muscle	0.73 ± 0.13	1.19 ± 0.20
Bone	2.09 ± 0.50	2.52 ± 0.81
Brain	0.88 ± 0.16	0.16 ± 0.01
Tumour	1.16 ± 0.19	0.83 ± 0.06

Values (%ID/g) are presented as mean ± SD

A possible explanation for the high uptake of ^{18}F-FEC in the liver is the metabolic action of 7-ethoxycoumarin O-deethylase (ECOD). ECOD is a family of cytochrome P450 enzymes that metabolize 7-ethoxycoumarin into 7-hydroxycoumarin and acetaldehyde[185] as depicted in Figure 2.7. ECOD is highly expressed in the liver, and one of the major ECOD is CYP1A2[185, 186]. Due to the similarity of 7-ethoxycoumarin and FEC in their structures, it is likely that ECOD

also metabolizes ^{18}F-FEC into 7-hydroxycoumarin and 2-[^{18}F]fluoroacetaldehyde (Figure 2.7). The radioactive metabolite 2-[^{18}F]fluoroacetaldehyde can be further metabolized into 2-[^{18}F]fluoroacetate which in turn forms 2-[^{18}]fluoroacetyl CoA and becomes trapped within the cell[187]. This hypothesis was supported by the high uptake of ^{18}F-FEC observed in the nasal cavity (Figure 2.5) as olfactory mucosa is the only extrahepatic tissue expressing high level of CYP1A2[188]. However, more studies are needed to confirm the trapping mechanism of ^{18}F-FEC in the liver and nasal cavity.

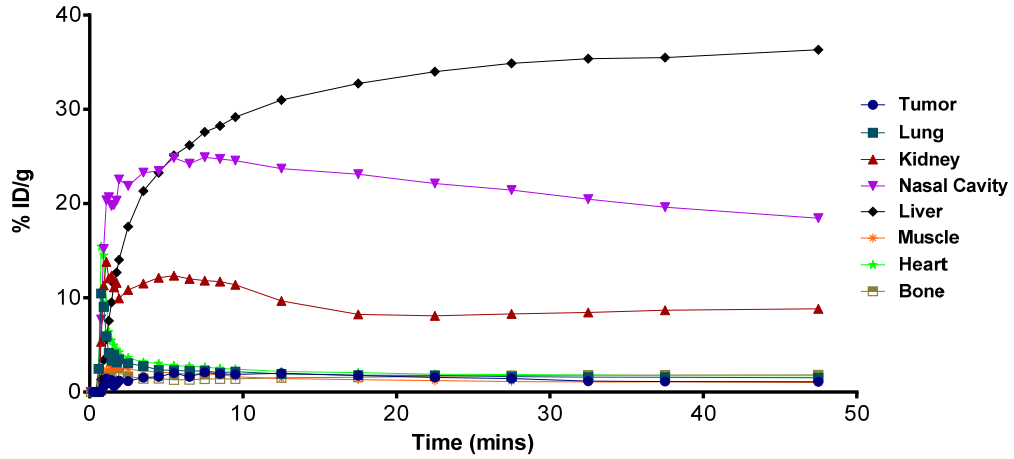

Figure 2.6 Time-activity curve of ^{18}F-FEC in tumour and selected organs/tissues. The Y-axis indicates uptake in %ID/g while the X-axis represents time in minutes.

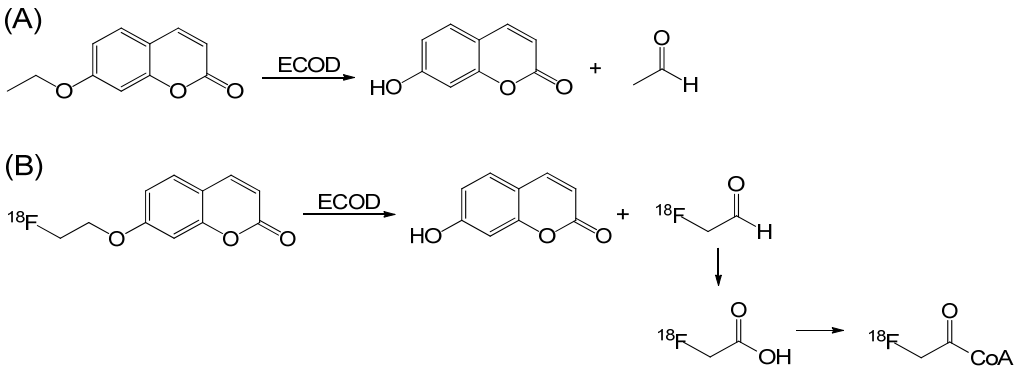

Figure 2.7 (A) Metabolism of 7-ethoxycoumarin and (B) proposed metabolism of ^{18}F-FEC by ECOD

2.4 Conclusion

We have synthesized two ^{18}F-labeled CA-IX inhibitors, ^{18}F-FEC and ^{18}F-U-104, and evaluated their potential as CA-IX targeted PET tracers. Both compounds showed good affinity for CA-IX and excellent stability in mouse plasma. However, their uptake in CA-IX-expressing HT-29 tumours was minimal which precludes their application as CA-IX imaging agents. The unexpected trapping of ^{18}F-FEC in the liver and nasal cavity could be due to the metabolism of ^{18}F-FEC by ECOD. Once this is confirmed, ^{18}F-FEC may be potentially used for imaging the expression/activity of ECOD with PET.

Chapter 3: ^{18}F-labeled Tertiary Substituted Sulfonamides for PET CA-IX Imaging

3.1 Introduction

As exemplified in Chapter 2, the structural and aa conservation shared by CA isoforms is a challenge for the design of CA-IX imaging agents[189]. Structural analyses identified subtle differences in aa composition within the hydrophilic and hydrophobic pockets of the active site which may be exploited to create "CA selective" agents[189, 190]. Towards this end, our collaborator Dr. Claudiu Supuran (Italy) reported a class of fluorinated tertiary substituted sulfonamides that showed strong selectivity for CA-IX without inhibiting the ubiquitously expressed CA-II isoform[191]. In their deprotonated form, sulfonamides bind to the Zn^{2+} ion to displace catalytic H_2O while forming a tetrahedral coordination with aa residues around the active site[131]. However, the unique selectivity of these tertiary substituted sulfonamides is attributed to a new but unresolved mode of binding, as these inhibitors do not undergo deprotonation and thus do not bind to the Zn^{2+} ion[192]. We selected three derivatives within this series that were amendable to [^{18}F]fluorination for small animal PET imaging studies (Figure 3.1).

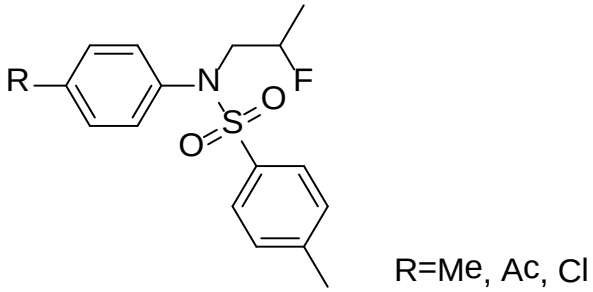

Figure 3.1 Chemical structures of fluorinated tertiary substituted sulfonamides. Three inhibitors were identified by Métayer *et al.* as potent and specific CA-IX inhibitors[191].

Adapted from: Synthesis and Evaluation of ^{18}F-Labeled Tertiary Sulfonamides for Imaging Carbonic Anhydrase IX expression in Tumours with Positron Emission Tomography. Bioorg Med Chem Lett, 2014; 24(14):3064-3068.

Joseph Lau[1], Jinhe Pan[1], Zhengxing Zhang[1], Navjit Hundal[1], Zhibo Liu[2], Francois Benard[1], Kuo-Shyan Lin[1]

[1] Department of Molecular Oncology, BC Cancer Research Centre, BC Cancer Agency, Vancouver, BC, Canada
[2] Department of Chemistry, University of British Columbia, Vancouver, BC, Canada

JL, FB and KSL designed the study. JL, JP, NH, and ZL were involved in the experiments. JL and JP were involved in acquisition of data and interpretation of the analysis. JL wrote the manuscript.

3.2 Materials and Methods

3.2.1 Chemicals and Instrumentation

Compounds **1a-c** were prepared according to previously published procedures[191]. All other chemicals and solvents were obtained from commercial sources, and used without further purification. Proton NMR spectra were obtained using a Bruker (Billerica, MA, USA) Avance 400inv Spectrometer, and were reported in parts per million downfield from internal tetramethylsilane. Mass analyses were performed using a Bruker Esquire-LC/MS system with ESI ion source. Melting points were taken on a Fisher-Johns melting point apparatus (Fisher Scientific, Pittsburgh, PA) and were uncorrected. Purification and quality control of ^{18}F-labeled **4a-c** were performed on an Agilent (Santa Clara, CA, USA) HPLC System equipped with a model 1200 quaternary pump, a model 1200 UV absorbance detector, and a Bioscan (Washington DC, USA) NaI scintillation detector. The radio-detector was connected to a Bioscan B-FC-1000 Flow-count system, and the output from the Bioscan Flow-count system was fed into an Agilent 35900E Interface which converted the analog signal to digital signal. The operation of the Agilent HPLC system was controlled using the Agilent ChemStation software. The HPLC columns used were a semi-preparative column (Phenomenex C18, 5 μ, 250 × 10 mm) and an analytical column (Eclipse XOB-C18, 5 μ, 150 × 4 mm). ^{18}F-Fluoride was produced by the ^{18}O(p, n)^{18}F reaction using an Advanced Cyclotron Systems Inc. (Richmond, BC, Canada) TR19 cyclotron. Radioactivity of ^{18}F-labeled **4a-c** were measured using a Capintec (Ramsey, NJ, USA) CRC®-25R/W dose calibrator, and the radioactivity of mouse tissues collected from biodistribution studies were counted using a Packard Cobra II 5000 Series auto-gamma counter. PET imaging experiments were conducted using a Siemens (Malvern, PA, USA) Inveon microPET/CT scanner.

3.2.2 Syntheses of Precursors and Standards

3.2.2.1 *N*-(2-hydroxypropyl)-4-methyl-*N*-(4-methylphenyl)benzenesulfonamide (2a)

A solution of **1a** (1.22 g, 4.67 mmol), K_2CO_3 (1.29 g, 9.35 mmol), and propylene oxide (1.4 mL, 20 mmol) in DMF (6 mL) was heated at 80 °C overnight. After cooling to room temperature, the reaction mixture was diluted with water (100 mL), and extracted with ethyl acetate (100 mL).

The ethyl acetate layer was dried with anhydrous $MgSO_4$, concentrated under reduced pressure, and chromatographed on silica gel using 35:65 ethyl acetate/hexane to obtain the desired product **2a** as a light brown oil (1.38 g, 92%). ^{1}H NMR ($CDCl_3$) δ 7.50 (d, J = 8.2 Hz, 2H, Ar–H), 7.27 (d, J = 8.2 Hz, 2H, Ar–H), 7.12 (d, J = 8.2 Hz, 2H, Ar–H), 6.95 (d, J = 8.2 Hz, 2H, Ar–H), 3.91 – 3.69 (m, 1H, C*H*), 3.59 (dd, J = 13.7, 8.3 Hz, 1H, CH_2), 3.36 (dd, J = 13.7, 3.5 Hz, 1H, CH_2), 2.44 (s, 3H, CH_3), 2.35 (s, 3H, CH_3), 1.15 (d, J = 6.3 Hz, 3H, CH_3). MS (ESI) calculated for $C_{17}H_{21}NO_3S$ 319.1, found $(M + H)^+$ 320.3.

3.2.2.2 *N*-(4-Acetylphenyl)-*N*-(2-hydroxypropyl)-4-methylbenzenesulfonamide (2b)

Following similar procedures as described for the preparation of **2a** by starting with **1b** (1.07 g, 3.69 mmol), K_2CO_3 (1.02 g, 7.38 mmol), and propylene oxide (1.4 mL, 20 mmol) in DMF (6 mL), 1.25 g (98%) of **2b** was obtained as a colourless oil after chromatography on silica gel using 35:65 ethyl acetate/hexane. ^{1}H NMR ($CDCl_3$) δ 7.50 (d, J = 8.2 Hz, 2H, Ar–H), 7.27 (d, J = 8.2 Hz, 2H, Ar–H), 7.12 (d, J = 8.2 Hz, 2H, Ar–H), 6.95 (d, J = 8.2 Hz, 2H, Ar–H), 3.91 – 3.69 (m, 1H, CH), 3.59 (dd, J = 13.7, 8.3 Hz, 1H, CH_2), 3.36 (dd, J = 13.7, 3.5 Hz, 1H, CH_2), 2.44 (s, 3H, CH_3), 2.35 (s, 3H, CH_3), 1.15 (d, J = 6.3 Hz, 3H, CH_3). MS (ESI) calculated for $C_{18}H_{21}NO_4S$ 347.1, found $(M + Na)^+$ 370.1.

3.2.2.3 *N*-(4-Chlorophenyl)-*N*-(2-hydroxypropyl)-4-methylbenzenesulfonamide (2c)

Following similar procedures as described for the preparation of **2a** by starting with **1c** (1.41 g, 4.14 mmol), K_2CO_3 (1.14 g, 8.29 mmol), and propylene oxide (1.4 mL, 20 mmol) in DMF (6 mL), 1.40 g (99%) of **2c** was obtained as a colourless oil after chromatography on silica gel using 20:80 ethyl acetate/hexane. ^{1}H NMR ($CDCl_3$) δ 7.48 (d, J = 8.3 Hz, 2H, Ar–H), 7.38 – 7.20 (m, 4H, Ar–H), 7.12 – 6.94 (m, 2H, Ar–H), 3.90 – 3.71 (m, 1H, CH), 3.58 (dd, J = 13.8, 8.1 Hz, 1H, CH_2), 3.38 (dd, J = 13.8, 3.8 Hz, 1H, CH_2), 2.44 (s, 3H, CH_3), 1.17 (d, J = 6.3 Hz, 3H, CH_3). MS (ESI) calculated for $C_{16}H_{18}ClNO_3S$ 339.1, found $(M + H)^+$ 340.2.

3.2.2.4 4-Methyl-*N*-(4-methylphenyl)-*N*-(2-tosyloxypropyl)benzenesulfonamide (3a)

A solution of **2a** (1.37 g, 4.29 mmol) in CH_2Cl_2 (20 mL) was added sequentially to *p*-toluenesulfonyl chloride (1.13 g, 5.95 mmol), trimethylamine hydrochloride (410 mg, 4.29 mmol), and diisopropylethylamine (1.42 mL, 8.58 mmol). After stirring at room temperature overnight, the solution was diluted with CH_2Cl_2 (80 mL), washed with 1N HCl (100 mL), and saturated $NaHCO_3$ aqueous solution (100 mL). The CH_2Cl_2 layer was dried with anhydrous $MgSO_4$, concentrated under reduced pressure, and chromatographed on silica gel using 25:75 ethyl acetate/hexane to obtain the desired product **3a** as a white solid (1.76 mg, 86%), mp: 123-125°C. ^{1}H NMR ($CDCl_3$) δ 7.69 (d, J = 8.2 Hz, 2H, Ar–H), 7.39 (d, J = 8.2 Hz, 2H, Ar–H), 7.34 – 7.19 (m, 4H, Ar–H), 7.06 (d, J = 8.2 Hz, 2H, Ar–*H*), 6.77 (d, J = 8.2 Hz, 2H, Ar–H), 4.76 – 4.53 (m, 1H, CH), 3.67 (dd, J = 13.8, 5.5 Hz, 1H, CH_2), 3.56 (dd, J = 13.8, 7.1 Hz, 1H, CH_2), 2.46 (s, 3H, CH_3), 2.43 (s, 3H, CH_3), 2.34 (s, 3H, CH_3), 1.33 (d, J = 6.3 Hz, 3H, CH_3). MS (ESI) calculated for $C_{24}H_{27}NO_5S_2$ 473.1, found $(M + H)^+$ 474.2.

3.2.2.5 *N*-(4-Acetylphenyl)-4-methyl-*N*-(2-tosyloxypropyl)benzenesulfonamide (3b)

Following similar procedures as described for the preparation of **3a** by starting with **2b** (380 mg, 1.09 mmol), *p*-toluenesulfonyl chloride (313 mg, 1.64 mmol), trimethylamine hydrochloride (105 mg, 1.09 mmol), and diisopropylethylamine (0.38 mL, 2.19 mmol), 424 mg (77%) of **3b** was obtained as a white solid after chromatographed on silica gel using 30:70 ethyl acetate/hexane. mp: 112-114 °C ^{1}H NMR ($CDCl_3$) δ 7.85 (d, J = 8.5 Hz, 2H, Ar–H), 7.67 (d, J = 8.2 Hz, 2H, Ar–H), 7.37 (d, J = 8.2 Hz, 2H, Ar–H), 7.31 (d, J = 8.1 Hz, 2H, Ar–H), 7.24 (d, J = 8.1 Hz, 2H, Ar–H), 7.05 (d, J = 8.5 Hz, 2H, Ar–H), 4.78 – 4.51 (m, 1H, CH), 3.75 (dd, J = 14.2, 5.6 Hz, 1H, CH_2), 3.65 (dd, J = 14.2, 6.5 Hz, 1H, CH_2), 2.61 (s, 3H, CH_3), 2.46 (s, 3H, CH_3), 2.43 (s, 3H, CH_3), 1.32 (d, J = 6.3 Hz, 3H, CH_3). MS (ESI) calculated for $C_{25}H_{27}NO_6S_2$ 501.1, found $(M + H)^+$ 502.2.

3.2.2.6 *N*-(4-Chlorophenyl)-4-methyl-*N*-(2-tosyloxypropyl)benzenesulfonamide (3c)

Following similar procedures as described for the preparation of **3a** by starting with **2c** (353 mg, 1.04 mmol), *p*-toluenesulfonyl chloride (297 mg, 1.56 mmol), trimethylamine hydrochloride

(99.3 mg, 1.04 mmol), and diisopropylethylamine (0.36. mL, 2.08 mmol), 416 mg (91%) of **3c** was obtained as a white solid after chromatographed on silica gel using 17:83 ethyl acetate/hexane. mp: 150-151 °C ^{1}H NMR ($CDCl_3$) δ 7.67 (d, J = 8.2 Hz, 2H, Ar–H), 7.39 (d, J = 8.2 Hz, 2H, Ar–H), 7.31 (d, J = 8.1 Hz, 2H, Ar–H), 7.27 – 7.18 (m, 4H, Ar–H), 6.84 (d, J = 8.7 Hz, 2H, Ar–H), 4.75 – 4.55 (m, 1H, CH), 3.69 (dd, J = 14.1, 5.5 Hz, 1H, CH_2), 3.60 (dd, J = 14.1, 6.5 Hz, 1H, CH_2), 2.46 (s, 3H, CH_3), 2.43 (s, 3H, CH_3), 1.33 (d, J = 6.3 Hz, 3H, CH_3). MS (ESI) calculated for $C_{23}H_{24}ClNO_5S_2$ 493.1, found $(M + H)^+$ 494.1.

3.2.2.7 *N*-(2-Fluoropropyl)-4-methyl-*N*-(4-methylphenyl)benzenesulfonamide (4a)

A solution of **3a** (614 mg, 1.30 mmol) in THF (5 mL) was added to tetrabutylammonium fluoride (1M solution in THF, 3 mL). The resulting solution was heated at 50 °C overnight. After volatile solvent was removed under reduced pressure, the residue was dissolved in diethyl ether (100 mL), and washed with water (100 mL). The diethyl ether layer was dried with anhydrous $MgSO_4$, concentrated under reduced pressure, and chromatographed on silica gel using 15:85 ethyl acetate/hexane to obtain the desired product **4a** as a white solid (27 mg, 6.5%), mp: 64-65°C. ^{1}H NMR ($CDCl_3$) δ 7.49 (d, J = 8.2 Hz, 2H, Ar–H), 7.26 (d, J = 8.1 Hz, 2H, Ar–H), 7.11 (d, J = 8.1 Hz, 2H, Ar–H), 6.95 (d, J = 8.2 Hz, 2H, Ar–H), 4.91 – 4.52 (m, 1H, CH), 3.85 – 3.52 (m, 2H, CH_2), 2.43 (s, 3H, CH_3), 2.34 (s, 3H, CH_3), 1.35 (dd, J = 23.7, 6.3 Hz, 3H, CH_3). MS (ESI) calculated for $C_{17}H_{20}FNO_2S$ 321.1, found $(M + H)^+$ 322.3.

3.2.2.8 *N*-(4-Acetylphenyl)-*N*-(2-fluoropropyl)-4-methylbenzenesulfonamide (4b)

A solution of diethylaminosulfur trifluoride (0.387 mL, 1.78 mmol) in CH_2Cl_2 (2 mL) was added dropwise to a solution of **2b** (310 mg, 0.89 mmol) in anhydrous CH_2Cl_2 (10 mL). After stirring at room temperature overnight, the solution was diluted with CH_2Cl_2 (80 mL) and washed with saturated $NaHCO_3$ aqueous solution (100 mL). The CH_2Cl_2 layer was dried with anhydrous $MgSO_4$, concentrated under reduced pressure, and chromatographed on silica gel using 25:75 ethyl acetate/hexane to obtain the desired product **4b** as a white solid (73.2 mg, 23%), mp: 97-99°C. ^{1}H NMR ($CDCl_3$) δ 7.91 (d, J = 8.5 Hz, 2H, Ar–H), 7.46 (d, J = 8.2 Hz, 2H, Ar–H), 7.34 – 7.12 (m, 4H, Ar–H), 4.98 – 4.60 (m, 1H, CH), 3.90 – 3.60 (m, 2H, CH_2), 2.61 (s, 3H, CH_3), 2.43

(s, 3H, CH_3), 1.36 (dd, J = 23.7, 6.3 Hz, 3H, CH_3). MS (ESI) calculated for $C_{18}H_{20}FNO_3S$ 349.1, found $(M + H)^+$ 350.2.

3.2.2.9 *N*-(4-Chlorophenyl)-*N*-(2-fluoropropyl)-4-methylbenzenesulfonamide (4c)

Following similar procedures as described for the preparation of **4b** by starting with **2c** (500 mg, 1.47 mmol) and diethylaminosulfur trifluoride (0.638 mL, 2.94 mmol), 219 mg (44%) of **4c** was obtained as a white solid after chromatography on silica gel using 16:84 ethyl acetate/hexane. mp: 73-74 °C ^{1}H NMR ($CDCl_3$) δ 7.48 (d, J = 8.2 Hz, 2H, Ar–H), 7.32 – 7.22 (m, 4H, Ar–H), 7.01 (d, J = 8.2 Hz, 2H, Ar–H), 4.93 – 4.56 (m, 1H, CH), 3.81 – 3.55 (m, 2H, CH_2), 2.44 (s, 3H, CH_3), 1.35 (dd, J = 23.7, 6.3 Hz, 3H, CH_3). MS (ESI) calculated for $C_{16}H_{17}ClFNO_2S$ 341.1, found $(M + H)^+$ 342.2.

3.2.3 Radiosyntheses of [^{18}F]4a-c

The proton-bombarded $H_2[^{18}O]O$ was transferred via He gas from the cyclotron target station to a Waters QMA light Sep-Pak cartridge set up in a hot cell. The ^{18}F-fluoride was trapped in the QMA cartridge, and eluted out into a 4-mL V-shaped reaction vial with a mixture of 0.1 mL $TBAHCO_3$ (0.5 M in CH_3CN, 0.1 mL), water (0.3 mL) and CH_3CN (0.6 mL). The uncapped reaction vial was placed in a heating block, and the solution was heated at 120 °C. After most of the solvents evaporated, CH_3CN (1 mL × 2) was added to the reaction vial to facilitate complete removal of water. A solution of tosylate precursor **3a-c** (3 mg) in DMF (0.5 mL) was added to the reaction vial. The vial was capped, and the mixture was heated at 125 °C for 20 min. At the end of heating, the mixture was diluted with water (1 mL) and purified by HPLC using the semi-preparative column eluted with 65% CH_3CN in water at a flow rate of 4.5 mL/min for [^{18}F]**4a** and [^{18}F]**4c**, or 55% CH_3CN at a flow rate of 4.5 mL/min for [^{18}F]**4b**. The retention times of [^{18}F]**4a-c** were 14.6, 15.2, and 14.9 min, respectively. The eluting fraction containing the desired ^{18}F-labeled tracer was collected, diluted with water (50 mL), and trapped on a Waters tC18 light Sep-Pak cartridge. After washing the tC18 light Sep-Pak cartridge with water (10 mL), ^{18}F-labeled tracer was eluted out with ethanol (0.4 mL), and formulated with saline (4 mL) for plasma stability, biodistribution, and μPET/CT imaging studies. Quality control was performed by HPLC on the analytical column eluted with 65% CH_3CN in water at a flow rate of 2.0

mL/min for [^{18}F]**4a** and [^{18}F]**4c**, and 55% CH_3CN in water at a flow rate of 2.0 mL/min for [^{18}F]**4b**. The retention times of [^{18}F]**4a-c** were 7.12, 8.14, and 8.17 min, respectively. The specific activities of [^{18}F]**4a-c** were measured using the analytical HPLC system. It was calculated by dividing the injected radioactivity in 0.2 mL of final ^{18}F-labeled tracer solution by the mass of the tracer in the injected solution. The mass of the tracer was estimated by comparing the UV absorbance obtained from the injection with a previously prepared standard curve.

3.2.4 Stability in Mouse Plasma

100 µL aliquots of [^{18}F]**4a-c** were incubated with 400 µL of BALB/c mouse plasma (available from Innovative Research) for 5, 15, 30, 60, and 120 minutes at 37 °C. At the end of each incubation period, samples were passed through a 0.45 micron filter. The filtered samples were loaded onto the analytical radio-HPLC to check for the presence of metabolite(s), and analyses were conducted with Agilent ChemStation software.

3.2.5 $LogD_{7.4}$ Measurements

$LogD_{7.4}$ was determined according to previously published procedures[193]. Briefly, an aliquot of ^{18}F-labeled tracer was added to a vial containing 2.5 ml of octanol and 2.5 ml of 0.1 M phosphate buffer (pH=7.4). The mixture was vortexed for 2 min and then centrifuged at 5,000 rpm for 2 min. A sample of the octanol (0.1 ml) and buffer (1 ml) layers was taken and counted in a well-type counter. $LogD_{7.4}$ was calculated using the following equation: $LogD_{7.4} = \log_{10}$ [((counts in octanol phase) × 10)/(counts in buffer phase)]. The major portion of the octanol layer (2.0 ml) was diluted with 0.5 ml of octanol and mixed with a fresh portion of 2.5 ml of phosphate buffer. The equilibration procedure described above was repeated until a constant value of $LogD_{7.4}$ was obtained.

3.2.6 In Vivo Experiments

Mice were maintained and in vivo experiments were conducted in accordance with the guidelines established by the Canadian Council on Animal Care and approved by the Animal Ethics Committee of the University of British Columbia.

3.2.6.1 Tumour Implantation

All experiments were performed using NOD.Cg-*Prkdc*^{scid}*Il2rg*^{tm1Wjl}/SzJ (NSG) mice bred in-house at the Animal Research Centre, British Columbia Cancer Research Centre, Vancouver, Canada. Mice were anesthetized briefly with 2.5% isoflurane in 2.0 L/min of oxygen during cells implantation. After wiping skin surrounding the injection site with an alcohol prep pad, a 31-Gauge needle was used to subcutaneously implant 5 x 10^6 HT-29 cells (in 100 µL of 1 x PBS and BD Matrigel Matrix at 1:1 ratio) under the right shoulder. Biodistribution studies and PET/CT imaging were performed when tumours reached 5-7mm in diameter.

3.2.6.2 PET Imaging and Biodistribution Studies

Under anesthesia, 3.7-7.4 MBq of ^{18}F-labeled tracer was administered intravenously through the caudal vein into HT-29 tumour bearing mice (n = 4 per tracer). CT scan was performed before a PET dynamic image sequence of 55 minutes. PET data were acquired in list mode acquisition. At 1 h p.i. mice were euthanized by CO_2 asphyxiation followed by cervical dislocation. Tissues of interest (blood, fat, intestine, stomach, spleen, liver, pancreas, kidney, lung, heart, muscle, bone, brain, and tumour) were harvested. Tissues of interest were rinsed with saline (exception of blood), blotted dry, weighed and counted to determine the percentage of injected dose per gram (%ID/g) of tissue. The PET data were reconstructed using the 3d-OSEM-MAP algorithm with CT-based attenuation correction. 3D regions of interest (ROI) were placed on the reconstructed images to determine the %ID/g of tissue using the Inveon Research Workplace software (IRW).

3.3 Results and Discussion

The synthesis of standards **4a-c** and their respective radiolabeling tosylate precursors **3a-c** are illustrated in Figure 3.2. The starting sulfonamides **1a-c** were prepared according to published procedures[191]. Coupling of sulfonamides **1a-c** with excess propylene oxide in DMF in the presence of K_2CO_3 as base afforded the desired secondary alcohols **2a-c** in excellent yield (92-99%). Initially, we attempted to prepare mesylate precursors for radiolabeling. However, we found out that it was difficult to separate the desired mesylates from their respective alcohol

reactants **2a-c** by flash column chromatography. Therefore, tosylate precursors were prepared instead as they could be easily separated from respective alcohol reactants **2a-c** due to the additional benzene on their structures. By using diisopropylethylamine as the base and trimethylamine hydrochloride as the catalyst[194], the reaction of alcohols **2a-c** with *p*-toluenesulfonyl chloride proceeded smoothly in CH_2Cl_2, and provided the desired tosylate precursors **3a-c** in 77-91% yield. Previously, standards **4a-c** were prepared by the reaction of HF/SbF_5 with their respective *N*-allylic intermediates[191]. However, due to safety concern with HF, different strategies for the preparation of standards **4a-c** were investigated. For the preparation of **4a**, tosylate **3a** was refluxed in THF in the presence of excess tetrabutylammonium fluoride (TBAF). However, the yield (6.5%) of desired product **4a** was low due to the formation of elimination by-product. Therefore, standards **4b-c** were prepared by directly converting alcohols **2b-c** to fluorides using diethylaminosulfur trifluoride (DAST), and better yields (23-44%) of **4b-c** were obtained.

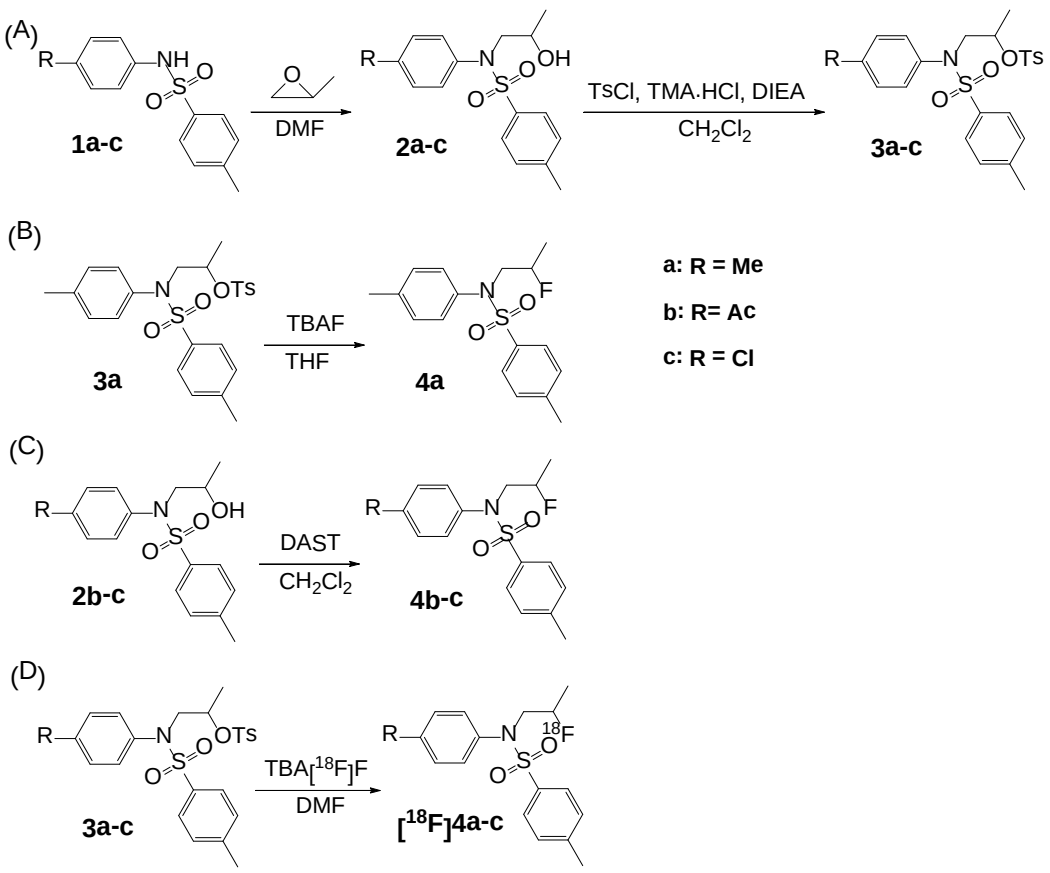

Figure 3.2 Syntheses of (A) precursors 3a-c and (B-C) standards 4a-c of tertiary sulfonamide CA-IX inhibitors, and (D) their ^{18}F-labeled analogs [^{18}F]4a-c.

As illustrated in Figure 3.2 (part D), the radiofluorination of [^{18}F]**4a-c** was performed via aliphatic nucleophilic substitution reactions between tosylate precursors **3a-c** and TBA[^{18}F]F in DMF at 125 °C. After HPLC purification, [^{18}F]**4a-c** were obtained in 7.1 - 43% decay-corrected yields with > 99% radiochemical purity, and > 740 GBq/μmol specific activity at the end of synthesis (~100 min). The stability of [^{18}F]**4a-c** was determined in mouse plasma, and no detectable metabolites of [^{18}F]**4a-c** were observed by HPLC analysis after 2 h incubation at 37 °C. The $logD_{7.4}$ (D: distribution coefficient) values of [^{18}F]**4a-c** were 3.45 ± 0.04, 3.05 ± 0.01, and 3.51 ± 0.27, respectively, as measured using the traditional shake flask method. These values were used to assess if [^{18}F]**4a-c** could cross cell membrane freely, and potentially bind to intracellular off targets CA-I and -II which are expressed abundantly in erythrocytes[181, 182]. Since the molecular weights (MW) and $logD_{7.4}$ values of **4a-c** are in the range of 321-349 Daltons, and 3.05-3.51, respectively, they are likely to be cell permeable according to the Lipinski's rule of five (MW < 500 and $logD_{7.4}$ < 5)[195].

Table 3.1 Biodistribution data (1 h p.i.; n = 4) of [^{18}F]**4a-c** in NSG mice bearing HT-29 human colorectal tumour xenografts.

Tissues/Organs	**Radiotracers**		
	[^{18}F]**4a**	[^{18}F]**4b**	[^{18}F]**4c**
Blood	0.58 ± 0.49	0.37 ± 0.11	0.98 ± 0.36
Fat	0.76 ± 0.55	1.48 ± 0.53	0.94 ± 0.51
Intestine	7.47 ± 7.46	16.7 ± 5.85	2.64 ± 0.26
Stomach	1.35 ± 2.21	1.25 ± 0.98	0.40 ± 0.16
Spleen	0.68 ± 0.53	0.82 ± 0.23	0.81 ± 0.35
Liver	9.77 ± 8.43	3.35 ± 1.72	3.57 ± 1.80
Pancreas	0.81 ± 0.83	0.75 ± 0.26	0.61 ± 0.20
Kidney	1.68 ± 1.66	2.03 ± 0.65	2.34 ± 1.04
Lungs	1.22 ± 0.90	1.46 ± 1.07	1.51 ± 0.42
Heart	0.59 ± 0.46	0.48 ± 0.11	0.93 ± 0.38
Muscle	0.52 ± 0.47	0.51 ± 0.18	0.92 ± 0.50
Bone	0.91 ± 0.70	2.72 ± 0.57	12.61 ± 5.18
Brain	0.32 ± 0.28	0.20 ± 0.06	0.33 ± 0.05
Tumour	0.51 ± 0.45	0.59 ± 0.29	0.98 ± 0.48

Values (%ID/g) are presented as mean ± SD

To evaluate the potential of [^{18}F]**4a-c** for imaging CA-IX expression, biodistribution and PET imaging studies were performed in mice bearing HT-29 human colorectal tumour xenografts. As shown in Table 3.1, fast blood clearance of [^{18}F]**4a-c** was observed with only 0.58 ± 0.49, 0.37 ± 0.11, and 0.98 ± 0.36 %ID/g, respectively, retained in blood at 1 h p.i. These numbers are substantially lower than the previously reported 13.92 ± 3.07 %ID/g obtained with ^{18}F-labeled U-104[196] indicating no significant binding of [^{18}F]**4a-c** to the intracellular off target CA-II. However, the uptake of [^{18}F]**4a-c** in HT-29 tumours did not improve as only 0.51 ± 0.45, 0.59 ± 0.29, and 0.98 ± 0.48 %ID/g, respectively, were observed at 1 h p.i. The majority of [^{18}F]**4a-b** radioactivity was excreted via the hepatobiliary pathway reflecting the lipophilic nature of these two radiotracers. For [^{18}F]**4c** very high bone uptake (12.61 ± 5.18 %ID/g at 1 h p.i.) was observed which indicated extensive defluorination of [^{18}F]**4c** in vivo. However, it is unclear at this stage why it was [^{18}F]**4c** but not [^{18}F]**4b** that resulted in massive defluorination. Based on their chemical structures, the 4-acetyl group in **4b** is the most electron-withdrawing group followed by the 4-chloro group in **4c**, and the 4-methyl group in **4a**. Presumably, the 4-acetyl group would make the nitrogen of sulfonamide **4b** more electron deficient, and the adjacent fluoro a better leaving group, resulting in a higher degree of in vivo defluorination. Although bone uptake of [^{18}F]**4b** was higher than [^{18}F]**4a** (2.72 ± 0.57 vs. 0.91 ± 0.70 %ID/g at 1 h p.i.), these numbers were much lower than 12.61 ± 5.18 %ID/g obtained by using [^{18}F]**4c** suggesting other factors might contribute to the in vivo defluorination of these compounds. Since the uptake of [^{18}F]**4a-c** in HT-29 tumours was not significantly higher than the uptake values in the surrounding tissues (blood, fat, muscle and bone), no clear tumour visualization was obtained from the PET images (Figure 3.3).

Compounds **4a-c** were explored for imaging CA-IX expression in HT-29 tumours because they were reported to have nanomolar binding affinity for CA-IX, and most importantly to be the first sulfonamides to show no interaction with CA-II in CO_2 hydration assays (Table 3.2). The binding of **4a-c** to CA-XII could be beneficial as CA-XII, a transmembrane protein, is also up-regulated in hypoxic tumours[197]. Cytosolic CA-I and -II are expressed in large quantities in erythrocytes[153, 154] and the binding of CA-IX-targeting tracers to CA-I and -II would reduce imaging contrast. Previously, we observed slow blood clearance of ^{18}F-labeled U-104 presumably due to binding with CA-II (K_i = 95 nM, Table 3.1)[196]. In this study, we did not

observe much retention of [^{18}F]**4a-c** in blood at 1 h p.i. despite their suitable physical characteristics (neutral, lipophilic, and with MW < 500 Daltons) to cross cell membrane, and good binding affinity to CA-I (K_i = 73.1 – 89.1 nM, Table 3.2). Possible explanations for the low tumour uptake and blood retention of [^{18}F]**4a-c** could be due to relatively fast metabolism and/or blood clearance of these tracers, and in the case of [^{18}F]**4c**, rapid in vivo defluorination.

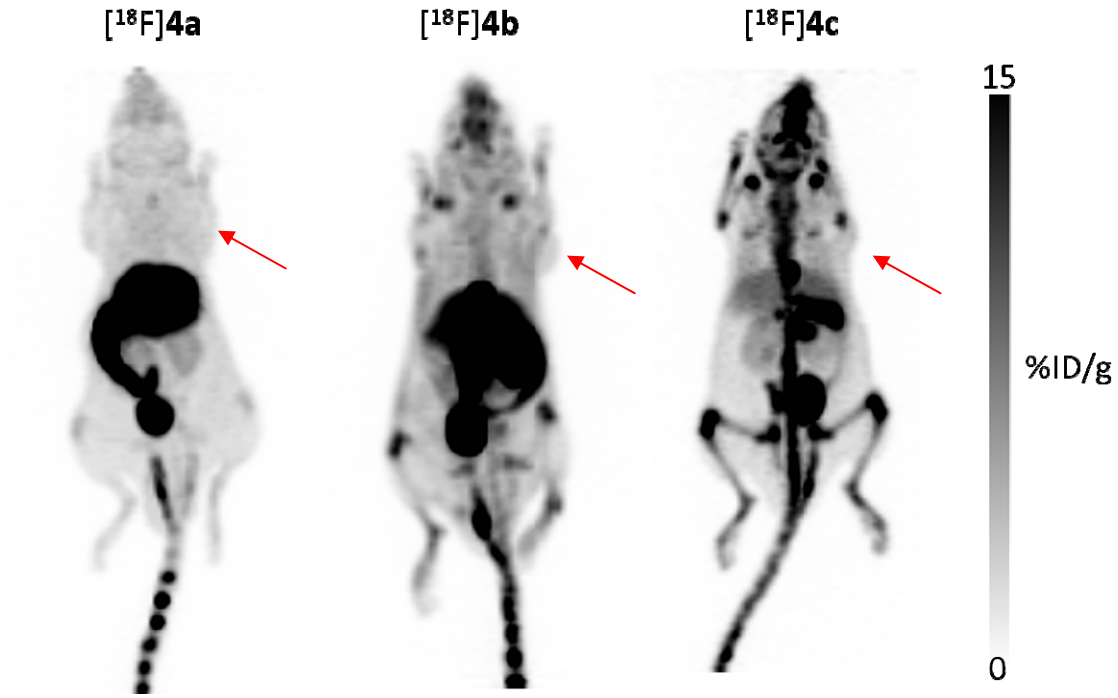

Figure 3.3 Representative PET maximum intensity projection images of [^{18}F]4a-c at 1 h p.i. in NSG mice bearing CA-IX expressing HT-29 human colorectal tumour xenografts. Arrows indicate location of the tumours.

Although no small sulfonamide-based radiotracers have been reported to visualize CA-IX-expressing tumours in preclinical imaging studies, a successful optical imaging probe HS680 is already commercially available. HS680, a conjugate of acetazolamide and the near-infrared fluorochrome VivoTag 680 developed by PerkinElmer, showed impressive 10% injected dose accumulation in HT-29 tumour xenografts in mice at 24 h p.i.[163]. Acetazolamide is a promiscuous CA inhibitor, and therefore the derivatives of acetazolamide including HS680 are expected to have good binding affinity to most CAs including the intracellular isoenzymes I and II (Table 3.2). However, the conjugation of acetazolamide with the highly charged and bulky

(MW > 1,000 Daltons) VivoTag 680 prevents it from crossing the cell membrane and binding to intracellular off targets. The success of HS680 could be a valuable lesson for the future design of radiotracers for imaging CA-IX expression with PET or SPECT. Instead of radiolabeling CA-IX-specific inhibitors which may be difficult to synthesize, the design of cell-impermeable sulfonamide-based radiotracers represents an easier and quicker solution. This could be achieved, for example, by conjugating the CA-targeting sulfonamide moiety with a polyaminocarboxylate chelator for labeling with radiometal such as ^{68}Ga, ^{64}Cu, or ^{111}In for imaging. The radiometal-polyaminocarboxylate-chelator complexes are generally highly hydrophilic and charged, and would prevent the radiolabeled sulfonamide conjugates from entering cells. Another promising alternative is the use of a multivalent design. This approach combines several CA-targeting sulfonamides into one single molecule, which could potentially enhance binding affinity to CA-IX and afford cell impermeability from accumulation of MW.

Table 3.2 Reported inhibition constants (K_i, nM) of acetazolamide[178], HS680[162], U-104[178], and tertiary sulfonamides **4a-c**[191] to human CA isoenzymes I, II, IX and XII.

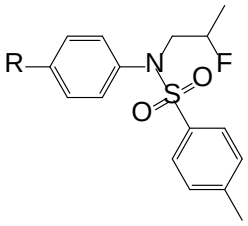

Compounds	CA-I	CA-II	CA-IX	CA-XII
acetazolamide	250	12	25	5.7
HS680	-	248	7.5	35
U-104	5,080	95	45	4.5
4a (R = Me)	73.1	Not active	9.3	33.6
4b (R = Ac)	89.1	Not active	9.6	83.8
4c (R = Cl)	77.3	Not active	9.1	100

Errors in the range of 5-10% of the reported value from three different assays.

3.4 Conclusion

In conclusion, we successfully synthesized and radiolabeled tertiary benzenesulfonamides **4a-c**, and evaluated their potential as CA-IX imaging agents. Despite their good affinity and selectivity for CA-IX, imaging and biodistribution data showed only minimal tumour uptake in xenograft mice relative to normal tissues. Therefore, [^{18}F]**4a-c** are not suitable for CA-IX targeted molecular imaging.

Chapter 4: Multivalent Approach to Achieve In Vivo Selectivity for CA-IX

4.1 Introduction

The application of small molecule inhibitors as PET tracers can be challenged by several effects such as non-specific uptake in cells, poor clearance from blood[198], and rapid metabolic defluorination with accompanying bone uptake[199, 200]. In addition, ^{18}F-labeling in high yield and at high specific activity often presents a significant challenge in the development of new PET tracers[201]. Yet even when conditions for clinically useful radiolabeling have been met, non-specific uptake due to association with off-target enzyme isoforms of greater abundance can result in images marked by low tumour to background ratios. Lipophilicity can also enhance non-specific uptake in some cases. As shown in Chapters 2 and 3, the development of CA-IX targeting agents can be hindered by a combination of these factors.

We hypothesized that a multivalent enzyme inhibitor would restrict intracellular accumulation and enhance specific binding to an extracellular tumour target. To accomplish this, we utilized a radiosynthon that readily enables grafting of various ligands to a pentaerythritol core while allowing for facile radiolabeling at high specific activity with Curie-levels of ^{18}F-activity. Recently, we communicated this method for linking both peptides and small molecule inhibitors in a trivalent motif[202]. Here we expand the application of this method to address the imaging potential of two related enzyme inhibitors and report detailed findings on how this method can be used to reduce nonspecific intracellular accumulation.

Adapted from: Trimeric Radiofluorinated Sulfonamide Derivatives to Achieve In Vivo Selectivity for Carbonic Anhydrase IX-Targeted Cancer Imaging. J Nuc Med, 2015;56(9): 1434-1440.

Joseph Lau[1*], Zhibo Liu[2*], Kuo-Shyan Lin[1], Jinhe Pan[1], Zhengxing Zhang[1], Daniella Vullo[3], Claudiu T. Supuran[3], David M. Perrin[2], Francois Benard[1]

[1] Department of Molecular Oncology, BC Cancer Research Centre, BC Cancer Agency, Vancouver, BC, Canada
[2] Department of Chemistry, University of British Columbia, Vancouver, BC, Canada
[3] Dipartimento Neurofarba and Laboratorio di Chimica Bioinorganica, Università degli Studi di Firenze, Florence, Italy

JL, KSL, DMP, and FB designed the study. JL, ZL, JP, ZZ, and DV were involved in the experiments. CTS provided the affinity measurements. JL and ZL were involved in acquisition of data and interpretation of the analysis. JL and ZL wrote the manuscript.

[*]Co-First Author

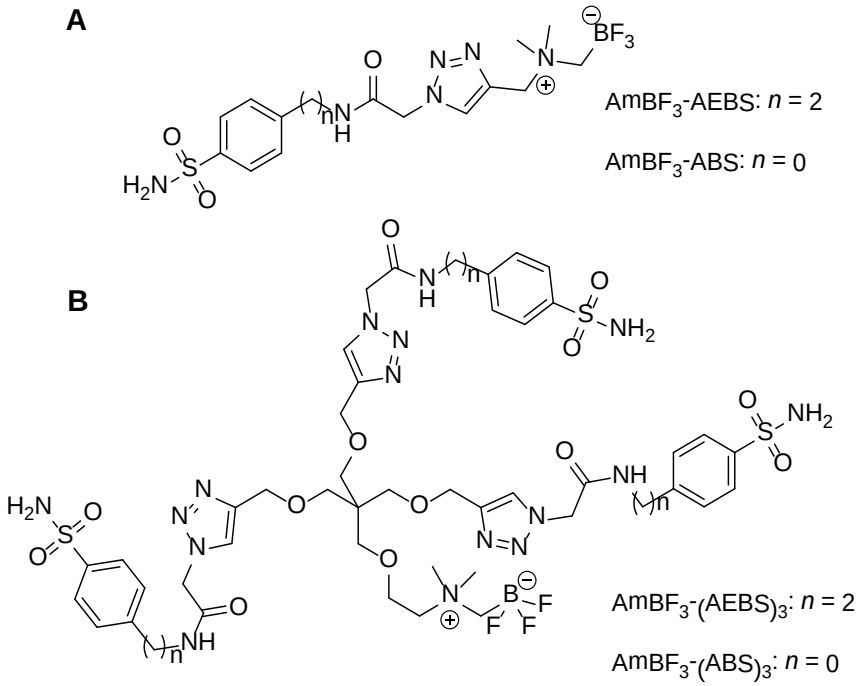

Figure 4.1 Chemical structures of ^{18}F-AmBF$_3$-AEBS, ^{18}F-AmBF$_3$-ABS, ^{18}F-AmBF$_3$-(AEBS)$_3$ and ^{18}F-AmBF$_3$-(ABS)$_3$. Tracers were radiolabeled with ^{18}F via an ^{18}F-^{19}F isotope exchange reaction for PET imaging.

Our previous attempt using ^{18}F-U-104 resulted in very high uptake in blood (13.97 ± 3.07 %ID/g at 1 h p.i.)[196] presumably due to the binding of ^{18}F-U-104 to intracellular off-targets CA-I and CA-II that are abundant in erythrocytes[203]. We hypothesized that cell-impermeant tracers would disfavor binding to intracellular CA isoforms, and in turn provide high contrast images. To do this we sought multivalent inhibitors to increase both avidity and molecular weight. In the present study, we synthesized and evaluated two monomeric (as controls) and two trimeric ^{18}F-labeled sulfonamides using 4-(2-aminoethyl)benzenesulfonamide (AEBS) and 4-aminobenzensulfonamide (ABS) as our pharmacophores for imaging CA-IX expression with PET (Figure 4.1). In terms of a radioprosthetic group, we chose the zwitterionic organotrifluoroborate[202], the polarity of which would likely further reduce lipophilicity and membrane permeability.

4.2 Methods and Materials

$AmBF_3$-conjugated alkyne **3**[204], $AmBF_3$-conjugated alkyne **4**[205], and 2-chloro-N-(4-sulfamoyl-phenyl)-acetamide[206] were prepared according to published procedures. Other chemicals were obtained from commercial sources, and used without further purification. ^{18}F-fluoride Trap & Release columns were purchased from ORTG Inc. (Oakdale, TN). C18 light Sep-Pak cartridges (1cc, 50 mg) were obtained from Waters (Milford, MA). BALB/c mouse plasma was obtained from Innovative Research (Novi, MI). Mass analyses were performed using a Bruker (Billerica, MA) Esquire-LC/MS system with ESI ion source. Purification and quality control of cold and ^{18}F-labeled sulfonamides were performed on an Agilent HPLC system equipped with a model 1200 quaternary pump, a model 1200 UV detector, and a Bioscan (Washington, DC) NaI scintillation detector. The radio-detector was connected to a Bioscan B-FC-1000 Flow-count system, and the output from the Bioscan Flow-count system was fed into an Agilent 35900E interface which converted the analog signal to digital signal. Operation of the Agilent HPLC system was controlled using the Agilent ChemStation software. Radioactivity of ^{18}F-labeled tracers was measured using a Capintec (Ramsey, NJ) CRC®-25R/W dose calibrator, and the radioactivity of mouse tissues collected from biodistribution studies were counted using a Packard (Meriden, CT) Cobra II 5000 Series auto-gamma counter.

4.2.1 HPLC Analysis

The following table lists the different HPLC conditions used during purification, QC and plasma stability assays.

Table 4.1 HPLC conditions for $AmBF_3$ sulfonamides.

Condition	Column	Solvent system (containing 0.1% TFA)	Flow rate (mL/min)
A	Phenomenex Luna C18, 5 µm, 10 × 250 mm semi-prep	11% CH_3CN in water	4.5
B	Phenomenex Luna C18, 5 µm, 10 × 250 mm semi-prep	10% CH_3CN in water	4.5
C	Agilent Eclipse XDB-C18, 5 µm, 9.2 × 250 mm semi-prep	0 to 5 min, 5 to 25% CH_3CN in water; 5 to 15 min, 25 to 45% CH_3CN in water	3.0
D	Agilent Eclipse XDB-C18, 5 µm, 9.2 × 250 mm semi-prep	0 to 5 min, 10 to 20% CH_3CN in water;5 to 15 min, 20 to 60% CH_3CN in water	3.0
E	Phenomenex Luna C18, 5 µm, 4.6 × 250 mm analytical	13% CH_3CN in water	2.0
F	Phenomenex Luna C18, 5 µm, 4.6 × 250 mm analytical	11% CH_3CN in water	2.0
G	Phenomenex Jupiter, 10 µm, C18 4.6 × 250 mm analytical	0 to 2 min, 5% CH_3CN in water; 2 to 7 min, 5 to 20% CH_3CN in water; 7 to 15 min, 20% CH_3CN in water to 100% CH_3CN	2.0
H	Phenomenex Luna C18, 5 µm, 10 × 250 mm semi-prep	14% CH_3CN in water	4.5
I	Phenomenex Luna C18, 5 µm, 10 × 250 mm semi-prep	12% CH_3CN in water	4.5

4.2.2 Synthesis of Azidoacetyl-AEBS (1)

A solution of azidoacetic acid (101 mg, 1.0 mmol), 1,3-dicyclohexylcarbodiimide (248 mg, 1.2 mmol) and N-hydroxysuccinimide (138 mg, 1.2 mmol) in DMF (2 mL) was stirred at room temperature for 1 h. After filtration, AEBS (220 mg, 1.1 mmol) in DMF (1 mL) was added. The resulting solution was stirred at room temperature overnight, diluted with water (25 mL), and extracted with DCM (125 mL). The organic layer was dried with anhydrous $MgSO_4$, concentrated under reduced pressure, and chromatographed on silica gel using 9:1 ethyl acetate/hexane to obtain the desired product as a white solid (210 mg, 74%). ESI-MS: calculated

for azidoacetyl-AEBS **1** $C_{10}H_{13}N_5O_3S$ 283.07, found $[M+H]^+$ 284.07. ^{1}H-NMR (CD_3CN-D_2O): δ 2.85 (t, 3.7 Hz, 2H), 3.47 (m, 4.4 Hz, 2H), 5.67 (s, 2H), 7.43 (d, 7.5 Hz, 2H), 7.78 (d, 7.5 Hz, 2H).

4.2.3 Synthesis of Azidoacetyl-ABS (2)

A mixture of 2-chloro-N-(4-sulfamoyl-phenyl)-acetamide (353 mg, 1.4 mmol) and sodium azide (102 mg, 1.6 mmol) in DMSO (5 mL) was stirred at room temperature overnight. The reaction mixture was diluted with water (12.5 mL) and extracted with ether (75 mL). The organic layer was dried with anhydrous $MgSO_4$, concentrated under reduced pressure, and recrystallized with water to obtain the desired product as a white solid (313 mg, 60%). ESI-MS: calculated for azidoacetyl-ABS **2** $C_8H_9N_5O_3S$ 255.04, found $[M+H]^+$ 256.04. ^{1}H-NMR (DMSO-d_6): δ 4.07 (s, 2H), 7.25 (s, 2H), 7.75 (m, 4H), 10.5 (s, 1H).

4.2.4 Synthesis of AmBF$_3$-AEBS

A 1.5-mL Eppendorf tube was loaded with AmBF$_3$-conjugated alkyne **3** (10 mg, 61 μmol), azidoacetyl-AEBS **1** (10 mg, 35 μmol), aqueous $CuSO_4$ (1.0 M, 56.3 μL), sodium ascorbate (1.0 M, 140.7 μL) and DMF (150 μL). This mixture was allowed to react at 45 °C for 2 h and then purified by HPLC (Condition **A**, t_R = 22.3 min) to obtain AmBF$_3$-AEBS in 41% yield. ESI-MS: calculated for AmBF$_3$-AEBS $C_{16}H_{24}BF_3N_6O_3S$ 448.2, found $[M+Na]^+$ 471.2. ^{1}H-NMR (DMSO-d_6): δ 2.23 (m, 2H), 2.50 (m, 2H), 2.82 (t, 7.1 Hz, 2H), 2.93 (s, 6H), 4.53 (s, 2H), 5.16 (s, 2H), 7.31 (s, 2H), 7.41 (d, 8.3 Hz, 2H), 7.75 (d, 8.3 Hz, 2H), 8.30 (s, 1H), 8.48 (t, 5.5 Hz, 1H).

4.2.5 Synthesis of AmBF$_3$-ABS

A 1.5-mL Eppendorf tube was loaded with AmBF$_3$-conjugated alkyne **3** (10 mg, 61 μmol), azidoacetyl-ABS **2** (10 mg, 39 μmol), aqueous $CuSO_4$ (1.0 M, 62.7 μL), sodium ascorbate (1.0 M, 156.8 μL) and DMF (150 μL). This mixture was allowed to react at 45 °C for 2 h and then purified by HPLC (Condition **B**, t_R = 22.1 min) to obtain AmBF$_3$-ABS in 40% yield. ESI-MS: calculated for AmBF$_3$-ABS $C_{14}H_{20}BF_3N_6O_3S$ 420.1, found $[M+Na]^+$ 443.2. ^{1}H-NMR (DMSO-

d_6): δ 2.24 (m, 2H), 2.95 (s, 6H), 4.57 (s, 2H), 5.47 (s, 2H), 7.27 (s, 2H), 7.76 (q, 8.0 Hz, 9.0 Hz, 4H), 8.41 (s, 1H), 10.86 (s, 1H).

4.2.6 Synthesis of $AmBF_3$-$(AEBS)_3$

A 1.5-mL Eppendorf tube was loaded with $AmBF_3$-conjugated alkyne **4** (5 mg, 12.3 μmol), azidoacetyl-AEBS **1** (12.1 mg, 44 μmol), aqueous $CuSO_4$ (1.0 M, 5 μL), sodium ascorbate (1.0 M, 12.5 μL) and 5% NH_4OH (in 1:1 CH_3CN/H_2O, 50 μL). This mixture was allowed to react at 45 °C for 2 h and then purified by HPLC (Condition **C**, t_R = 12.8 min) to obtain $AmBF_3$-$(AEBS)_3$ in 47% yield. ESI-MS: calculated for $AmBF_3$-$(AEBS)_3$ $C_{49}H_{68}BF_3N_{16}O_{13}S_3$ 1252.44, found $[M+H]^+$ 1253.49. ^{1}H-NMR (CD_3CN-D_2O): δ 2.71 (s, 2H), 2.88 (m, 8H), 3.17 (s, 6H), 3.47 (q, 4.4 Hz, 6H), 3.63 (t, 2.7 Hz, 2H), 3.80 (s, 8H), 4.19 (s, 6H), 5.67 (s, 6H), 7.43 (d, 7.4 Hz, 2H), 7.78 (d, 7.4 Hz, 2H).

4.2.7 Synthesis of $AmBF_3$-$(ABS)_3$

A 1.5-mL Eppendorf tube was loaded with $AmBF_3$-conjugated alkyne **4** (5 mg, 12.3 μmol), azidoacetyl-ABS **2** (11.0 mg, 44 μmol), aqueous $CuSO_4$ (1.0 M, 5 μL), sodium ascorbate (1.0 M, 12.5 μL) and 5% NH_4OH (in 1:1 CH_3CN/H_2O, 50 μL). The mixture was allowed to react at 45 °C for 2 h, and then purified by HPLC (Condition **D**, t_R = 13.1 min) to obtain $AmBF_3$-$(ABS)_3$ in 55% yield. ESI-MS: calculated for $AmBF_3$-$(ABS)_3$ $C_{43}H_{56}BF_3N_{16}O_{13}S_3$ 1168.34, found $[M+H]^+$ 1169.40 ^{1}H-NMR (CD_3CN-D_2O): δ 4.16 (s, 6H), 4.30 (s, 2H), 4.61 (m, 4H), 4.72 (s, 8H), 5.77 (s, 6H), 6.54 (s, 6H), 8.94 (d, 9.0 Hz, 6H), 9.03 (d, 9.0 Hz, 6H), 9.16 (s, 3H).

4.2.8 Binding Affinity Measurements

Inhibition constants (K_i) of $AmBF_3$-AEBS, $AmBF_3$-ABS, and $AmBF_3$-$(AEBS)_3$ and $AmBF_3$-$(ABS)_3$ for CA-I, -II, -IX and -XII were determined using the CA catalyzed CO_2 hydration stopped-flow assays following published procedures[178].

4.2.9 Radiolabeling

100-150 nmol of ^{19}F-AmBF$_3$-AEBS, ^{19}F-AmBF$_3$-ABS, ^{19}F-AmBF$_3$-(AEBS)$_3$ or ^{19}F-AmBF$_3$-(ABS)$_3$ was resuspended with aqueous pyridazine-HCl buffer (15-20 μL, 1M, pH = 2) and DMF (15-20 μL) in a polypropylene tube. No carrier-added ^{18}F-fluoride was obtained by bombardment of $H_2{}^{18}O$ with 18 MeV protons, followed by trapping on an anion exchange column (9 mg, QMA, chloride form). The ^{18}F-fluoride was eluted off with saline (100 μL) into the reaction vial. The reaction mixture was heated at 80 °C for 20 min, and quenched with 5% aqueous NH_4OH (2 mL). The quenched solution was loaded onto a C18 light Sep-Pak cartridge. ^{18}F-Fluoride was removed by washing the cartridge with DI water (5 mL × 2). ^{18}F-AmBF$_3$-AEBS, ^{18}F-AmBF$_3$-ABS, ^{18}F-AmBF$_3$-(AEBS)$_3$ or ^{18}F-AmBF$_3$-(ABS)$_3$ was eluted off the cartridge with 0.5 mL 4:1 ethanol/saline and diluted with saline (5 mL) for stability and biodistribution/imaging studies. Samples were removed for QC analysis by HPLC using Condition **E** for ^{18}F-AmBF$_3$-AEBS (t_R = 8.0 min), Condition **F** for ^{18}F-AmBF$_3$-ABS (t_R = 7.9 min), or Condition **G** for ^{18}F-AmBF$_3$-(AEBS)$_3$ (t_R = 12.4 min) and ^{18}F-AmBF$_3$-(ABS)$_3$ (t_R = 11.9 min).

4.2.10 Stability in Mouse Plasma

20 μL of ^{18}F-AmBF$_3$-AEBS, ^{18}F-AmBF$_3$-ABS, ^{18}F-AmBF$_3$-(AEBS)$_3$ or ^{18}F-AmBF$_3$-(ABS)$_3$ was added to mouse plasma (500 μL) and incubated at 37 °C for 2 h. The reaction was quenched by adding 1 mL CH_3CN to the plasma solution. The quenched solution was centrifuged, and the supernatant was collected, filtered and analyzed by HPLC using Condition **H** for ^{18}F-AmBF$_3$-AEBS (t_R = 13.0 min), Condition **I** for ^{18}F-AmBF$_3$-ABS (t_R = 15.4 min), or Condition **G** for ^{18}F-AmBF$_3$-(AEBS)$_3$ (t_R = 12.4 min) and ^{18}F-AmBF$_3$-(ABS)$_3$ (t_R = 11.9 min).

4.2.11 LogD$_{7.4}$ measurements

An aliquot of ^{18}F-AmBF$_3$-AEBS, ^{18}F-AmBF$_3$-ABS, ^{18}F-AmBF$_3$-(AEBS)$_3$ or ^{18}F-AmBF$_3$-(ABS)$_3$ was added to a Falcon tube containing 4 mL of octanol and 1.5 mL of phosphate buffer (0.1 M, pH = 7.4). The mixture was vortexed for 2 min and centrifuged at 5,000 rpm for 2 min. Samples of the octanol (3.5 mL) and buffer (1 mL) layers were taken and counted. LogD$_{7.4}$ was calculated using the following equation: $LogD_{7.4} = \log_{10}[(\text{counts in octanol phase}/3.5)/(\text{counts in buffer}$

phase)]. The major portion of the phosphate buffer layer (1 mL) was diluted with 0.5 mL of phosphate buffer and mixed with octanol (4 mL). The equilibration procedure described above was repeated until a constant value of $LogD_{7.4}$ was obtained.

4.2.12 In Vivo Experiments

4.2.12.1 Cell Line and Animal Model

All animal studies were performed in accordance with the Canadian Council on Animal Care guidelines and approved by the Animal Care Committee of the University of British Columbia. HT-29 human colorectal cancer cells were obtained as a gift from Dr. Donald Yapp (BC Cancer Research Centre, Vancouver, Canada). HT-29 cells were cultured in Dulbecco's Modified Eagle's Medium supplemented with 10% fetal bovine serum 100 U/mL penicillin-streptomycin, and non-essential amino acids. Male NOD.Cg-*Prkdc*^{scid}*Il2rg*^{tm1Wjl}/SzJ (NSG) mice bred in-house at the Animal Research Centre, BC Cancer Research Centre were used. Mice were subcutaneously inoculated with 5×10^6 HT-29 cells in the right dorsal flank. Biodistribution studies and PET/CT imaging were performed when tumours reached 7-9 mm in diameter.

4.2.12.2 Biodistribution Studies

Tumour bearing mice were injected with ~ 0.37 MBq of ^{18}F-labeled tracer (100 – 200 µL in saline, i.v.). For blocking experiments, mice were intravenously pre-injected with 10 mg/kg acetazolamide 1 h (100 – 200 µL in saline, i.v.) before administering the radiotracer. After an uptake period of 0.5, 1, or 2 h, mice were euthanized by CO_2 asphyxiation. Blood was promptly withdrawn, and organs/tissues of interest were harvested, rinsed with saline, blotted dry and weighed. Radioactivity in collected tissues was counted, normalized to the injected dose and expressed as the percentage of the injected dose per gram of tissue (%ID/g).

4.2.12.3 PET/CT Imaging

Imaging experiments were performed using a Siemens (Erlangen, Germany) Inveon micro PET/CT scanner. Tumour bearing mice were injected with ~ 3.7 MBq of ^{18}F-labeled tracer (100 – 200 µL in saline, i.v.). For blocking experiments, mice were intravenously pre-injected with 10

mg/kg acetazolamide 1 h (100 – 200 µL in saline, i.v.) before administering the radiotracer. At 0.5, 1, or 2 h p.i., a 10-min PET acquisition scan was performed, which was preceded by a 10-min CT scan. Body temperature of mice was maintained at 37 °C with the use of thermal pads. PET data were acquired in list mode acquisition, reconstructed using the 3d-OSEM-MAP algorithm with CT-based attenuation correction, and co-registered for alignment. At the conclusion of the imaging study, mice were euthanized and processed for biodistribution as described above.

4.2.12.4 Data Analysis

All statistics were performed using Prism 6 software (GraphPad). For Table 4.3, *P* values for the difference of tracer uptake in mouse tissues between unblocked and blocked groups were calculated using a Student's *t*-test (unpaired, one-tailed) and values < 0.05 were considered statistically significant. For Figure 4.4, *P* values for the difference of tumour/muscle ratios between monomer and trimer were calculated using a Student's *t*-test (unpaired, two-tailed) and values < 0.05 were considered statistically significant.

4.3 Results and Discussion

The highly conserved catalytic domain of CA isoforms represents a major challenge for the design of CA-IX selective imaging agents[131]. Off-target binding to intracellular CAs can significantly reduce tumour binding and image contrast [203]. Strategies to confer CA-IX selectivity for small molecule inhibitors have focused on limiting transport across the plasma membrane. These include incorporating bulky entities like FITC, albumin-binders, sugar derivatives, or charged species to CA targeting pharmacophores[207-211]. Based on these findings, we initiated the development of multivalent PET tracers for imaging CA-IX expression in tumours.

Previously, our group reported the synthesis of a dual-mode imaging agent by coupling rhodamine and cycloRGD to an $AmBF_3$-conjugated alkyne **4** amendable for ^{18}F-labeling[212]. Using the modular adaptability of this synthon, we coupled three AEBS/ABS moieties via copper-catalyzed azide alkyne cycloaddition to target CA-IX expression. To the best of our knowledge, there are few examples of such multimeric inhibitors that have been labeled for

imaging and none has been labeled with ^{18}F nor used to visualize tumour-associated CA-IX activity. For comparison and as controls, we coupled AEBS/ABS to $AmBF_3$-conjugated alkyne **3** to synthesize monovalent tracers to determine if trimerization is essential to selectively target CA-IX in vivo.

The preparation of non-radioactive ^{19}F-$AmBF_3$-AEBS, ^{19}F-$AmBF_3$-ABS, ^{19}F-$AmBF_3$-$(AEBS)_3$, and ^{19}F-$AmBF_3$-$(ABS)_3$ followed synthetic schemes as shown in Figure 4.2. Azidoacetyl-AEBS **1** was obtained in 74% yield by coupling AEBS with azidoacetic acid, whereas azidoacetyl-ABS **2** was prepared in 60% yield by the displacement of the chloro group of 2-chloro-N-(4-sulfamoyl-phenyl)-acetamide with azide. The coupling of **1** and **2** to $AmBF_3$-conjugated alkyne **3** via the Cu^+-catalyzed click reaction afforded the desired $AmBF_3$-AEBS and $AmBF_3$-ABS in 41 and 40% yields, while coupling to alkyne **4** generated $AmBF_3$-$(AEBS)_3$ and $AmBF_3$-$(ABS)_3$ in 47 and 55% yields, respectively.

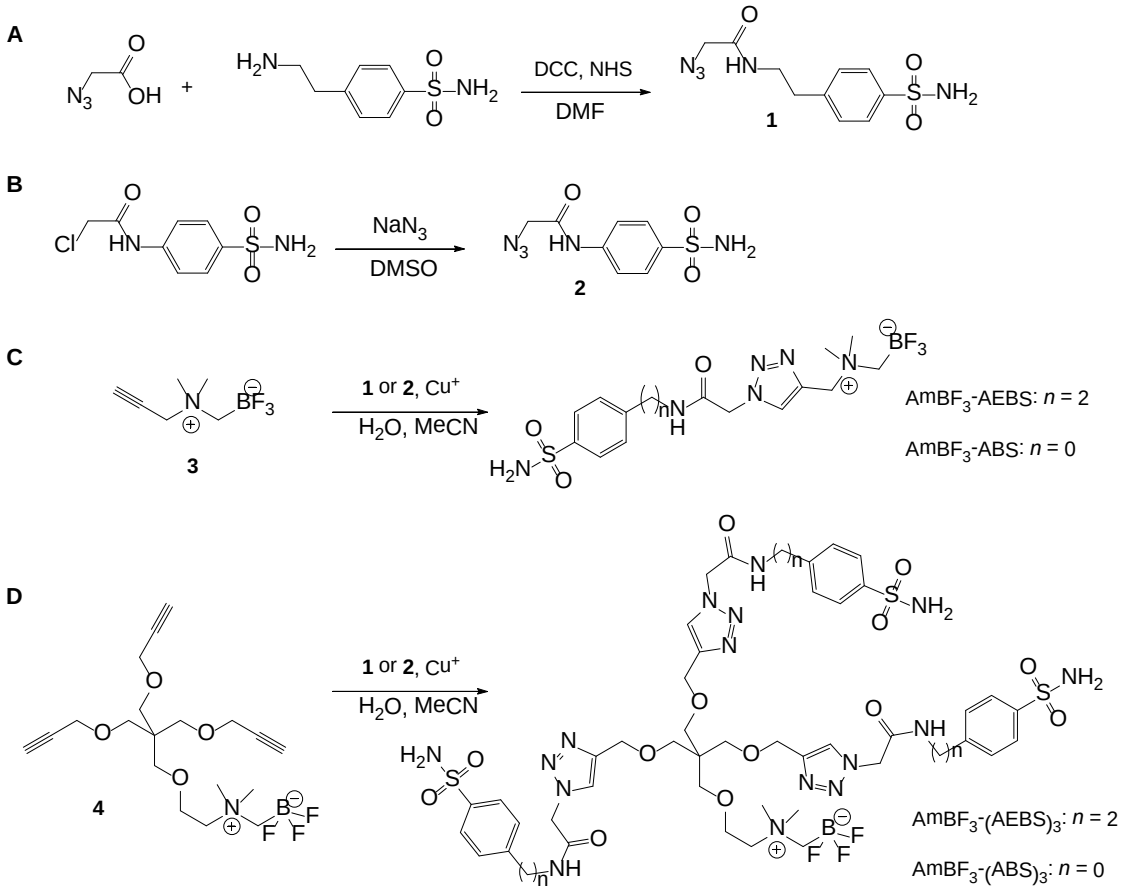

Figure 4.2 Synthesis of (A) azidoacetyl-AEBS 1, (B) azidoacetyl-ABS 2, (C) $AmBF_3$-AEBS and $AmBF_3$-ABS, and (D) $AmBF_3$-$(AEBS)_3$ and $AmBF_3$-$(ABS)_3$.

The binding affinities of the synthesized compounds to CA-I, -II, -IX and -XII are summarized in Table 4.2. Whereas more specific inhibitors can be designed to enhance selectivity to CA-IX, we sought to test the use of a trivalent scaffold with very simple and rather non-specific inhibitors to demonstrate that in vivo selectivity can be generated simply by altering cell-permeability of the tracer to reduce uptake in blood. AEBS and ABS are known to inhibit CA-IX; however, they by themselves lack isoform selectivity. According to literature, the K_i values of AEBS and ABS for CA-IX are 33 and 294 nM, respectively[213-215]. For reasons unknown, incorporation of AEBS or ABS into $AmBF_3$-conjugated radiosynthons resulted in consistent or significantly improved binding affinities for CA-IX. $AmBF_3$-AEBS and $AmBF_3$-ABS exhibited binding affinities of 8.0 and 6.6 nM, while $AmBF_3$-$(AEBS)_3$ and $AmBF_3$-$(ABS)_3$ had binding affinities of 35.7 and 8.5 nM. Despite retaining good binding affinity to CA-I and –II, the in vivo binding of bulky ^{18}F-$AmBF_3$-$(AEBS)_3$ and ^{18}F-$AmBF_3$-$(ABS)_3$ to these two intracellular off-target CA isoforms is highly unlikely. Trimerization of AEBS and ABS to form $AmBF_3$-$(AEBS)_3$ and $AmBF_3$-$(ABS)_3$ respectively, affords cell-impermeability due to the high molecular weight (> 1 kDa). On the other hand, the high binding affinity of $AmBF_3$-$(AEBS)_3$ and $AmBF_3$-$(ABS)_3$ to CA-XII is advantageous as CA-XII is also found up-regulated in hypoxic tumours[216].

Table 4.2 Inhibition constants of ^{18}F-$AmBF_3$-sulfonamides to human CA isoenzymes I, II, IX and XII.

Compound	K_i (nM)			
	CA-I	**CA-II**	**CA-IX**	**CA-XII**
$AmBF_3$-AEBS	137	27.5	8.0	0.76
$AmBF_3$-ABS	65.6	59.8	6.6	0.49
$AmBF_3$-$(AEBS)_3$	34.8	26.5	35.7	8.6
$AmBF_3$-$(ABS)_3$	100.3	8.6	8.5	8.6
Acetazolamide	250	12	25	6.0

Errors in the range of ± 5% of the reported data from three different assays

We used the facile ^{18}F-^{19}F isotopic exchange reaction on $AmBF_3$-bioconjugates for the preparation of tracers (Figure 4.3)[202]. Features of this radiolabeling strategy include: one-step synthesis without azeotropic drying, good radiochemical yields, high purity, specific activity and

in vitro/vivo stability, and relative ease of purification without HPLC[202]. This approach for ^{18}F-labeling has been successfully applied to RGD and somatostatin analogs for cancer imaging[205, 212]. Starting with 23.3 – 38.5 GBq of ^{18}F-fluoride, ^{18}F-AmBF$_3$-AEBS, ^{18}F-AmBF$_3$-ABS, ^{18}F-AmBF$_3$-(AEBS)$_3$, and ^{18}F-AmBF$_3$-(ABS)$_3$ were obtained in 24.8 ± 2.2%, 26.4 ± 10.2%, 28.0 ± 3.5% and 26.9 ± 5.6% nondecay-corrected radiochemical yields (n = 3) with corresponding specific activities of 185 ± 22, 141 ± 11, 66 ± 9, and 49 ± 12 GBq/μmol, respectively. After C18 Sep-Pak purification, > 95% radiochemical purity was obtained for all tracers based on HPLC radio-chromatograms. These radiosynthesis data (radiochemical yield and specific activity) are comparable with those previously reported for other AmBF$_3$-conjugates[205, 212].

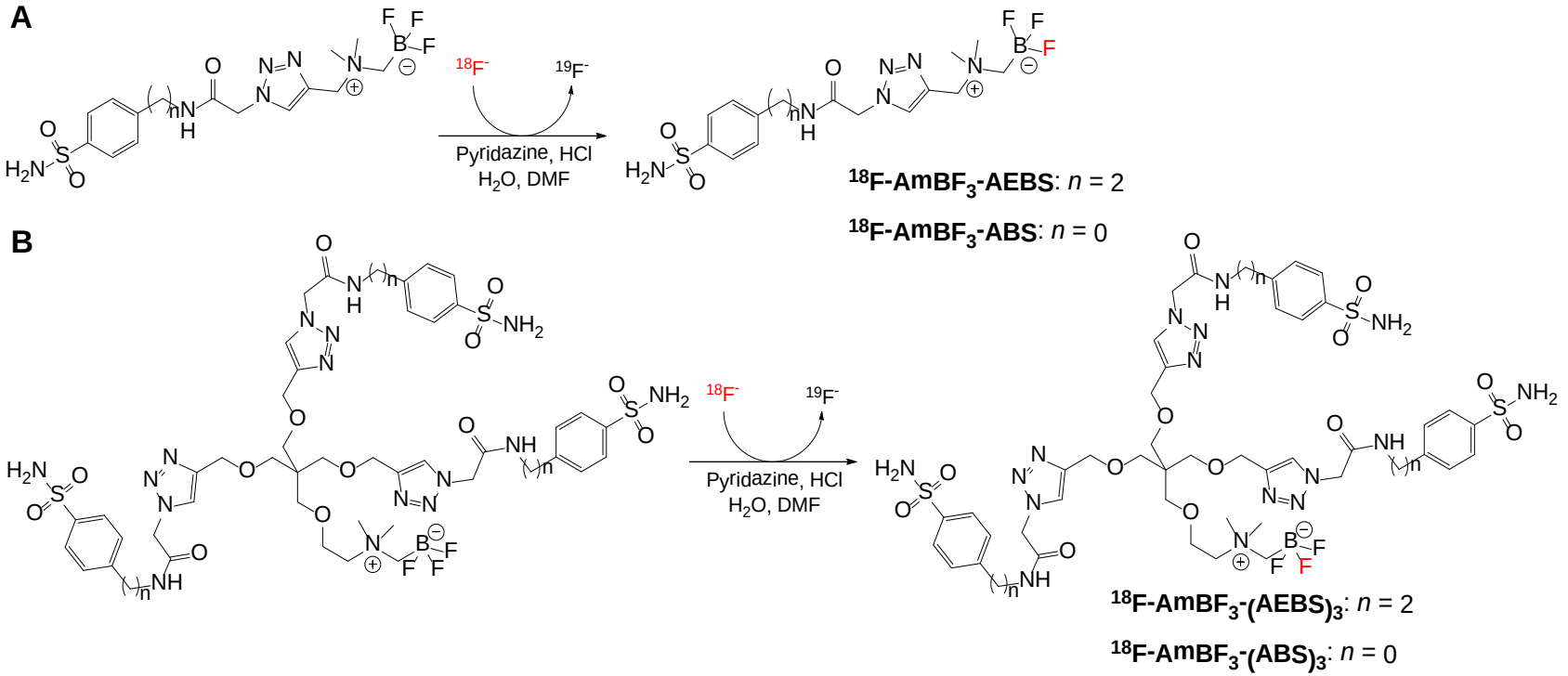

Figure 4.3 Radiosynthesis of (A) ^{18}F-AmBF$_3$-AEBS and ^{18}F-AmBF$_3$-ABS, and (B) ^{18}F-AmBF$_3$-(AEBS)$_3$ and ^{18}F-AmBF$_3$-(ABS)$_3$ via ^{18}F-^{19}F isotope exchange reaction.

To assess stability, tracers were incubated in mouse plasma and analyzed by HPLC. No metabolites of ^{18}F-AmBF$_3$-AEBS, ^{18}F-AmBF$_3$-ABS, ^{18}F-AmBF$_3$-(AEBS)$_3$, and ^{18}F-AmBF$_3$-(ABS)$_3$ were observed after 2 h incubation at 37 °C. Using shake flask extraction method, the LogD$_{7.4}$ values of ^{18}F-AmBF$_3$-AEBS, ^{18}F-AmBF$_3$-ABS, ^{18}F-AmBF$_3$-(AEBS)$_3$, and ^{18}F-AmBF$_3$-(ABS)$_3$ were measured to be -1.9, -1.8, -2.1 and -2.5, respectively.

For in vivo evaluations, studies were conducted with immunodeficient mice inoculated with HT-29 human colorectal cancer cells. HT-29 cells express high levels of CA-IX under hypoxic conditions[217]. Biodistribution (Table 4.3) showed that tracers cleared rapidly through the hepatobiliary and renal pathways. At 1 h p.i., ^{18}F-AmBF$_3$-AEBS and ^{18}F-AmBF$_3$-ABS had higher tumour accumulation (0.56 ± 0.11 and 0.64 ± 0.08 %ID/g) than their trimeric counterparts (0.30 ± 0.10 and 0.33 ± 0.07 %ID/g); however tumour-to-background ratios were substantially lower (Figure 4.4). Most importantly, tumour-to-blood ratios were 1.01 ± 0.25 and 1.24 ± 0.12 for ^{18}F-AmBF$_3$-AEBS and ^{18}F-AmBF$_3$-ABS, respectively, suggesting that both tracers may have bound intracellular CAs in blood. Although monomers may be more pertinent for traversing through aberrant tumour vasculature and binding to CA-IX, they appear to be unable to differentiate between CA isoforms. In regards to the trimers, ^{18}F-AmBF$_3$-(ABS)$_3$ demonstrated superior tumour-to-muscle (9.55 ± 2.96 *vs.* 4.94 ± 2.76) and tumour-to-blood (3.93 ± 1.26 *vs.* 2.88 ± 1.81) ratios. The difference may be explained by tracer lipophilicity. With three additional ethylene moieties, ^{18}F-AmBF$_3$-(AEBS)$_3$ proved more lipophilic and had a higher LogD$_{7.4}$ value compared to ^{18}F-AmBF$_3$-(ABS)$_3$. With the exception of testes, stomach, kidney and bone, uptake in nontarget tissues was higher for ^{18}F-AmBF$_3$-(AEBS)$_3$. Based on this observation, it appears that image contrast may be improved by selecting more hydrophilic CA-IX-targeting pharmacophores[218]. Since ^{18}F-AmBF$_3$-(ABS)$_3$ yielded the most promising results of the evaluated tracers, additional biodistribution studies were performed at 2 h p.i. to determine if tumour uptake and/or contrast would improve over time. Although tumour uptake for ^{18}F-AmBF$_3$-(ABS)$_3$ decreased slightly from 0.33 ± 0.07 %ID/g at 1 h p.i. to 0.24 ± 0.05 %ID/g at 2 h p.i., tumours were readily visualized in PET images. Pre-injection with 10 mg/kg of acetazolamide significantly reduced the uptake of ^{18}F-AmBF$_3$-(ABS)$_3$ in tumours to 0.06 ± 0.01 %ID/g, as well as its tumour-to-background ratios at 1 h p.i.

Table 4.3 Biodistribution and tumour-to-nontarget ratios for ^{18}F-AmBF$_3$ sulfonamides.

Organ	^{18}F-AmBF$_3$-AEBS	^{18}F-AmBF$_3$-ABS	^{18}F-AmBF$_3$-(AEBS)$_3$	^{18}F-AmBF$_3$-(ABS)$_3$			
	1 h p.i.	1 h p.i.	1 h p.i.	0.5 h p.i.	1 h p.i. Unblocked	1 h p.i. Blocked*	2 h p.i.
Blood	0.56 ± 0.05	0.51 ± 0.05	0.19 ± 0.20	0.26 ± 0.02	0.09 ± 0.05	0.17 ± 0.17	0.07 ± 0.01
Fat	0.08 ± 0.03	0.08 ± 0.03	0.04 ± 0.05	0.16 ± 0.08	0.02 ± 0.01	0.03 ± 0.04	0.02 ± 0.00
Testes	0.14 ± 0.05	0.23 ± 0.15	0.04 ± 0.05	0.20 ± 0.11	0.04 ± 0.01	0.03 ± 0.02	0.03 ± 0.00
Stomach	0.54 ± 0.39	2.32 ± 2.14	1.03 ± 0.27	4.66 ± 4.06	1.90 ± 1.62	0.26 ± 0.36	0.44 ± 0.26
Spleen	0.38 ± 0.03	0.54 ± 0.31	0.55 ± 0.73	0.68 ± 0.24	0.37 ± 0.34	0.19 ± 0.24	0.19 ± 0.05
Liver	10.87 ± 0.53	13.64 ± 2.49	0.98 ± 0.67	9.64 ± 3.66	0.97 ± 0.27	0.34 ± 0.18†	0.58 ± 0.19
Pancreas	0.59 ± 0.07	0.57 ± 0.18	0.07 ± 0.05	0.22 ± 0.10	0.07 ± 0.05	0.08 ± 0.11	0.05 ± 0.03
Adrenals	0.32 ± 0.10	0.54 ± 0.27	0.34 ± 0.50	0.97 ± 1.02	0.21 ± 0.15	0.08 ± 0.03	0.26 ± 0.14
Kidney	74.33 ± 19.64	52.70 ± 14.09	0.94 ± 0.32	18.63 ± 3.41	1.78 ± 0.49	0.14 ± 0.04†	5.86 ± 0.86
Lungs	0.90 ± 0.18	1.97 ± 0.11	0.48 ± 0.54	2.75 ± 0.52	0.41 ± 0.29	0.23 ± 0.14	0.24 ± 0.04
Heart	0.29 ± 0.04	0.27 ± 0.02	0.10 ± 0.07	0.32 ± 0.05	0.08 ± 0.04	0.04 ± 0.03	0.08 ± 0.04
Muscle	0.18 ± 0.05	0.32 ± 0.11	0.07 ± 0.03	0.26 ± 0.08	0.04 ± 0.02	0.03 ± 0.01	0.10 ± 0.05
Bone	2.05 ± 0.36	0.85 ± 0.11	0.18 ± 0.12	0.52 ± 0.09	0.21 ± 0.09	0.10 ± 0.04	0.34 ± 0.02
Brain	0.05 ± 0.02	0.04 ± 0.00	0.02 ± 0.02	0.09 ± 0.02	0.02 ± 0.01	0.01 ± 0.01	0.02 ± 0.01
Tumour	0.56 ± 0.11	0.64 ± 0.08	0.30 ± 0.10	0.70 ± 0.13	0.33 ± 0.07	0.06 ± 0.01†	0.24 ± 0.05
Tumour/liver	0.05 ± 0.01	0.05 ± 0.01	0.37 ± 0.14	0.07 ± 0.03	0.35 ± 0.07	0.19 ± 0.04†	0.42 ± 0.07
Tumour/blood	1.01 ± 0.25	1.24 ± 0.12	2.88 ± 1.81	2.74 ± 0.68	3.93 ± 1.26	1.08 ± 1.03†	3.53 ± 0.55
Tumour/muscle	3.18 ± 0.63	2.15 ± 0.66	4.94 ± 2.76	2.87 ± 1.43	9.55 ± 2.96	1.95 ± 0.52†	2.78 ± 1.44

*Blocked by pre-injection of 10 mg/kg of acetazolamide 1 h before administering radiotracer.
†Pre-injection significantly reduced uptake of the same organ/ratio ($p < 0.05$).
Values (%ID/g) are presented as mean ± SD ($n \geq 4$)

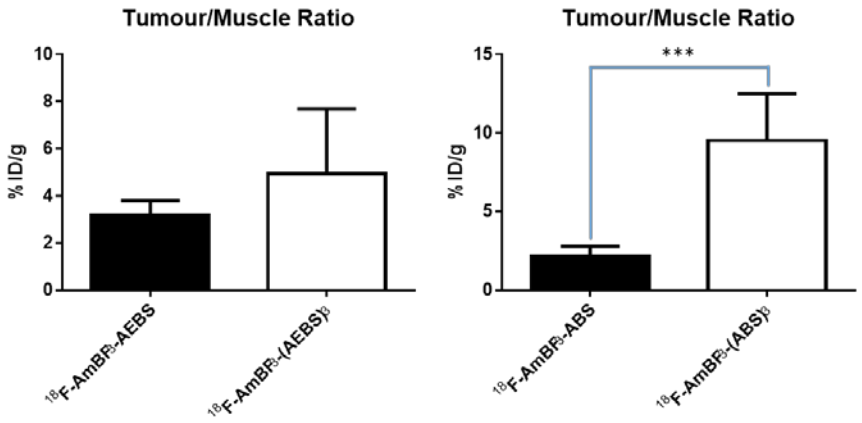

Figure 4.4 Tumour-to-muscle ratios for ^{18}F-AmBF$_3$ sulfonamides at 1 h p.i. Trimerization of ABS statistically significantly improved tumour-to-muscle contrast. ****p* <0.001

PET/CT images obtained at 1 h p.i. (Figure 4.5 and 4.6) were consistent with the biodistribution data. Higher uptake was observed in kidneys, liver, and gastrointestinal tract. HT-29 tumour xenografts were clearly visualized after injecting ^{18}F-AmBF$_3$-AEBS (Figure 4.5A), ^{18}F-AmBF$_3$-ABS (Figure 4.5B), ^{18}F-AmBF$_3$-(AEBS)$_3$ (Figure 4.6A), or ^{18}F-AmBF$_3$-(ABS)$_3$ (Figure 4.6B). Blocking studies were performed for ^{18}F-AmBF$_3$-(ABS)$_3$ that generated highest tumour-to-background contrast. Pre-injection of acetazolamide effectively blocked uptake of ^{18}F-AmBF$_3$-(ABS)$_3$ in tumour and reduced tumour-to-background contrast (Figure 4.6C)

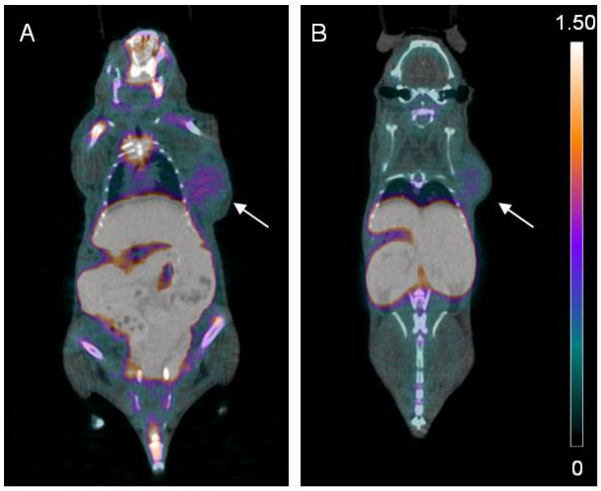

Figure 4.5 PET/CT images of monomeric ^{18}F-sulfonamides at 1 h p.i. (A) ^{18}F-AmBF$_3$-AEBS, and (B) ^{18}F-AmBF$_3$-ABS. Tumours are indicated by arrows. Scale bar unit is %ID/g.

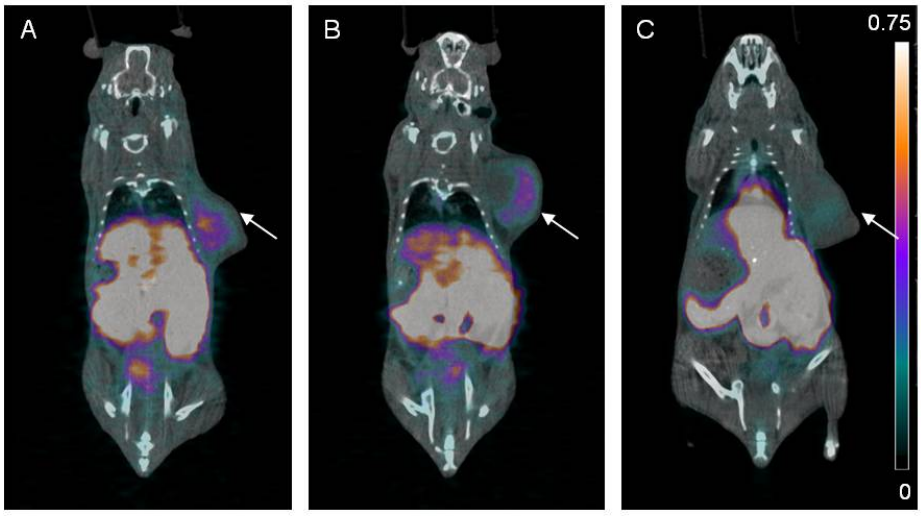

Figure 4.6 PET/CT images of trimeric ^{18}F-sulfonamides at 1 h p.i. (A) ^{18}F-AmBF$_3$-(AEBS)$_3$, (B) ^{18}F-AmBF$_3$-(ABS)$_3$, and (C) ^{18}F-AmBF$_3$-(ABS)$_3$ pre-blocking with acetazolamide. Tumours are indicated by arrows. Scale bar unit is %ID/g.

Given the prognostic and therapeutic value of CA-IX, the development of CA-IX imaging agents will have a significant clinical impact. Notwithstanding somewhat low tumour uptake, both ^{18}F-AmBF$_3$-(AEBS)$_3$ and ^{18}F-AmBF$_3$-(ABS)$_3$ enabled clear visualization of CA-IX expressing HT-29 tumour xenografts to provide some of the highest tumour-to-blood and tumour-to-muscle ratios ever reported. Pre-injection of acetazolamide significantly blocked tumour uptake to near background levels for ^{18}F-AmBF$_3$-(ABS)$_3$ demonstrating target specificity. These data represent a great advancement over previous attempts, and demonstrate the effectiveness of increasing cell-impermeability to achieve CA-IX selectivity. Further synthetic modifications to reduce gastrointestinal uptake as well as the use of more specific inhibitors to increase tumour uptake are ongoing. In the meantime, we suggest that this method has great potential to enhance in vivo imaging of extracellular enzymatic activity through the simple application of a multivalent approach that mitigates generalized uptake.

4.4 Conclusion

We synthesized and evaluated four ^{18}F-labeled sulfonamides as PET imaging agents targeting CA-IX. Trimerization of sulfonamide derivatives improved tumour-to-nontarget ratios, suggesting that a level of CA isoform selectivity was achieved in vivo. ^{18}F-AmBF$_3$-(ABS)$_3$

showed specific and selective uptake in CA-IX expressing tumour xenografts with good contrast. The use of multivalent enzyme inhibitors represents a viable strategy to selectively image extracellular enzyme activity with PET.

Chapter 5: Polyaminocarboxylate Conjugated Sulfonamides for ^{68}Ga-labeling and PET Imaging

5.1 Introduction

Carbonic anhydrases (CA) are a large family of zinc metalloenzymes that share a highly conserved protein domain for catalysis.[131] Whereas most CAs are found intracellularly (ex. CA-I and CA-II are expressed in high abundance in erythrocytes), CA-IX and CA-XII are the two isoforms that reside at the extracellular surface[6, 15]. Although CA-XII is also ectopically expressed by cancers in response to hypoxia, it has lower expression profile and catalytic activity than CA-IX[219]. Based on the spatial distribution of the various CA isoforms, small molecule inhibitors that are cell impermeable have enhanced selectivity for CA-IX. Different strategies to confer CA-IX selectivity include introducing bulk (fluorophores, albumin binders, glycosylation, multimeric design)[207-210, 220] net charge (pyridinio sulfonamides)[221, 222], and/or enhancing hydrophilicity (polyaminocarboxylate chelators)[223-225]. Rami *et al.* synthesized several series of aromatic sulfonamides conjugated to DTPA, DOTA, and TETA chelators for Cu^{2+} complexation, and proposed their application for PET imaging[223]. While these Cu^{2+} sulfonamide complexes retained binding affinity to CA-I/II (K_i: 54-81 nM), negligible amounts were detected in red blood cells after direct incubation for 3 h due to cell impermeability[223].

Adapted from: PET Imaging of Carbonic Anhydrase IX Expression of HT-29 Tumor Xenograft Mice with ^{68}Ga-Labeled Benzenesulfonamides. Mol Pharm, 2016;13(3): 1137-1146.

Joseph Lau[1*], Zhengxing Zhang[1*], Silvia Jenni[1], Hsiou-Ting Kuo[1], Zhibo Liu[2], Daniella Vullo[3], Claudiu T. Supuran[3], Kuo-Shyan Lin[1,4], Francois Benard[1,4]

[1] Department of Molecular Oncology, BC Cancer Research Centre, BC Cancer Agency, Vancouver, BC, Canada
[2] Department of Chemistry, University of British Columbia, Vancouver, BC, Canada
[3] Dipartimento Neurofarba and Laboratorio di Chimica Bioinorganica, Università degli Studi di Firenze, Florence, Italy
[4] Department of Radiology, University of British Columbia, Vancouver, BC, Canada

JL, ZZ, KSL, and FB designed the study. JL, ZZ, SJ, HTK , ZL, and DV were involved in the experiments. CTS provided the affinity measurements. JL and ZZ were involved in acquisition of data and interpretation of the analysis. JL and ZZ wrote the manuscript.

[*]Co-First Author

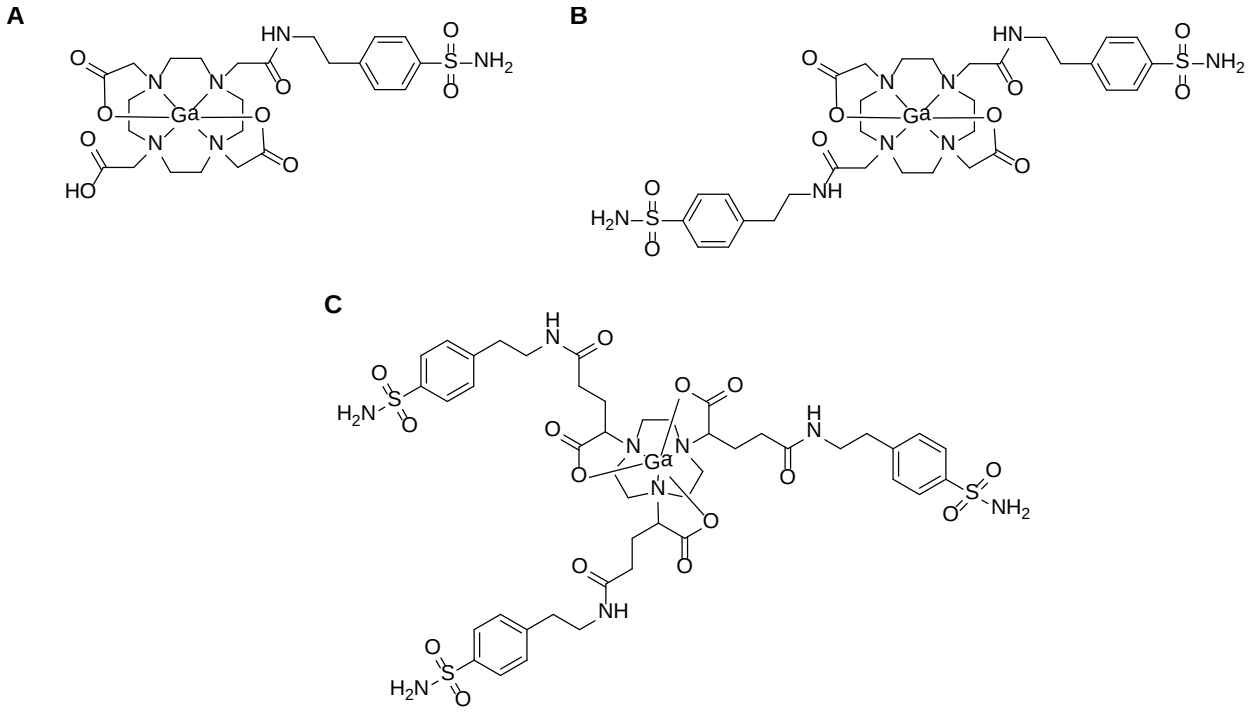

Figure 5.1 Chemical structures of ^{68}Ga-DOTA-AEBSA, ^{68}Ga-DOTA-(AEBSA)$_2$ and ^{68}Ga-NOTGA-(AEBSA)$_3$. Tracers were radiolabeled with ^{68}Ga for PET imaging.

For our study, we synthesized monomeric (DOTA-AEBSA), dimeric (DOTA-(AEBSA)$_2$) and trimeric (NOTGA(AEBSA)$_3$) sulfonamide inhibitors and radiolabeled them with ^{68}Ga (Figure 5.1). ^{68}Ga has a short radioactive half-life (67.7 min) that makes it suitable for labeling pharmaceuticals that have rapid targeting and clearance profiles[226]. As an imaging isotope, ^{68}Ga decays 89% via positron emission with an average 740 keV ($E^{+}_{\beta max}$ = 1.899 MeV) positron energy per disintegration[226]. ^{68}Ga-DOTA/NOTGA complexes are highly stable[227], and several ^{68}Ga-DOTA peptide derivatives have successfully entered the clinic setting for targeting somatostatin receptors in neuroendocrine tumours[228]. More significantly, as ^{68}Ga can be eluted from ^{68}Ge/^{68}Ga generators for on-demand synthesis, this allows facilities without access to a cyclotron to readily synthesize these tracers. We hypothesized that a multivalent approach may increase binding avidity to CA-IX, and cell impermeability can be achieved through the hydrophilicity and bulk of the metal/chelator complex.

5.2 Methods

5.2.1 Reagents and Instrumentation

All chemicals and solvents unless otherwise specified were obtained from commercial sources, and used without further purification. Tri-*tert*-butyl 1,4,7,10-tetraazacyclododecane-1,4,7,10-tetraacetate (**1**) was purchased from TCI America (Portland, OR). 1,7-Di-*tert*-butyl 1,4,7,10-tetraazacyclododecane-1,4,7,10-tetraacetate (**5**) and 1,4,7-triazacyclononane-1,4,7-tris-glutamic acid-α-*tert*-butyl ester-γ-succinimidyl ester (**9**) were synthesized according to literature methods[229, 230]. Proton NMR spectra were obtained using a Bruker (Billerica, MA) Avance 300 spectrometer, and were reported in parts per million downfield from the peak of internal tetramethylsilane. High resolution electrospray-ionization mass spectrometry (ESI-MS) was performed on a Waters Micromass LCT TOF instrument. Purification and quality control of ^{68}Ga-labeled CA-IX inhibitors were performed on an Agilent (Santa Clara, CA) HPLC system equipped with a model 1200 quaternary pump, a model 1200 UV absorbance detector (wavelength preset at 220 nm), and a Bioscan (Washington, DC) NaI scintillation detector. The HPLC columns used were a semipreparative column (Phenomenex C18, 5 µ, 250 × 10 mm) and an analytical column (Phenomenex Luna C18, 5 µ, 250 × 4.6 mm). The HPLC conditions used for the purification and quality control of cold and radiolabeled compounds are shown in Table 5.1. [^{68}Ga]$GaCl_3$ was eluted from either a 30-mCi ^{68}Ge/^{68}Ga generator from Eckert & Ziegler (Berlin, Germany) or a 50-mCi generator from iThemba LABS (Faure, South Africa). Radioactivity of ^{68}Ga-labeled tracers were measured using a Capintec (Ramsey, NJ) CRC®-25R/W dose calibrator.

Table 5.1 HPLC conditions used for purification, QC and plasma stability assays.

Compound	Column	Solvent system (containing 0.1% TFA)	Flow rate (mL/min)	Retention time (min)
3, 4	Phenomenex Luna C18, 5 µm, 10 × 250 mm semi-prep	5% CH_3CN in water	4.5	14.8, 16.5
7, 8	Phenomenex Luna C18, 5 µm, 10 × 250 mm semi-prep	0-30 min, 0 to 30% CH_3CN in water	4.5	20.0, 21.4
11, 12	Phenomenex Luna C18, 5 µm, 10 × 250 mm semi-prep	21% CH_3CN in water	4.5	16.5, 16.5
^{68}Ga-DOTA-AEBSA	Phenomenex Luna C18, 5 µm, 10 × 250 mm semi-prep	5% EtOH in PBS	4.5	10.0
^{68}Ga-DOTA-(AEBSA)$_2$	Phenomenex Luna C18, 5 µm, 10 × 250 mm semi-prep	7% EtOH in PBS	4.5	16.5
^{68}Ga-NOTGA-(AEBSA)$_3$	Phenomenex Luna C18, 5 µm, 10 × 250 mm semi-prep	20% CH_3CN in PBS	4.5	17.5
^{68}Ga-DOTA-AEBSA (QC and plasma stability)	Phenomenex Luna C18, 5 µm, 4.6 × 250 mm analytical	5% EtOH in PBS	2.0	4.3
^{68}Ga-DOTA-(AEBSA)$_2$ (QC and plasma stability)	Phenomenex Luna C18, 5 µm, 4.6 × 250 mm analytical	7% EtOH in PBS	2.0	6.7
^{68}Ga-NOTGA-(AEBSA)$_3$ (QC and plasma stability)	Phenomenex Luna C18, 5 µm, 4.6 × 250 mm analytical	19% CH_3CN in PBS	2.0	10.5

5.2.2 Chemistry and Radiolabeling

5.2.2.1 Synthesis of 1,4,7,10-tetraazacyclododecane-1,4,7-tris(*t*-butylacetate)-10-p-sulfonamidophenylethylacetamide (2)

A mixture of tri-*tert*-butyl 1,4,7,10-tetraazacyclododecane-1,4,7,10-tetraacetate **1** (100 mg, 0.18 mmol), 4-(2-aminoethyl)benzenesulfonamide (35 mg, 0.18 mmol), EDC•HCl (34 mg, 0.18 mol),

ethyldiisopropylamine (30 µL, 0.18 mmol), and HOBt(hydroxybenzotriazole)•H_2O (27 mg, 0.18 mmol) in DMF (5 mL) was stirred at room temperature for 24 h, and then the solvent was removed under reduced pressure. Ethyl acetate (50 mL) was added to the residue, and then the mixture was washed successively with 0.5 M NaOH (50 mL × 2), saturated aqueous $NaHCO_3$ solution (50 mL), and brine (50 mL). The organic layer was dried over magnesium sulfate before evaporation. The residue was obtained as a white powder and used for the next reaction without further purification. Yield: 71 mg (0.09 mmol, 52%). ^{1}H NMR (300 MHz, $CDCl_3$) δ 9.09 (s, 1H, CONH), 7.86 (d, J = 8.1 Hz, 2H, Ar–H), 7.48 (d, J = 8.1 Hz, 2H, Ar–H), 5.59 (s, 2H, NH_2), 3.78 – 3.28 (m, 6H, CH_2), 3.14 – 2.65 (m, 10H, CH_2), 2.31 – 1.92 (m, 12H, CH_2), 1.47 (s, 27H, CH_3); HRMS(ESI) Calcd. for $C_{36}H_{62}N_6O_9S$: m/z 755.4377 ($[M+H]^+$); Found: m/z 755.4373 ($[M+H]^+$).

5.2.2.2 Synthesis of 1,4,7,10-tetraazacyclododecane-1,4,7-triacetic acid, 10-p-sulfonamidophenylethylacetamide (DOTA-AEBSA, 3)

A solution of **2** (20 mg, 0.026 mmol) in 1:1 TFA/CH_2Cl_2 (2 mL) was stirred at room temperature overnight. Solvent was evaporated and CH_2Cl_2 (10 mL × 2) was added and subsequently removed under reduced pressure to remove excess TFA. The residue was dissolved in de-ionized water and purified by HPLC to yield **3·xTFA** as a white solid (17 mg). ^{1}H NMR (D_2O, 300 MHz) δ 7.86 (d, J = 8.0 Hz, 2H, Ar–H), 7.51 (d, J = 8.0 Hz, 2H, Ar–H), 4.11 – 3.65 (m, 6H, CH_2), 3.64 – 3.48 (m, 4H, CH_2), 3.42 – 3.00 (m, 14H, CH_2), 2.98 – 2.82 (m, 4H, CH_2); HRMS(ESI) Calcd. for $C_{24}H_{38}N_6O_9S$: m/z 587.2499 ($[M+H]^+$); Found: m/z 587.2507 ($[M+H]^+$).

5.2.2.3 Synthesis of 1,4,7,10-tetraazacyclododecane-1,4-bis(*t*-butylacetate)-7,10-bis-p-sulfonamidophenylethylacetamide (6)

A mixture of 1,7-di-*tert*-butyl 1,4,7,10-tetraazacyclododecane-1,4,7,10-tetraacetate **5** (150 mg, 0.29 mmol), 4-(2-aminoethyl)benzenesulfonamide (116 mg, 0.58 mmol), EDC•HCl (111 mg, 0.58 mol), ethyldiisopropylamine (101 µL, 0.58 mmol), and HOBt•H_2O (89 mg, 0.58 mmol) in DMF (5 mL) was stirred at room temperature for 24 h, and solvent was removed under reduced pressure. Ethyl acetate (50 mL) was added to the residue, and then the mixture was washed successively with 0.5 M NaOH (50 mL × 2), saturated aqueous $NaHCO_3$ solution (50 mL), and

brine (50 mL). The organic layer was dried over magnesium sulfate before evaporation. The residue was obtained as a white powder and used for next reaction without further purification. Yield: 57 mg (0.06 mmol, 22%). ^{1}H NMR (300 MHz, d_6-DMSO) δ 8.27 (s, 2H, CONH), 7.82 – 7.67 (m, 4H, Ar–H), 7.47 – 7.35 (m, 4H, Ar–H), 5.80 (s, 4H, NH_2), 3.27 – 3.10 (m, 6H, CH_2), 3.05 – 2.90 (m, 6H, CH_2), 2.87 – 2.75 (m, 6H, CH_2), 2.72 – 2.57 (m, 6H, CH_2), 2.30 – 1.94 (m, 8H, CH_2), 1.41 (s, 18H, CH_3); HRMS(ESI) Calcd. for $C_{40}H_{64}N_8O_{10}S_2$: m/z 881.4265 ($[M+H]^+$); Found: m/z 881.4277 ($[M+H]^+$).

5.2.2.4 Synthesis of 1,4,7,10-tetraazacyclododecane-1,7-diacetic acid, 4,10-bis-p-sulfonamidophenylethylacetamide (DOTA-(AEBSA)$_2$, 7)

A solution of **6** (50 mg, 0.06 mmol) in 1:1 TFA/CH_2Cl_2 (2 mL) was stirred at room temperature overnight. Solvent was evaporated and CH_2Cl_2 (10 mL × 2) was added and then removed under reduced pressure to remove excess TFA. The residue was dissolved in de-ionized water and purified by HPLC to give **7·xTFA** as a white solid (26 mg). ^{1}H NMR (D_2O, 300 MHz) δ 7.81 (d, J = 8.0 Hz, 4H, Ar–H), 7.44 (d, J = 8.0 Hz, 4H, Ar–H), 3.90 – 3.59 (m, 4H, CH_2), 3.59 – 3.33 (m, 8H, CH_2), 3.33 – 2.98 (m, 12H, CH_2), 2.96 – 2.74 (m, 8H, CH_2); HRMS(ESI) Calcd. for $C_{32}H_{48}N_8O_{10}S_2$: m/z 769.3013 ($[M+H]^+$); Found: m/z 769.3028 ($[M+H]^+$).

5.2.2.5 Synthesis of 1,4,7-triazacyclononane-1,4,7-tris-glutamic acid-α-*tert*-butyl ester-γ-p-sulfonamidophenylethylamide (10)

A mixture of 1,4,7-triazacyclononane-1,4,7-tris-glutamic acid-α-*tert*-butyl ester-γ-succinimidyl ester **9** (680 mg, 0.70 mmol), 4-(2-aminoethyl)benzenesulfonamide (459 mg, 2.29 mmol) and ethyldiisopropylamine (399 µL, 2.29 mmol) in DMF (50 mL) was initially stirred at room temperature for 24 h before incubation at 50^{o}C for an additional 24 h. Excess solvent was removed under reduced pressure. Water (100 mL) was added and the resultant mixture was extracted with $CHCl_3$ (100 mL × 3). The combined organic phase was dried over magnesium sulfate before evaporation. Residue was loaded onto a silica gel column and eluted using a mixture of EtOAc/methanol (10:1 to 5:1). The product was obtained as a white foam. Yield: 283 mg (0.23 mmol, 33%). ^{1}H NMR (300 MHz, d_6-DMSO) δ 7.95 (s, 3H, CONH), 7.73 (d, J = 8.2

Hz, 6H, Ar–H), 7.37 (d, J = 8.2 Hz, 6H, Ar–H), 7.28 (s, 6H, NH_2), 3.14 – 3.00 (m, 4H, CH_2), 2.85 – 2.75 (m, 10H, CH_2), 2.69 – 2.55 (m, 6H, CH_2), 2.25 – 2.05 (m, 7H, CH_2), 1.83 – 1.55 (m, 12H, CH_2), 1.40 (s, 27H, CH_3); HRMS(ESI) Calcd. for $C_{57}H_{87}N_9O_{15}S_3$: m/z 1234.5562 ($[M+H]^+$); Found: m/z 1234.5559 ($[M+H]^+$).

5.2.2.6 Synthesis of 1,4,7-triazacyclononane-1,4,7-tris-glutamic acid-γ-p-sulfonamidophenylethylamide (NOTGA-(AEBSA)$_3$, 11)

A solution of **10** (100 mg, 0.081 mmol) in 1:1 TFA/CH_2Cl_2 (2 mL) was stirred at room temperature overnight. The solvent was evaporated and CH_2Cl_2 (10 mL × 2) was added and then removed under reduced pressure to remove excess TFA. The residue was dissolved in de-ionized water and purified by HPLC to yield **11·xTFA** as a white solid (70 mg). ^{1}H NMR (300 MHz, DMSO) δ 8.08 (s, 3H, CONH), 7.74 (d, J = 8.1 Hz, 6H, Ar–H), 7.37 (d, J = 8.1 Hz, 6H, Ar–H), 7.30 (s, 6H, NH_2), 3.37 – 3.14 (m, 11H, CH_2), 3.13 – 2.87 (m, 9H, CH_2), 2.84 – 2.70 (m, 7H, CH_2), 2.37 – 2.18 (m, 6H, CH_2), 2.06 – 1.88 (m, 6H, CH_2); HRMS(ESI) Calcd. for $C_{45}H_{63}N_9O_{15}S_3$: m/z 1065.3684 ($[M+H]^+$); Found: m/z 1066.3666 ($[M+H]^+$).

5.2.2.7 General Procedure for the Synthesis of Cold Gallium Standard

A solution of the corresponding precursor in sodium acetate buffer (0.5 mL, 0.1 M, pH = 4.0) and 5 equiv. of $^{nat}GaCl_3$ was stirred at 80 ^oC for 15 min. The mixture was purified by HPLC to give the corresponding gallium complexes as a white fluffy solid.

^{nat}Ga-DOTA-AEBSA (**4**) Yield: 69%. ^{1}H NMR (D_2O, 300 MHz) δ 7.95 (d, J = 8.2 Hz, 2H, Ar–H), 7.60 (d, J = 8.2 Hz, 2H, Ar–H), 4.21 – 3.85 (m, 8H, CH_2), 3.78 – 3.32 (m, 16H, CH_2), 3.14 – 2.92 (m, 4H, CH_2); HRMS(ESI) Calcd. for $C_{24}H_{35}GaN_6O_9S$: m/z 653.1520 ($[M+H]^+$); Found: m/z 653.1516 ($[M+H]^+$).

^{nat}Ga-DOTA-(AEBSA)$_2$ (**8**) Yield: 61%. ^{1}H NMR (300 MHz, D_2O) δ 7.94 (d, J = 8.2 Hz, 4H, Ar–H), 7.59 (d, J = 8.0 Hz, 4H, Ar–H), 4.06 – 3.88 (m, 4H, CH_2), 3.79 – 3.50 (m, 16H, CH_2),

3.48 – 3.23 (m, 4H, CH_2), 3.17 – 2.91 (m, 8H, CH_2); HRMS(ESI) Calcd. for $C_{32}H_{46}GaN_8O_{10}S_2$: m/z 835.2034 ($[M]^+$); Found: m/z 835.2039 ($[M]^+$).

^{nat}Ga-NOTGA-(AEBSA)$_3$ (**12**) Yield: 72%. ^{1}H NMR (300 MHz, DMSO) δ 8.02 (s, 3H, CONH), 7.74 (d, J = 8.2 Hz, 6H, Ar–H), 7.40 (d, J = 8.2 Hz, 6H, Ar–H), 7.29 (s, 6H, NH_2), 3.30 – 3.19 (m, 10H, CH_2), 3.17 – 2.90 (m, 10H, CH_2), 2.90 – 2.67 (m, 10H, CH_2), 2.41 – 2.26 (m, 3H, CH_2), 2.18 – 1.98 (m, 3H, CH_2), 1.95 – 1.77 (m, 3H, CH_2); HRMS(ESI) Calcd. for $C_{45}H_{60}GaN_9O_{15}S_3$: m/z 1130.2549 ($[M-H]^-$); Found: m/z 1130.2570 ($[M-H]^-$).

5.2.2.8 General Procedure for the Synthesis of ^{68}Ga Tracers

$^{68}GaCl_3$ was purified following published procedures[231]. A HEPES buffer (0.50 mL, 2 M, pH = 5.0) solution of the corresponding precursor (30 μg for ^{68}Ga-DOTA-AEBSA, and 40 μg for ^{68}Ga-DOTA-(AEBSA)$_2$ and ^{68}Ga-NOTGA-(AEBSA)$_3$) and purified $^{68}GaCl_3$ (0.19-1.30 GBq for ^{68}Ga-DOTA-AEBSA, 0.19-1.41 GBq for ^{68}Ga-DOTA-(AEBSA)$_2$, and 0.19-0.70 GBq for ^{68}Ga-NOTGA-(AEBSA)$_3$) was heated in the microwave for 1 min. Reaction mixtures were purified by HPLC. ^{68}Ga-DOTA-AEBSA and ^{68}Ga-DOTA-(AEBSA)$_2$ were collected in fractions and used directly for in vitro and in vivo studies. ^{68}Ga-NOTGA-(AEBSA)$_3$ was collected, diluted with water, and loaded onto a C18 Sep-Pak cartridge to remove acetonitrile. The trapped ^{68}Ga-NOTGA-(AEBSA)$_3$ was eluted off the cartridge with ethanol and diluted with saline for in vitro and in vivo studies.

5.2.3 Binding Affinity Measurement

Inhibition constants (K_i) of $AmBF_3$-AEBS, $AmBF_3$-ABS, and $AmBF_3$-$(AEBS)_3$ and $AmBF_3$-$(ABS)_3$ for CA-I, -II, -IX and -XII were determined using the CA catalyzed CO_2 hydration stopped-flow assays following published procedures[178].

5.2.4 Stability in Mouse Plasma

Following published procedures, 100 μL aliquots of tracer were incubated with 400 μL of BALB/c mouse plasma (Innovative Research) for 2 h at 37 °C[231]. After incubation, sample was

quenched with 70% CH_3CN, passed through a 0.45 μm filter, and loaded on to a radio-HPLC system for analysis.

5.2.5 Lipophilicity Measurement

Values of octanol:water distribution coefficient at pH 7.4 ($LogD_{7.4}$) were determined for the radiotracers using a shake flask method as previously described[231]. Aliquots (2 μL) of the ^{68}Ga-labeled tracers were added to 15 mL conical centrifuge tubes containing 3 mL of octanol and 3 mL of phosphate buffer (0.1 M, pH 7.4). The mixture was vortexed for 1 min and centrifuged at 5,000 rpm for 10 min. Samples of the octanol (1 mL) and aqueous (1 mL) phases were taken and counted on a gamma counter. $LogD_{7.4}$ was calculated using the following equation: $LogD_{7.4} = Log_{10}$[(counts in octanol phase)/(counts in buffer phase)].

5.2.6 Cell Line

HT-29 human colorectal cancer cells were obtained as a gift from Dr. Donald Yapp (BC Cancer Research Centre, Vancouver, Canada). Cells were cultured in Dulbecco's Modified Eagle's Medium supplemented with 10% fetal bovine serum, 100 U/mL penicillin-streptomycin, and non-essential amino acids. Cells were incubated at 37 °C in an atmosphere containing 5% CO_2 and used for in vitro or in vivo experiments when 80-90% confluence was reached.

5.2.7 Immunofluorescence of HT-29 Colonies

This study was performed following published procedures[232]. Matrigel (52 μL) was added to individual wells of an 8-well chamber slide and allowed to solidify at 37 °C for 30 min. Cells (~ 1000) cultured in media + 2% matrigel in 300 μL were seeded per well. Cultures were incubated at 37 °C in an atmosphere containing 5% CO_2 for 21 days before fixation for immunocytochemistry. Growth medium was refreshed every four days with media + 2% matrigel. For immunofluorescence, colonies were fixed with 2% paraformaldehyde for 25 min at room temperature and permeabilized with PBS + 0.5% Triton-X for 10 min at 4 °C. After three rinses with PBS + 0.1 M glycine for 10 min, samples were rinsed once for 5 min with IF buffer (130 mM NaCl, 7 mM Na_2HPO_4, 3.5 mM NaH_2PO_4, 7.7 mM NaN_3, 0.1% bovine serum

albumin, 0.2% Triton X-100, 0.05% Tween-20) and blocked for 2.5 h in IF buffer containing 10% serum. CA-IX was stained with phycoerythrin-conjugated mouse-anti CA-IX antibody (R&D Systems) at 4 °C overnight. Cells were counterstained with Oregon Green 488 phalloidin (Invitrogen) for 20 min and Draq5 (Biostatus Limited) for 5 min. Imaging was performed on a Nikon Eclipse C1 confocal laser scanning microscope (Melville, NY) equipped with 488 nm, 561 nm, and 638 nm lasers.

5.2.8 PET Imaging and Biodistribution Studies

All animal studies were performed in accordance with the Canadian Council on Animal Care guidelines and approved by the Animal Care Committee of the University of British Columbia. Male immunodeficient NOD.Cg-*Prkdc*^{scid}*Il2rg*^{tm1Wjl}/SzJ (NSG) mice bred in-house at the Animal Research Centre, BC Cancer Research Centre were used for this study. Under anesthesia with 2.5% isoflurane in 2.0 L/min of oxygen, mice were subcutaneously inoculated with 5×10^6 HT-29 cells (in 100 µL PBS and BD Matrigel Matrix at 1:1 ratio) under the right dorsal flank. Biodistribution studies and PET/CT imaging were performed when tumours reached 7-9 mm in diameter.

PET imaging studies of ^{68}Ga-labeled tracers were conducted using a Siemens Inveon microPET/CT scanner. Under 2.5% isoflurane anesthesia in oxygen at 2.0 L/min, 3.7-7.4 MBq of ^{68}Ga-DOTA-AEBSA, ^{68}Ga-DOTA-$(AEBSA)_2$ or ^{68}Ga-NOTGA-$(AEBSA)_3$ in a volume of 200 µL was administered intravenously through the caudal vein. For blocking experiments, mice were intravenously pre-injected with 10 or 20 mg/kg acetazolamide 1 h (100 – 200 µL in saline, i.v.) before administering the radiotracer. At 1 h post-injection (p.i.), a 10 min PET scan was performed. For anatomical localization, a 10 min CT scan was performed prior to each PET acquisition. The body temperature of mice was maintained at 37 °C with the use of thermal pads. PET data were acquired in list mode acquisition, reconstructed using the 3d-OSEM-MAP algorithm with CT-based attenuation correction. Three-dimensional regions of interests (ROIs) were placed on the reconstructed images to determine the %ID/g of tissue using the Inveon Acquisition Workplace software (conversion factor was predetermined using a ^{68}Ge/^{68}Ga source).

Biodistribution studies were performed to confirm the quantitative ROI uptake values observed from PET scans. At 1 h p.i., mice were euthanized by cervical dislocation. Tissues of interest (blood, testes, stomach, intestine, spleen, liver, pancreas, kidney, lung, heart, tumour, muscle, bone and brain) were collected. Tissues were rinsed with PBS (except blood), blotted dry, weighed, and measured on a Packard Cobra II 5000 Series auto-gamma counter.

5.2.9 Statistical Analysis

All statistics were performed using Prism 6 software (GraphPad). For Figure 5.6, *P* values for the differences between tumour/muscle ratio, kidney and liver uptake were calculated using a two-way ANOVA test adjusted for multiple comparisons using the Holm-Šídák method. Values < 0.05 were considered statistically significant. For Table 5.4, *P* values for the difference of tracer uptake in mouse tissues between unblocked and blocked groups were calculated using a two-tailed *t*-test adjusted for multiple comparisons using the Holm-Šídák method. Values < 0.05 were considered statistically significant.

5.3 Results and Discussion

The synthesis scheme for the precursors and standards are shown in Figure 5.2. One to three 4-(2-aminoethyl)benzenesulfonamide (AEBSA) moieties were conjugated to either DOTA (monomer and dimer) or NOTGA (trimer) chelators to obtain the radiolabeling precursors. Results of the radiolabeling experiments are summarized in Table 5.2. All three tracers were successfully radiolabeled with ^{68}Ga with average decay-corrected isolated yields of ≥ 64% (n ≥ 3). The specific activities measured were 536.5 ± 187.1, 269.5 ± 176.9, and 50.9 ± 8.4 GBq/μmol for ^{68}Ga-DOTA-AEBSA, ^{68}Ga-DOTA-$(AEBSA)_2$, and ^{68}Ga-NOTGA-$(AEBSA)_3$ respectively. After purification by radio-HPLC, tracers were obtained in ≥ 97.5% average radiochemical purity for in vitro and in vivo experiments.

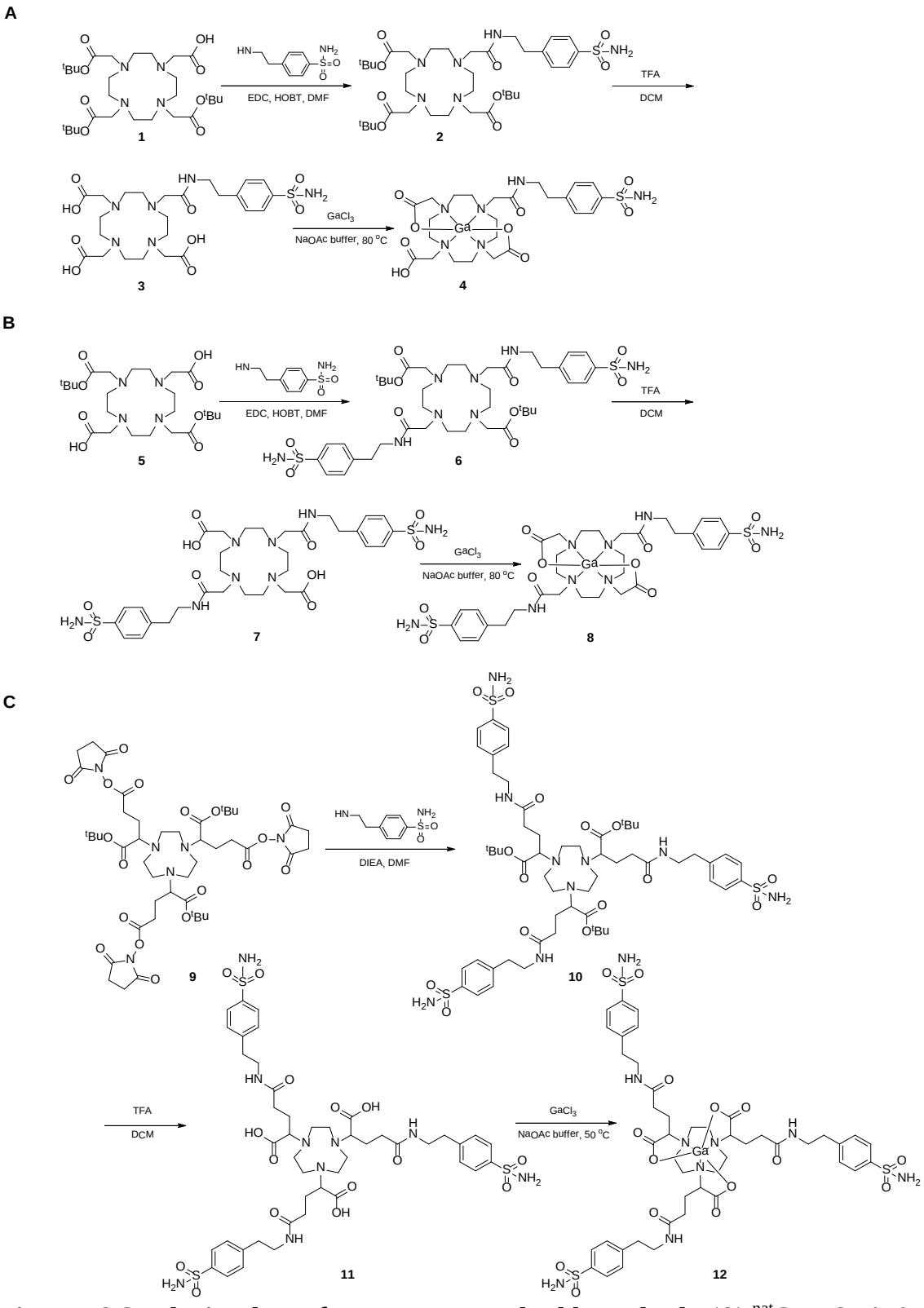

Figure 5.2 Synthetic scheme for precursors and cold standards. (A) ^{nat}Ga-DOTA-AEBSA; **(B)** ^{nat}Ga-DOTA-(AEBSA)$_2$ and **(C)** ^{nat}Ga-NOTGA-(AEBSA)

Table 5.2 Molecular weight and radiolabeling data of ^{68}Ga CA-IX inhibitors.

Compound	Molecular weight (Dalton)	% Isolated radiochemical yield[a]	% Radiochemical purity	Specific activity (GBq/μmol)
^{68}Ga-DOTA-AEBSA	653.36	91 ± 3	97.5 ± 1.9	536.5 ± 187.1
^{68}Ga-DOTA-$(AEBSA)_2$	835.6	84 ± 4	97.8 ± 1.8	269.5 ± 176.9
^{68}Ga-NOTGA-$(AEBSA)_3$	1132.93	64 ± 8	99.3 ± 0.3	50.9 ± 8.4

Data are presented as mean values ± standard deviation (n ≥ 3).
[a]Decay-corrected.

The stability of the tracers was assessed by incubating the tracers in mouse plasma. Tracers were highly stable in plasma, as > 90% of them remained intact after 2 h incubation at 37 °C (Figure 5.3). The $LogD_{7.4}$ values of ^{68}Ga-DOTA-AEBSA, ^{68}Ga-DOTA-$(AEBSA)_2$, and ^{68}Ga-NOTGA-$(AEBSA)_3$ were measured to be -4.37 ± 0.08, -3.52 ± 0.01, and -2.39 ± 0.01, respectively.

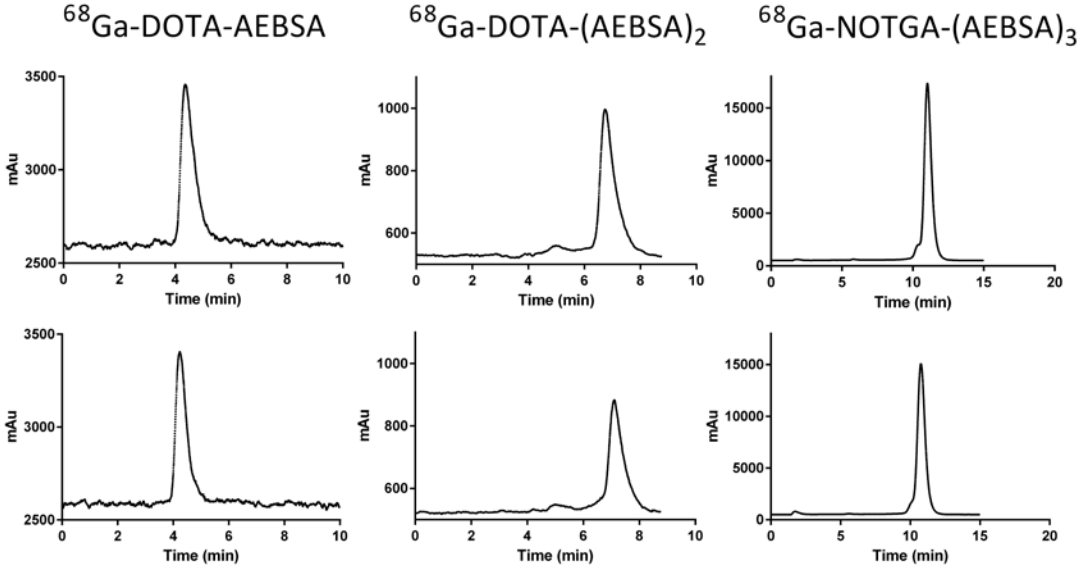

Figure 5.3 Stability of ^{68}Ga CA-IX inhibitors in mouse plasma. HPLC traces of ^{68}Ga CA-IX inhibitors before (top) and after 2 h incubation in mouse plasma (bottom). The Y-axis denotes radioactivity while the X-axis denotes retention time.

Table 5.3 Binding affinity (K_i) of sulfonamide inhibitors to CA-I, CA-II, CA-IX and CA-XII were determined via a stopped-flow CO_2 hydration assay.

Compound	Binding affinity (K_i, nM)			
	CA-I	**CA-II**	**CA-IX**	**CA-XII**
Ga-DOTA-AEBSA	38.0	136.8	10.8	30.7
Ga-DOTA-$(AEBSA)_2$	37.6	41.2	25.4	7.4
Ga-NOTGA-$(AEBSA)_3$	34.4	7.2	7.7	6.5
Acetazolamide	250	12.0	25.0	6.0

Errors in the range of 5-10% of the reported value from three different assays.

Sulfonamide derivatives inhibit CA-IX enzymatic activity by forming coordination with Zn^{2+} ion of the catalytic domain and displacing H_2O[131]. The primary concern with incorporating a multidentate chelator into our structural design was the possibility of steric hindrance. To ensure that our compounds can bind to CA-IX after coupling to either DOTA (monomer and dimer) or NOTGA (trimer), we first evaluated their binding affinity (K_i) using a CA catalyzed CO_2 stopped-flow hydration assay (Table 5.3). The K_i value of ^{68}Ga-DOTA-$(AEBSA)_2$ was similar to acetazolamide (25.4 nM vs 25.0 nM), while ^{68}Ga-DOTA-AEBSA and ^{68}Ga-NOTGA-$(AEBSA)_3$ exhibited 2-3 folds better binding affinity than acetazolamide (10.8 nM and 7.7 nM, respectively). For this study, the conjugation of sulfonamide moieties to polyaminocarboxylate chelators did not hinder CA-IX binding and inhibition.

The HT-29 xenograft model has been used extensively for evaluating prospective CA-IX radiotracers, and we have confirmed expression of CA-IX with immunofluorescence (Figure 5.4) and immunohistochemistry. Representative decay-corrected PET images of HT-29 tumour-bearing mice at 1 h p.i. are shown in Figure 5.5. ^{68}Ga-labeled sulfonamides generated good-contrast PET images in CA-IX expressing tumour xenografts. Absolute uptake appeared to correlate positively with the number of targeting moieties as well as molecular weight of the tracers. In addition to tumour, uptake was observed in excretory organs like the kidneys (^{68}Ga-DOTA-AEBSA, ^{68}Ga-DOTA-$(AEBSA)_2$, and ^{68}Ga-NOTGA-$(AEBSA)_3$) or liver (mostly for ^{68}Ga-DOTA-$(AEBSA)_2$, and ^{68}Ga-NOTGA-$(AEBSA)_3$). While ^{68}Ga-DOTA-AEBSA was excreted predominantly through the kidneys, ^{68}Ga-DOTA-$(AEBSA)_2$ and ^{68}Ga-NOTGA-$(AEBSA)_3$ were cleared by both renal and hepatobiliary pathways. The differences in pharmacokinetic profile between the tracers may be attributed to tracer lipophilicity. The

incorporation of each additional benzenesulfonamide moiety increased overall lipophilicity. As ^{68}Ga-DOTA-AEBSA generated the highest contrasted images, blocking studies were performed by pre-injecting acetazolamide (10 and 20 mg/kg, intravenous) before tracer administration. Uptake in HT-29 tumours was successfully blocked compared to baseline studies indicating tracer specificity (Table 5.4).

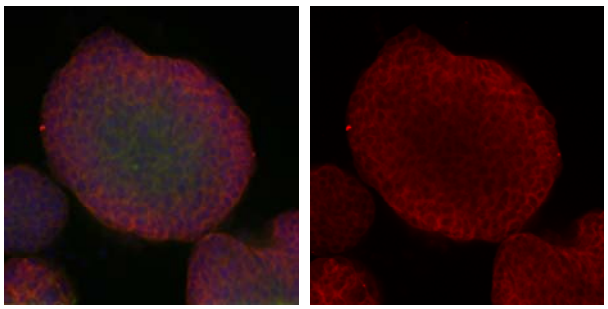

Figure 5.4 CA-IX expression in HT-29 colorectal cancer model. CA-IX expression in cell model was confirmed in vitro and with 3D colony immunofluorescence (red = CA-IX, blue = nucleus and green = F-actin). Left: Merged. Right: CA-IX alone.

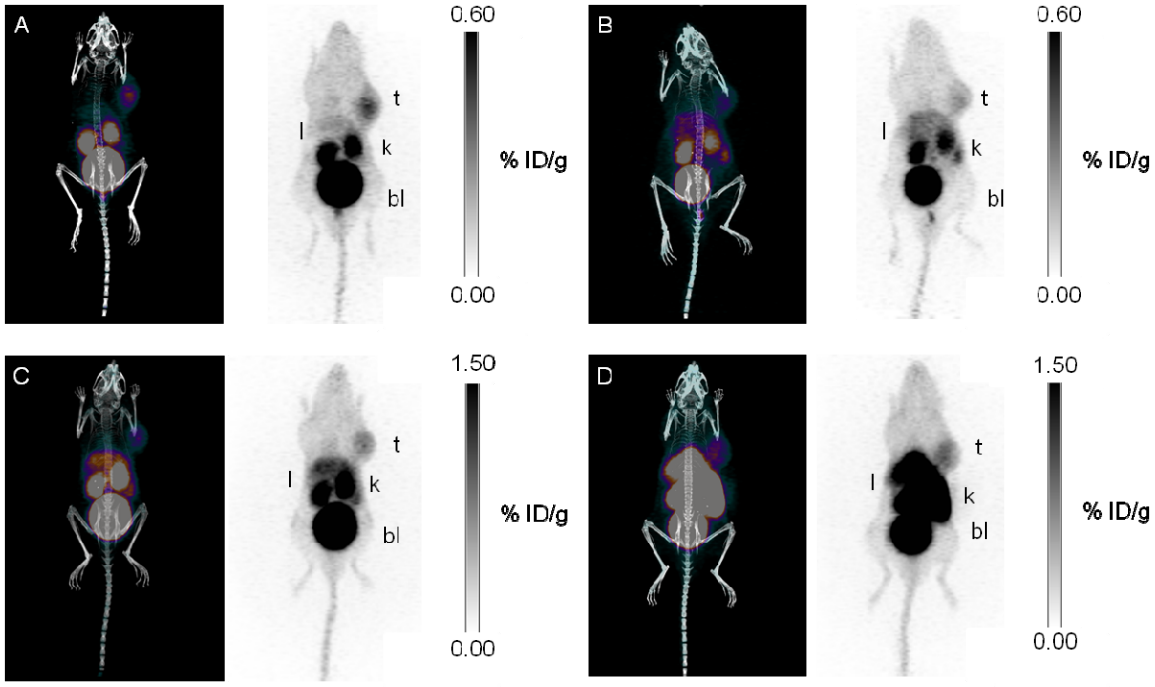

Figure 5.5 Maximal intensity projections of PET/CT and PET with ^{68}Ga tracers at 1 h p.i. **(A)** ^{68}Ga-DOTA-AEBSA; **(B)** ^{68}Ga-DOTA-AEBSA pre-blocked with 10 mg/kg of acetazolamide; **(C)** ^{68}Ga-DOTA-(AEBSA)$_2$; and **(D)** ^{68}Ga-NOTGA-(AEBSA)$_3$. t = tumour; l = liver; k = kidney; bl = bladder

Biodistribution analysis corroborated observations of the PET images (Table 5.4). Tumour uptake of ^{68}Ga-DOTA-AEBSA, ^{68}Ga-DOTA-(AEBSA)$_2$, and ^{68}Ga-NOTGA-(AEBSA)$_3$ were 0.81 ± 0.15, 1.93 ± 0.26, and 2.30 ± 0.53 %ID/g at 1 h p.i. Although not statistically significant, ^{68}Ga-DOTA-AEBSA managed to generate the highest tumour-to-muscle contrast at 5.02 ± 0.22 when compared to ^{68}Ga-DOTA-(AEBSA)$_2$ (4.07 ± 0.87) and ^{68}Ga-NOTGA-(AEBSA)$_3$ (4.18 ± 0.84) (Figure 5.6). For ^{68}Ga-DOTA-AEBSA, minimal uptake was noted in non-target tissue with kidneys being the only organ with higher uptake (4.37 ± 1.04 %ID/g) than tumour at 1 h p.i. For ^{68}Ga-DOTA-(AEBSA)$_2$ and ^{68}Ga-NOTGA-(AEBSA)$_3$, enhanced tumour uptake is accompanied by an increase of radioactivity in kidneys (14.84 ± 7.21 and 14.40 ± 1.65) and in liver (3.78 ± 1.06 and 8.01 ± 3.58). Uptake in latter indicated the involvement of the hepatobiliary pathway in the excretion profiles of both the dimer and trimer. Pre-injection with 10 mg/kg of acetazolamide significantly reduced the uptake of ^{68}Ga-DOTA-AEBSA in tumours to 0.41 ± 0.10 %ID/g. Injection of a higher dose of acetazolamide (20 mg/kg) led to further reduction in non-target tissues, but similar reduction in tumour uptake (0.35 ± 0.17 %ID/g) relative to the 10 mg/kg dose. It is possible that the activity reduction observed in kidneys and liver is due to the indirect effect of acetazolamide as a diuretic[233].

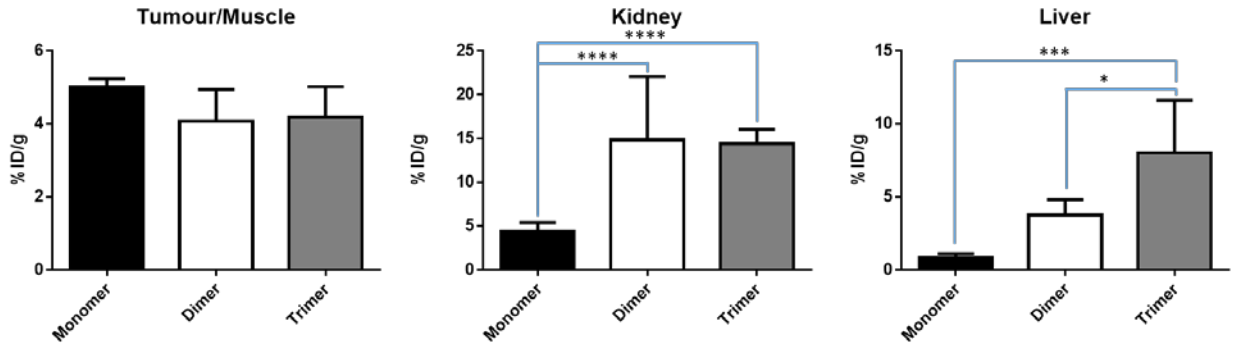

Figure 5.6 Two-way ANOVA analysis of tumour/muscle ratio, kidney and liver uptake for ^{68}Ga CA-IX inhibitors. There are no statistically significant differences for tumour/muscle ratio. In contrast, there are statistically significant differences for both renal and hepatobiliary uptake for the tracers. *p <0.05, **p <0.01, ***p <0.001, ****p <0.0001

Table 5.4 Biodistribution and tumour-to-nontarget ratios for ^{68}Ga CA-IX inhibitors

Organ	**^{68}Ga-DOTA-AEBSA**			**^{68}Ga-DOTA-$(AEBSA)_2$**	**^{68}Ga-NOTGA-$(AEBSA)_3$**
	Unblocked (n = 5)	**10 mg/kg AZA[a]** (n = 5)	**20 mg/kg AZA[a]** (n = 4)	**Unblocked** (n = 5)	**Unblocked** (n = 5)
Blood	0.63 ± 0.15	0.33 ± 0.13	0.25 ± 0.08[b]	1.53 ± 0.25	0.92 ± 0.35
Fat	0.09 ± 0.04	0.08 ± 0.07	0.04 ± 0.01	0.24 ± 0.13	0.21 ± 0.14
Testes	0.16 ± 0.05	0.10 ± 0.05	0.06 ± 0.02	0.41 ± 0.06	0.37 ± 0.09
Stomach	0.17 ± 0.07	0.14 ± 0.12	0.24 ± 0.33	0.77 ± 0.34	2.77 ± 1.74
Spleen	0.25 ± 0.05	0.16 ± 0.07	0.07 ± 0.02[b]	1.77 ± 1.44	1.08 ± 0.54
Liver	0.83 ± 0.29	0.48 ± 0.08	0.32 ± 0.10	3.78 ± 1.06	8.01 ± 3.58
Pancreas	0.15 ± 0.04	0.08 ± 0.02	0.05 ± 0.01[b]	0.49 ± 0.21	0.46 ± 0.11
Adrenals	0.40 ± 0.06	0.32 ± 0.25	0.08 ± 0.03[b]	1.23 ± 0.51	1.16 ± 0.61
Kidney	4.37 ± 1.04	1.92 ± 0.46[b]	1.28 ± 0.32[b]	14.84 ± 7.21	14.40 ± 1.65
Lungs	0.56 ± 0.13	0.32 ± 0.13	0.16 ± 0.05[b]	1.86 ± 0.37	2.27 ± 0.44
Heart	0.20 ± 0.07	0.12 ± 0.04	0.12 ± 0.04	0.67 ± 0.15	0.70 ± 0.18
Muscle	0.16 ± 0.03	0.08 ± 0.03[b]	0.09 ± 0.11	0.49 ± 0.10	0.56 ± 0.15
Bone	0.20 ± 0.05	0.22 ± 0.16	0.04 ± 0.01[b]	0.60 ± 0.24	0.40 ± 0.27
Brain	0.05 ± 0.01	0.04 ± 0.03	0.01 ± 0.00[b]	0.11 ± 0.06	0.07 ± 0.03
Tumour	**0.81 ± 0.15**	**0.41 ± 0.10[b]**	**0.35 ± 0.17[b]**	**1.93 ± 0.26**	**2.30 ± 0.53**
Tumour/liver	1.03 ± 0.21	0.85 ± 0.16	1.04 ± 0.22	0.48 ± 0.15	0.30 ± 0.05
Tumour/blood	1.29 ± 0.11	1.31 ± 0.26	1.37 ± 0.24	1.28 ± 0.18	2.67 ± 0.72
Tumour/muscle	5.02 ± 0.22	5.63 ± 1.52	6.26 ± 2.74	4.07 ± 0.87	4.18 ± 0.84

Biodistribution and ratios are at 1 h post-injection. Values (%ID/g) are presented as mean ± standard deviation.
[a]Blocked by pre-injection of acetazolamide (AZA) 1 h before administering radiotracer.
[b]Pre-injection significantly reduced uptake of the same organ for the tracer ($p<0.05$)

Positive correlation between hypoxia and CA-IX expression has previously been demonstrated using PET hypoxia tracers and CA-IX immunohistochemical staining[234], but not vice versa due to the lack of suitable CA-IX tracers. Using ^{68}Ga-DOTA-AEBSA as the imaging tracer, PET studies were performed at 17, 24 and 33 days after cell-inoculation for one mouse which exhibited slower initial tumour growth compared to other subjects (Figure 5.7). Absolute uptake and overall contrast improved as the tumour grew over the three imaging sessions. Tumour size and hottest 2 × 2 voxel cluster (based on drawn ROIs) were 91.8 mm^3 and 0.21 %ID/g, 830.9 mm^3 and 0.40 %ID/g, and 1225.1 mm^3 and 0.65 %ID/g for 17, 24, and 33 days, respectively. By the second and third imaging session, distribution of radioactivity in tumour is visibly heterogeneous with several areas of focality. While additional studies are needed to determine if uptake of ^{68}Ga-DOTA-AEBSA corresponds to the degree of hypoxia, the clinical utility of tracers will be improved if they can serve as surrogate hypoxia imaging agents. As CA-IX is an endogenous marker of hypoxia, tumours that express CA-IX are not only susceptible to emergent CA-IX inhibitors, but to hypoxia-targeting therapies as well.

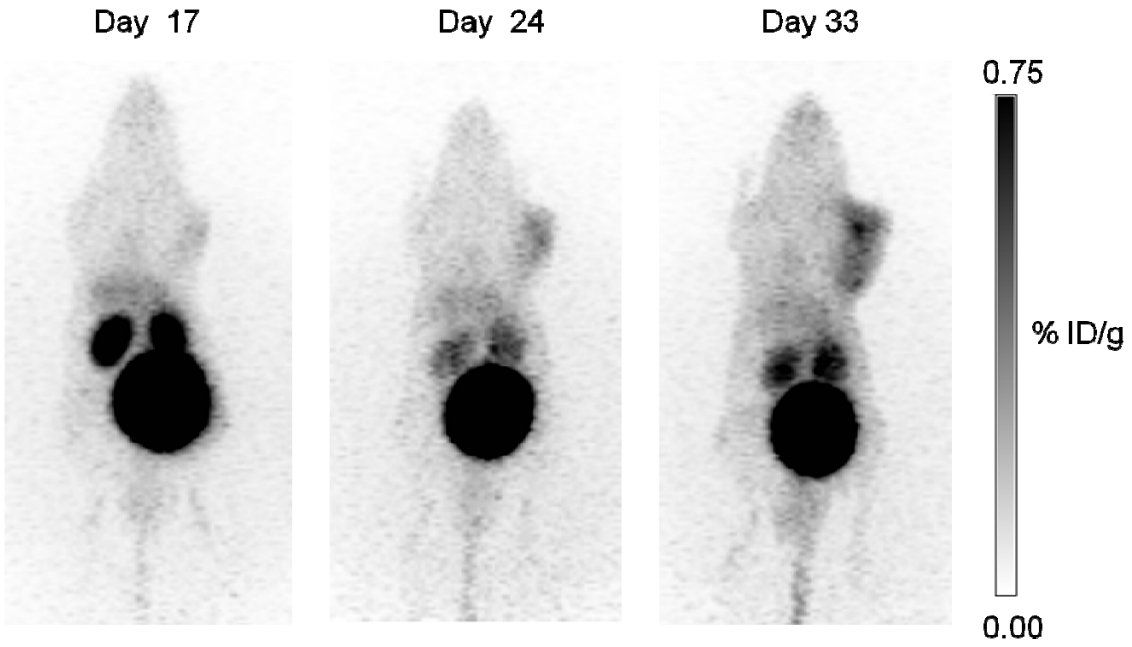

Figure 5.7 Longitudinal study: uptake of ^{68}Ga-DOTA-AEBSA in HT-29 tumour xenograft increases as tumour grows. This tumour bearing mouse was imaged 17, 24 and 33 days post-cell inoculation with ^{68}Ga-DOTA-AEBSA.

Historically the clinical detection of CA-IX has mainly been facilitated by the mAb cG250. cG250 binds to the proteoglycan-like domain of CA-IX and have been explored for imaging[127-129] and therapy[172, 173]. ^{124}I-cG250 advanced to phase III clinical trials for the diagnosis of CCRCC with PET,[127] but whether this antibody will be available for clinical use remains unclear. The high molecular weight of mAbs combined with slow uptake kinetics and high cost of ^{124}I, could limit their usefulness or clinical acceptance. On the other hand, there is significant interest in developing small molecule inhibitors for imaging CA-IX in vivo.

The development of CA-IX inhibitors as PET imaging agents have been met with limited success. Those that have been evaluated in the pre-clinical setting have shown low tumour uptake, lack of isoform selectivity, and/or instability in vivo.[196, 235-237] Recently, we reported the synthesis and biological evaluations of four ^{18}F-labeled sulfonamide derivatives for CA-IX imaging.[220] For each tracer, HT-29 tumour xenografts were readily visualized with good contrast (tumour-to-muscle ratios of 3.18-9.55). In vivo selectivity for CA-IX was achieved through the use of a multivalent design; however, absolute uptake in tumour remained low (0.30-0.64 %ID/g at 1 h p.i.). Furthermore, high sequestration of activity in liver and GI tract precludes their use for imaging lesions in these organs. By comparison, all three tracers presented in this chapter had higher absolute uptake with comparable contrasts. ^{68}Ga-DOTA-AEBSA and to a lesser extent ^{68}Ga-DOTA-$(AEBSA)_2$ showed favourable pharmacokinetic profiles that will enable detection of lesions within the abdominal thorax. Given the prognostic and therapeutic significance of CA-IX, we believe that polyaminocarboxylate chelator-conjugated sulfonamides warrant further investigation as promising imaging agents. Further optimization could be possible by tailoring charge properties or hydrophilicity of the multimeric compounds to decrease liver accumulation and hepatobiliary clearance.

5.4 Conclusion

We have demonstrated that ^{68}Ga-labeled benzenesulfonamide inhibitors can be used for non-invasive imaging of CA-IX. Easily produced, with favourable pharmacokinetics and rapid tumour targeting, these tracers represent attractive alternatives to conventional mAb-based imaging systems. Clinically, these nanomolar affinity compounds could enable physicians to determine if patients' tumours express sufficiently high levels of CA-IX to evaluate their

suitability for treatments. As CA-IX is considered an endogenous marker for hypoxia in certain cancer subtypes, these compounds might be useful for hypoxia imaging. Further validation is warranted to assess the suitability of these compounds for this application.

Chapter 6: Antibodies and Antibody Mimetics for Imaging – Pilot Studies

6.1 Introduction

The advent of hybridoma technology in conjunction with advancements in serological techniques has made mAbs one of the more powerful pharmacological tools for basic research and medicine[123, 238]. The tumouricidal effects of mAbs are derived from several mechanisms[105]. mAbs can cause direct cell death by abrogating cell signaling and inducing apoptosis[105], or by delivering cytotoxic drugs or radiation as antibody conjugates[239, 240]. Additionally, mAbs can elicit indirect immune-mediated cell killing through antibody-dependent cell-mediated cytotoxicity (ADCC), complement dependent cytotoxicity (CDC), or antibody-dependent cell phagocytosis (ADCP)[241-243].

Since its discovery in 1986, the mAb cG250 has been investigated extensively for CA-IX targeted therapy[244, 245]. cG250 was evaluated as adjuvant therapy for CCRCC patients in a phase III clinical study; however, it failed to meet primary endpoint as no improvement in median disease-free survival was observed compared to placebo[172, 246]. While cG250 has been shown to facilitate ADCC[247], it does not inhibit CA-IX enzymatic activity as it binds to the PG-like domain. It has been hypothesized that mAbs that can inhibit CA-IX activity and induce immune-mediated cell killing would be more efficacious than cG250[220]. As such, different research groups have focused on developing mAbs that target the catalytic site of CA-IX[248-251]. In collaboration with Drs. Shoukat Dedhar (BCCA), Anne Lenferink (NRC) and Maureen O'Connor (NRC) who are interested in developing therapeutic agents targeting CA-IX, we evaluated 3 high-affinity mAbs raised against the extracellular domain of CA-IX (Table 6.1). Two of these mAbs bind the PG-like domain of CA-IX, while the epitope for the remaining mAb was determined to be the catalytic domain. We conjugated these antibodies with DTPA as a chelator, followed by radiolabeling with ^{111}In, using non-selective polyclonal IgG as a negative control. SPECT imaging studies were performed to evaluate mAb uptake in vivo and to guide therapeutic development of ADCs.

The work presented in this chapter is not published. The mAbs used for radiolabeling and imaging experiments were obtained from our collaborators Drs. Shoukat Dedhar (BCCA), Anne Lenferink (NRC), and Maureen O'Connor (NRC).

Table 6.1 Characterization of mAbs raised against the extracellular domain of CA-IX

Name	Isotype	Epitope	Internalization	K_i (nM)[a]
Ab01	Mouse IgG1	PG-like domain	No	0.12
Ab02	Mouse IgG1	PG-like domain	Yes	0.76
Ab03	Mouse IgG1	Catalytic domain	Yes	0.33

[a]Binding affinity determined by surface plasmon resonance

In addition to mAbs, we investigated the use of an affibody as an alternative protein scaffold for CA-IX imaging. Affibody and other antibody mimetics offer high affinity antigen recognition, tissue penetrance, stability, and quick pharmacokinetics (Figure 6.1). As discussed in Chapter 1, Honarvar *et al.* reported the successful affibody-mediated imaging of CA-IX expression in SK-RC-52 xenograft mice with ^{99m}Tc-HEHEHE-ZCAIX:1[154]. ZCAIX:1, also known as Z09781 in a patent application, had good binding affinity to CA-IX with a K_d value of 1.3 nM[252]. Biodistribution data showed high and sustained tumour uptake: 22.3 ± 3.2 and 9.7 ± 0.7 %ID/g at 1 and 4 h p.i., respectively. This corresponded to tumour-to-blood and tumour-to-muscle ratios of 26 ± 4 and 61 ± 14 at 1 h p.i., and 53 ± 1 and 104 ± 52 at 4 h p.i., respectively[154]. Since a CCRCC cancer cell line was used, we were interested to see if Z09781 would yield similar results in a hypoxia CA-IX model. Therefore, we proceeded to radiolabel Z09781 with ^{68}Ga for PET imaging studies using HT-29 tumour xenograft mice.

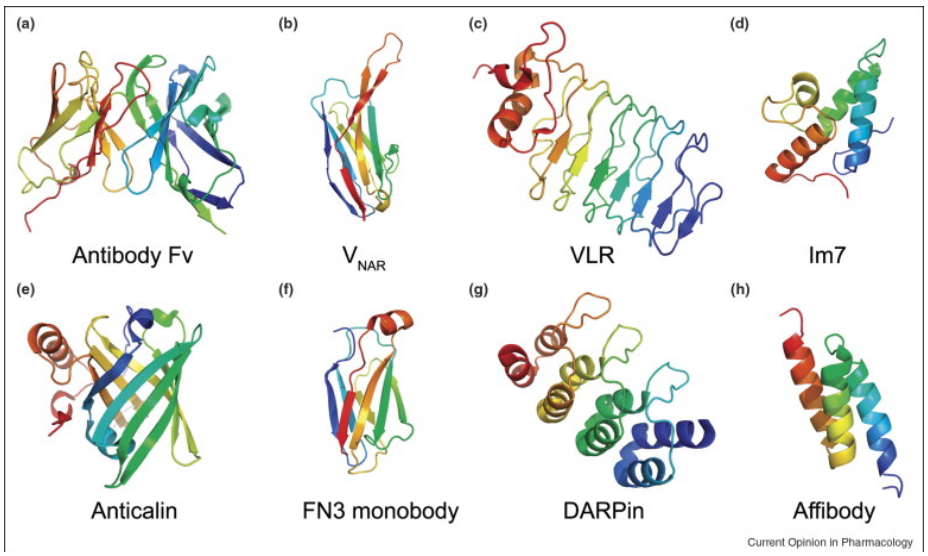

Figure 6.1 Engineered protein scaffolds. This figure shows representative protein models of antibody mimetics that have been engineered for antigen recognition and targeting. Figure reproduced with permission from Nuttall and Walsh[253].

6.2 Materials and Methods

All chemicals and solvents unless otherwise specified were obtained from commercial sources, and used without further purification. The three CA-IX mAbs were obtained from the National Research Council (NRC). Mouse polyclonal IgG1 control was purchased commercially from Sigma. Purification and quality control of precursors and radiotracers were performed on an Agilent (Santa Clara, CA) HPLC system equipped with a model 1200 quaternary pump, a model 1200 UV absorbance detector, and a Bioscan (Washington, DC) NaI scintillation detector. The HPLC columns used were a size exclusion column (Phenomenex SEC-3000, 5 µ, 300 × 7.8 mm), a semipreparative column (Phenomenex C18, 5 µ, 250 × 10 mm), and an analytical column (Phenomenex Luna C18, 5 µ, 250 × 4.6 mm). [^{68}Ga]$GaCl_3$ was eluted from either a 30-mCi ^{68}Ge/^{68}Ga generator from Eckert & Ziegler (Berlin, Germany) or a 50-mCi generator from iThemba LABS (Faure, South Africa). Radioactivity of tracers were measured using a Capintec (Ramsey, NJ) CRC®-25R/W dose calibrator. The radioactivity of mouse tissues collected from biodistribution studies were counted using a Perkin Elmer (Waltham, MA) Wizard2 2480 automatic gamma counter.

6.2.1 Conjugation of *p*-SCN-Bn-DTPA to mAbs

mAbs with excipients were first washed with PBS and recovered by centrifugal purification. For each mAb, 1 mg was conjugated with *p*-SCN-Bn-DTPA (Macrocyclics) in 500 µL of PBS (buffered to pH 8.9 with 0.1 M Na_2CO_3). A 5:1 molar ratio of chelator to mAb was used and the reactions were allowed to proceed overnight at room temperature with gentle agitation. After incubation, the reactant mixtures were purified using using 50 kDa amicon filters (Millipore) to remove any unconjugated chelator. *p*-SCN-Bn-DTPA-mAb conjugates were washed thrice with PBS before being resuspended in 0.15 M ammonium acetate (pH 5.5) and stored as 0.1 mg aliquots at -20 °C.

6.2.2 ^{111}In Radiolabeling for *p*-SCN-Bn-DTPA-mAbs

^{111}In was purchased from Nordion (Vancouver, Canada) as [^{111}In]$InCl_3$ solution. 0.9% NaCl solution was added to create a ~185 MBq/100 µL stock solution. In a reaction vial, 500 µL of

0.1 M HEPES solution (pH 5.5) was added to 100 µL of [^{111}In]$InCl_3$. For each mAb, 0.4 mg of *p*-SCN-Bn-DTPA-mAb conjugates were added to the ^{111}In/HEPES solution and incubated for 1 h at room temperature. The crude reactions were purified using 50 kDa amicon filters (Millipore) and radiochemical purity was determined by SEC HPLC analysis per published procedures[254].

6.2.3 Synthesis of Cys-Z09781

The synthesis of Cys-Z09781 was performed using the standard Fmoc solid-phase approach on an AAPPTec Endeavor 90 peptide synthesizer (Louisville, KT). Starting with Fmoc-Lys(Boc)-Rink-Amide-MBHA resin, the N^{α}-Fmoc protecting group was removed by 20% piperidine in DMF. Subsequently, each Fmoc-protected aa was coupled to the sequence with standard in situ activating reagent HBTU (3 eq), HOBT (3 eq), DIEA (6 eq), in DMF. The process was repeated until the sequence was completed (CAEAKYAKENLFAGWEIDDLPNLTEDQRNAFIYKLW DDPSQSSELLSEAKKLNDSQAPK). At the end of elongation, the peptides were cleaved from resin and all protecting groups were concomitantly removed by treatment TFA/TIS/DI water/EDT/Thioanisole/Phenol at 81.5/1.0/5.0/2.5/5.0/5.0 ratio for 4 h at room temperature. The solution was filtered and the peptide was precipitated with 10 times volume of diethyl ether. The precipitate was collected by centrifugation, dissolved in water, and lyophilized. The dried product was resuspended in water and purified by HPLC on a semipreparative column using 25-35% acetonitrile gradient containing 0.1% TFA in 30 min at a flow rate of 4.5 mL/min (t_R: 24.3 min). MS(ESI) Calcd. for Cys-Z09781: m/z 6741.67; Found: m/z 6746.80 ($[M+5H]^{5+}$).

6.2.4 Conjugation of NOTA to Cys-Z09781

A cysteine residue was introduced at the *N*-terminus of the affibody to facilitate site-specific conjugation with thiol-maleimide chemistry. In a 4-mL reaction vial, 1.9 mg of purified Cys-Z09781 was dissolved in 950 µL of 0.2 M ammonium acetate (pH 6.5) and incubated with 10 µL of 0.5 M TCEP and 0.46 mg of maleimido-mono-amide-NOTA (Macrocyclics). The reaction was allowed to proceed at 40 °C for 2 h with gentle agitation under inert conditions (vial filled with N_2 gas). The reaction was purified by HPLC on a semipreparative column using 20-40%

acetonitrile gradient containing 0.1% TFA in 30 min at a flow rate of 4.5 mL/min (t_R: 22.1 min). MS(ESI) Calcd. for Cys[NOTA]-Z09781: m/z 7167.15; Found: m/z 7173.59 ($[M+5H]^{5+}$).

6.2.5 ^{68}Ga Radiolabeling for Cys[NOTA]-Z09781

$^{68}GaCl_3$ was purified following published procedures[231]. Purified $^{68}GaCl_3$ (806 – 899 MBq in 0.5 mL) was added to 100 µg of Cys[NOTA]-Z09781 in 0.7 mL of 2 M HEPES buffer (pH 5.0) with 5% glycerol. Reaction was heated using a Danby DMW7700WDB microwave (Finday, OH) at power setting 2 for 1 min. For purification, the reaction was loaded onto a PD10 column, and eluted with 0.9% saline in fractions. The fractions containing the radiolabeled product were pooled and a small aliquot was subsequently taken for QC HLPC. Radiochemical yield, purity and specific activity, was determined by HPLC on an analytical column eluted with 31% acetonitrile at a flow rate of 2 mL/min (t_R: 10.8 min).

6.2.6 In Vivo Evaluations

All animal studies were performed in accordance with the Canadian Council on Animal Care guidelines and approved by the Animal Care Committee of the University of British Columbia. Male immunodeficient NOD.Cg-*Prkdc*^{scid}*Il2rg*^{tm1Wjl}/SzJ (NSG) mice bred in-house at the Animal Research Centre, BC Cancer Research Centre were used for this study. Under anesthesia with 2.5% isoflurane in 2.0 L/min of oxygen, mice were subcutaneously inoculated with 5×10^6 HT-29 cells (in 100 µL PBS and BD Matrigel Matrix at 1:1 ratio) under the right dorsal flank. Biodistribution studies and imaging were performed when tumours reached 7-9 mm in diameter.

6.2.6.1 Biodistribution Studies

Tumour bearing mice were injected intravenously with ~0.37 MBq of ^{68}Ga-Cys[NOTA]-Z09781 or ~3.7 MBq of ^{111}In-labeled mAb. After an uptake period of either 2, 72, or 168 h, mice were euthanized by CO_2 asphyxiation. Blood was promptly withdrawn, and organs/tissues of interest were harvested, rinsed with saline, blotted dry and weighted. Radioactivity in collected tissues was counted, normalized to the injected dose and expressed as the percentage of the injected dose per gram of tissue (%ID/g).

6.2.6.2 SPECT/CT Imaging

Tumour bearing mice were injected intravenously with ~37 MBq of ^{111}In-labeled mAb. After injection, mice were allowed to recover and roam freely in their cages. At selected time points, mice were sedated with 2% isoflurane inhalation and placed in a MILabs **(**Utrecht, Netherlands) U-SPECT II/CT scanner for image acquisition. Body temperature was maintained by a heating pad during acquisition. A 5 min baseline CT scan was obtained for localization with voltage setting at 60 kV and current at 615 μA. A single static emission scan was acquired for 1 h using an ultra-high-resolution multi-pinhole rat-mouse (1 mm pinhole size) collimator. Data were acquired in list mode acquisition, reconstructed using the U-SPECT II software, and co-registered for alignment. The SPECT images were reconstructed using maximum-likelihood expectation maximization (3 iterations), pixel-based ordered subset expectation maximization (16 subsets) and a post-processing filter (Gaussian blurring) of 0.5mm centered at photopeaks 171 keV and 245 keV with a 20% window width. Imaging files were visualized with either PMOD or Inveon Research Workplace software. At the conclusion of the final imaging time point, mice were euthanized and processed for biodistribution as described above.

6.2.6.3 PET/CT Imaging

PET imaging studies of ^{68}Ga-Cys[NOTA]-Z09781 were conducted using a Siemens Inveon microPET/CT scanner. Under 2.5% isoflurane anesthesia in oxygen at 2.0 L/min, 3.7-7.4 MBq of ^{68}Ga-Cys[NOTA]-Z09781 in a volume of 200 μL was administered intravenously through the caudal vein. Under 2.5% isoflurane anesthesia in oxygen at 2.0 L/min, 3.7-7.4 MBq of ^{68}Ga-Cys[NOTA]-Z09781 in a volume of 200 μL was administered intravenously through the caudal vein. At 2 h p.i., a CT-based attenuation scan was performed with exposure settings of 60kV, 500 μA and 500 ms, using three sequential bed positions with a 33% overlap, and 220 degree continuous rotation prior to the 10 min PET acquisition. The body temperature of mice was maintained at 37 °C with the use of thermal pads. The PET list mode data were converted into a sinogram file with default 3D histogram settings prior to reconstruction using 2 iterations of 3D - Ordered Subset-Expectation Maximization (3D OSEM) and 18 iterations of Maximum A Priori (MAP). At the conclusion of the final imaging time point, mice were euthanized and processed for biodistribution as described above.

6.3 Results and Discussion

We evaluated three novel mAbs raised against the extracellular domain of CA-IX for SPECT/CT imaging. These mAbs were initially developed at the NRC for therapeutic applications. These mAbs target either the PG-domain or catalytic domain of CA-IX with subnanomolar affinity (Table 6.1). Based on in vitro assays done at the NRC, Ab02 and Ab03 were found to undergo internalization upon binding to CA-IX, while Ab01 is considered a non-internalizing mAb. For mAbs that are designed to deliver drugs or radiation, internalization can bring the therapeutic payload closer to intracellular targets (microtubule, DNA etc.)[124]. If the mechanism of action of a mAb is to bind the target receptor to inhibit signalling, or to elicit immunomodulatory response (ADCC, CDC, or ADCP), it is desirable for the antigen-mAb complex to not be rapidly internalized[124]. This enables the Fab region of the mAb to continue signal blockade of the receptor, and maximizes the availability of the Fc region to interact with immune effector cells[124].

For each mAb, we performed conjugation with *p*-SCN-Bn-DTPA to facilitate ^{111}In labeling (Figure 6.2). With a physical $t_{1/2}$ of 2.80 d, ^{111}In has long been used for mAb-based imaging[255, 256] and is a biological surrogate for therapeutic radionuclides, ^{90}Y and ^{177}Lu[257, 258]. In recent years, in addition to imaging ^{111}In-bioconjugates have received significant interest as Auger electron emitting radiotherapeutics[259, 260]. As a residualizing radionuclide, ^{111}In will reside in the cell even if the radiolabeled mAb is internalized and degraded[261, 262]. Radiolabeling procedures were adapted from published procedures[263]. Based on SEC HLPC analysis, we obtained good radiochemical yields (70-80%, n = 3) and radiochemical purity (> 95%) after centrifugal purification for the radiolabeled mAbs. With limited quantity of each mAb, the immunoreactivity fractions were not determined for this pilot study.

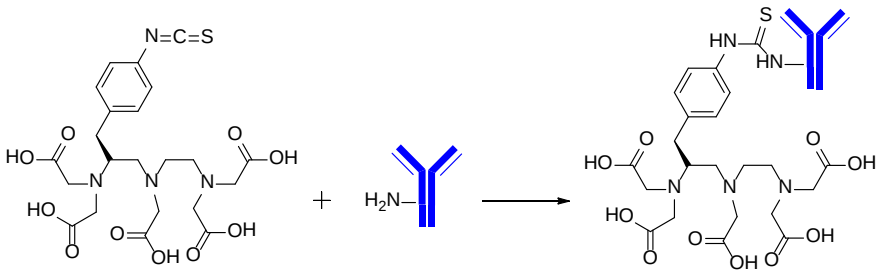

Figure 6.2 DTPA conjugation for mAbs. The bifunctional chelator *p*-SCN-Bn-DTPA was conjugated to the CA-IX mAbs for ^{111}In labeling.

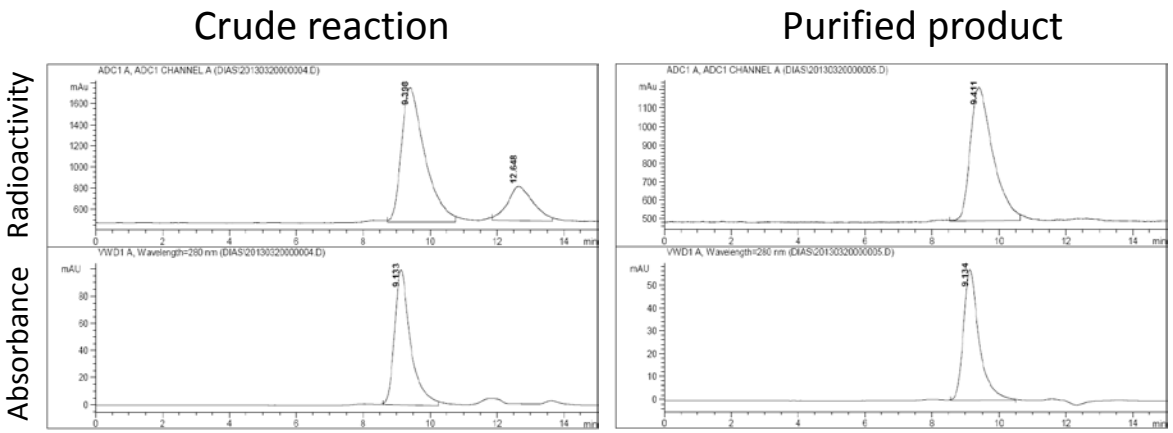

Figure 6.3 Representative radiochromatogram of an ^{111}In radiolabeled mAb, before and after centrifugal filtration to remove unbound radioisotopes. Top panel is radioactivity (mAu), while bottom panel is absorbance at 280 nm (mAU). t_R of radiolabled mAb is approximately 9.4 min.

As absolute tumour uptake is determined in part by the clearance rate of a radiopharmaceutical, large molecules like mAbs generally display higher uptake than small molecule agents. The enhanced permeability and retention (EPR) effect[264] is beneficial for macromolecule-based therapeutics; however, it obscures evaluation of targeted imaging by overestimating specific uptake. In order to discern the contribution of the EPR effect, we included the use of a non-specific polyclonal IgG for in vivo studies. Imaging experiments were performed in immunodeficient mice bearing HT-29 colon carcinoma xenografts (Figures 6.4 and 6.5). From the SPECT/CT images, there was significant accumulation of Ab02 in tumour compared to Ab01, Ab03, and non-specific polyclonal IgG. As early as 24 h p.i., Ab02 was readily taken up by tumour with high penetrance enabling the acquisition of high contrast images. Radioactivity was retained in the tumour over the course of 7 days, while progressive clearance was observed for non-target tissues including the heart, liver and spleen. Conversely, the accumulation of Ab01 and Ab03 in tumour was observed predominantly at the peripheral boundaries similar to IgG control.

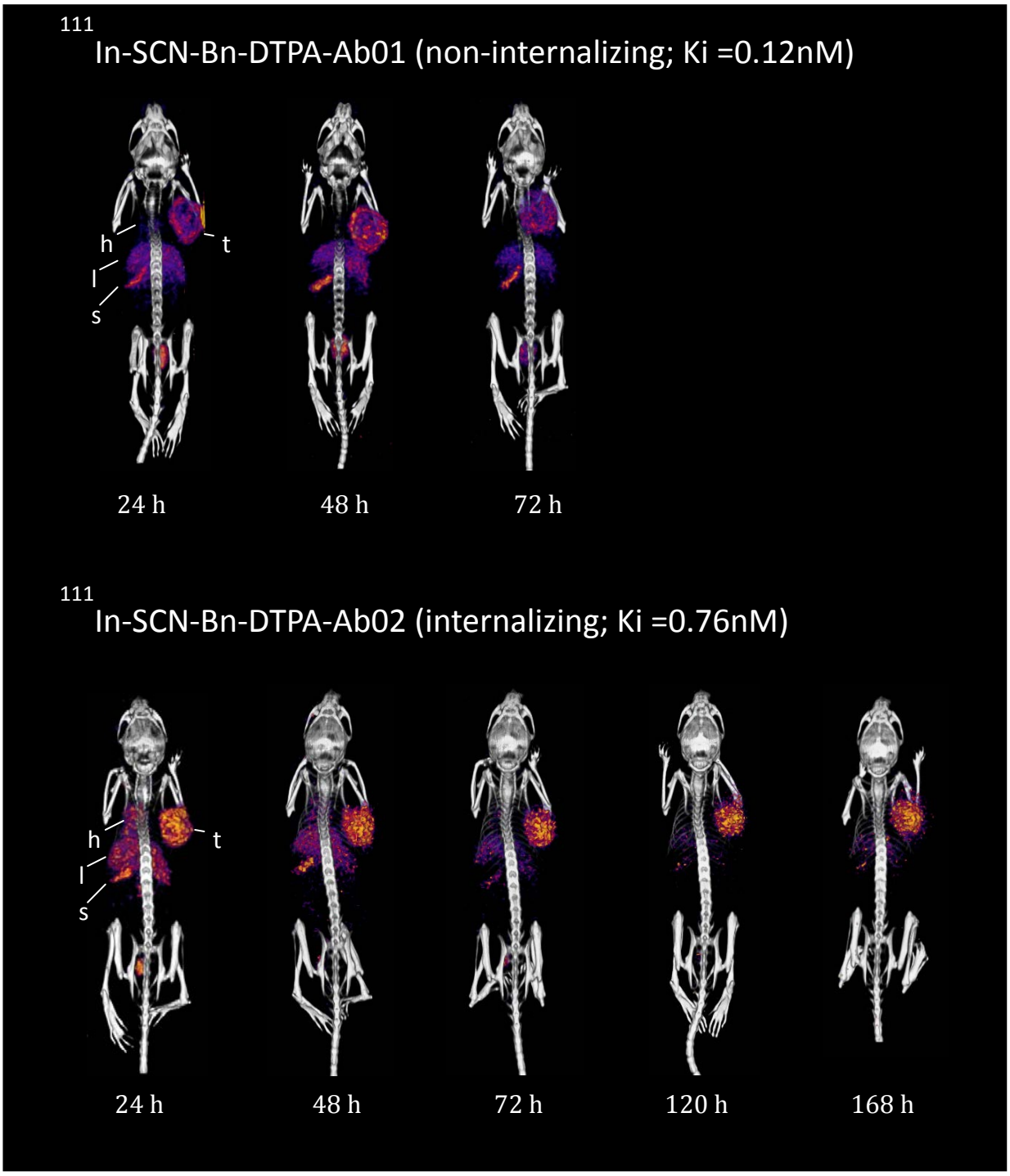

Figure 6.4 Sequential SPECT/CT images obtained with ^{111}In-SCN-Bn-DTPA-Ab01 and ^{111}In-SCN-Bn-DTPA-Ab02. ^{111}In-SCN-Bn-DTPA-Ab01 uptake was primarily observed at the peripheral boundaries, while ^{111}In-SCN-Bn-DTPA-Ab02 showed significant retention and accumulation of in tumours with progressive decrease in background. t = tumour; h = heart; l = liver; s = spleen

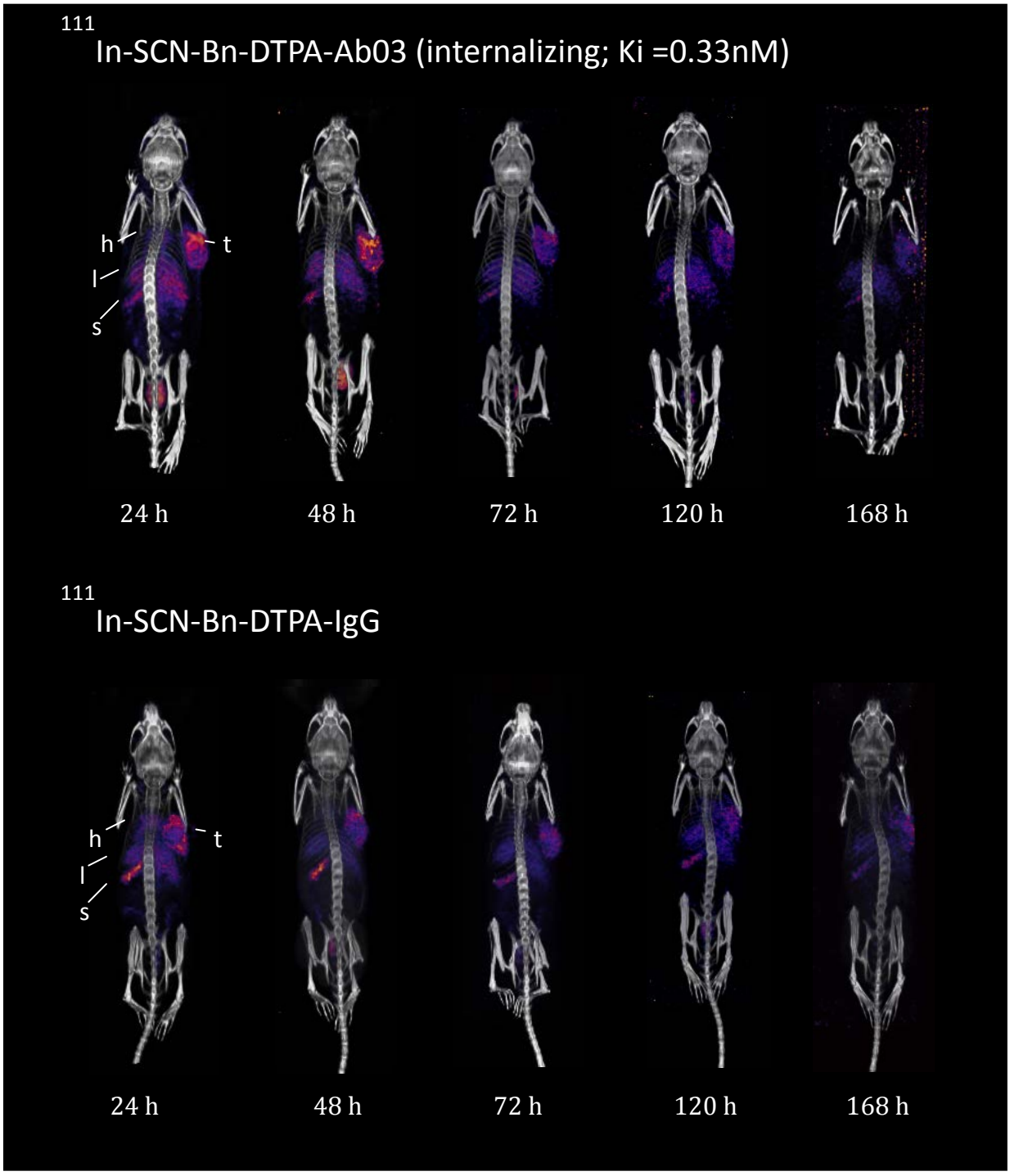

Figure 6.5 Sequential SPECT/CT images obtained with ^{111}In-SCN-Bn-DTPA-Ab03 and ^{111}In-SCN-Bn-DTPA-IgG. ^{111}In-SCN-Bn-DTPA-Ab03 uptake was initially observed at the peripheral boundaries but showed progressive clearance from tumour. By day 3, uptake of ^{111}In-SCN-Bn-DTPA-Ab03 was similar to ^{111}In-SCN-Bn-DTPA-IgG. t = tumour; h = heart; l = liver; s = spleen

Since mAbs circulate in the blood for many days, this provides opportunities for repeated antigen-mAb interactions and progressive accumulation of tumour-specific mAbs. In contrast, non-specific mAbs typically exhibit transient passive accumulation followed by progressive clearance from the tumours. Biodistribution studies were performed to determine absolute uptake in tumour and non-target tissues (Table 6.2). Of the evaluated mAbs, the highest tumour uptake was observed for Ab02 (37.84 ± 4.69 %ID/g at 72 h p.i.). The uptake of Ab02 in tumour was approximately two-fold higher than Ab01 (19.09 ± 4.81 %ID/g) and Ab03 (18.38 ± 3.07 %ID/g). With the exception of blood, spleen, and tumour, uptake in non-target tissues were relatively consistent for each mAb. A potential reason for the enhanced uptake of Ab02 is its slow rate of clearance from blood (20.62 ± 4.33 %ID/g at 72 h p.i.). At 168 h p.i., uptake in tumour for Ab02 was 35.64 %ID/g, suggesting that there is retention at the tumour site. By comparison, the uptake of the polyclonal IgG control was 14.01 ± 0.23 %ID/g at 168 h p.i. While Ab02 yielded promising data, further studies are needed to fully assess its potential for targeting CA-IX (greater sample size at multiple time points).

As cG250 is considered the metric novel mAbs targeting CA-IX are evaluated against, an overview of the different radiolabeled cG250 immunoconjugates that have been investigated in preclinical setting is provided in Table 6.3. In the most comprehensive study to date, Brouwers *et al.* demonstrated that radionuclide and chelation selection can affect stability, biodistribution and therapeutic efficacy of radioimmunotherapy with cG250[265]. Depending on the radioisotope/chelator combination used, tumour uptake ranged from 14.0 ± 3.0 %ID/g (for ^{125}I-cG250) to 113.3 ± 24.7 %ID/g (for ^{177}Lu-SCN-Bz-DTPA-cG250) at 3 d p.i. Brouwers *et al.* evaluated ^{111}In-DTPA-cG250 for targeting SK-RC-52 tumour xenografts (4.9 ± 2.9 %ID/g at 3 d p.i.); however the studies were performed in nude rats[266]. The study that offers the fairest comparison would be the one performed by Carlin *et al*. using ^{111}In-DOTA-cG250 with the HT-29 model (20.1 ± 4.8 %ID/g at 2 d p.i.)[217]. Ideally, for future studies we will be able to obtain cG250 and perform a side-by-side comparison with our CA-IX mAbs while holding variables like isotope, chelator, tumour model, host, and timepoint consistent.

Table 6.2 Biodistribution and tumour-to-nontarget ratios for ^{111}In-SCN-Bn-DTPA-mAbs.

Organ	**^{111}In-SCN-Bn-DTPA-Ab01**	**^{111}In-SCN-Bn-DTPA-Ab02**		**^{111}In-SCN-Bn-DTPA-Ab03**		**^{111}In-SCN-Bn-DTPA-IgG**
	72 h p.i. (n = 4)	**72 h p.i. (n = 3)**	**168 h p.i. (n = 1)**	**72 h p.i. (n = 3)**	**168 h p.i. (n = 1)**	**168 h p.i. (n = 3)**
Blood	6.68 ± 1.41	20.62 ± 4.33	11.06	7.56 ± 0.60	9.65	11.37 ± 2.55
Fat	1.97 ± 0.69	1.88 ± 0.47	2.34	1.50 ± 0.15	0.84	1.92 ± 0.99
Intestine	3.05 ± 0.40	3.25 ± 0.30	1.76	2.69 ± 0.41	0.89	2.91 ± 1.57
Stomach	2.12 ± 0.38	2.21 ± 0.44	1.98	1.88 ± 0.24	0.84	3.08 ± 0.55
Spleen	78.16 ± 48.53	37.84 ± 4.69	32.12	53.88 ± 12.50	28.66	66.33 ± 22.81
Liver	18.66 ± 4.42	18.68 ± 2.22	14.41	17.46 ± 4.05	14.13	14.60 ± 2.55
Pancreas	2.69 ± 0.53	2.95± 0.59	2.09	2.36 ± 0.28	1.76	2.42 ± 0.94
Kidney	10.83 ± 2.78	12.86 ± 2.54	6.75	5.06 ± 0.80	6.31	6.95 ± 1.20
Lungs	5.88 ± 1.52	9.54 ± 0.92	9.55	5.22 ± 0.42	2.75	4.06 ± 2.92
Heart	5.49 ± 1.52	6.74 ± 1.04	3.50	4.77 ± 0.56	3.29	2.40 ± 1.81
Muscle	1.87 ± 0.38	2.26 ± 0.29	1.35	1.37 ± 0.02	0.34	1.48 ± 0.61
Bone	6.25 ± 2.98	4.46 ± 1.62	2.83	3.05 ± 0.86	1.61	5.55 ± 2.02
Brain	0.18 ± 0.05	0.33 ± 0.04	0.20	0.16 ± 0.04	0.11	0.25 ± 0.02
Tumour	**19.09 ± 4.81**	**37.84 ± 4.69**	**35.64**	**18.38 ± 3.07**	**8.20**	**14.01 ± 0.23**
Tumour/muscle	10.43 ± 2.81	15.22 ± 0.64	26.38	13.37 ± 2.14	24.07	10.47 ± 3.72

Values are presented as mean ± SD where possible

Table 6.3 Biodistribution of radiolabeled cG250 immunoconjugates

Paper	Bioconjugates	Tumour (%ID/g)	Model	Notes
Stillebroer *et al.*[128]	^{89}Zr-Df-cG250	48.7 ± 15.2 at 7 d	SK-RC-52	
	^{124}I-cG250	32.0 ± 22.9 at 7 d		
Brouwers *et al.*[265]	^{88}Y-cDTPA-cG250	46.6 ± 19.7 at 3 d	SK-RC-52	For therapy
	^{88}Y-SCN-Bz-DTPA-cG250	51.9 ± 7.0 at 3 d		
	^{88}Y-DOTA-cG250	44.4 ± 14.8 at 3 d		
	^{177}Lu-cDTPA-cG250	59.0 ± 11.5 at 3 d		
	^{177}Lu-SCN-Bz-DTPA-cG250	113.3 ± 24.7 at 3 d		
	^{177}Lu-DOTA-cG250	86.9 ± 14.5 at 3 d		
	^{125}I-cG250	14.0 ± 3.0 at 3 d		
	^{186}Re-MAG3-cG250	16.9 ± 2.8 at 3 d		
Brouwers *et al.*[266]	^{89}Zr-Df-cG250	5.0 ± 2.4 at 3 d	SK-RC-52	In nude rats
	^{111}In-DTPA-cG250	4.9 ± 2.9 at 3 d		
Cheal *et al.*[267]	^{89}Zr-Df-cG250	5.0 ± 2.4 at 11 d	SK-RC-52	Values derived from drawn ROIs
	^{124}I-cG250	4.9 ± 2.9 at 10 d		
Carlin *et al.*[217]	^{111}In-DOTA-cG250	20.1 ± 4.8 at 2 d	HT-29	IgG and Ab fragments
	^{111}In-DOTA-cG250-F(ab')$_2$	9.3 ± 2.1 at 1 d		
	^{111}In-DOTA-cG250-F(ab)	3.5 ± 1.7 at 3 d		
Hoeben *et al.*[268]	^{89}Zr-Df-cG250-F(ab')$_2$	1.66 ± 0.48 at 1 d	SCCNij3	Head and neck cancer model

For the remainder of this chapter, the discussion will primarily be focused on the synthesis and biological evaluations of the CA-IX affibody, ^{68}Ga-Cys[NOTA]-Z09781. As an antibody mimetic, affibodies have many advantages including protein solubility, thermodynamic stability, single polypeptide chain format, ease of production, and functionality in the absence of disulfide bridges[253]. We synthesized the affibody Z09781 (Figure 6.6) using a solid-phase approach and added a Cys residue at the *N*-terminus to facilitate site-specific conjugation of the NOTA chelator via thiol-maleimide chemistry. To complement the rapid pharmacokinetics, we selected ^{68}Ga as our imaging radionuclide. For radiolabeling experiments, ^{68}Ga-Cys[NOTA]-Z09781 was obtained in 64-73% decay-corrected radiochemical yields with 16.7 MBq/μg specific activity and > 99% radiochemical purity.

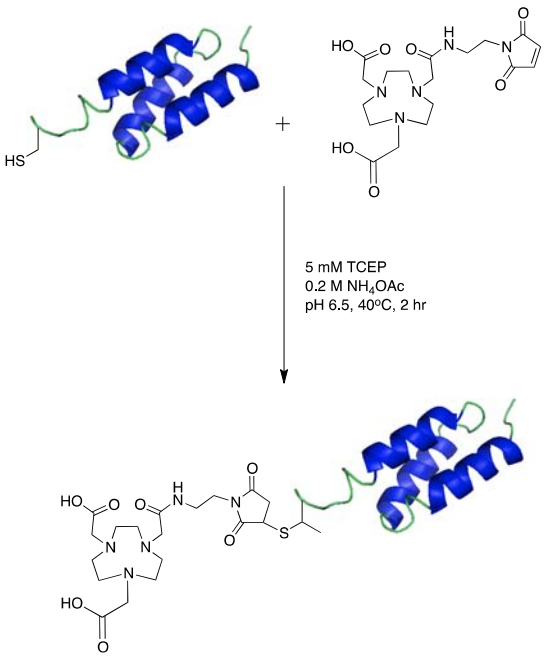

CAEAKYAK**E**<u>**NLF**</u>A<u>**GW**</u>EI<u>**DD**</u>LPNLT<u>**ED**</u>Q<u>**R**</u><u>**N**</u>A
F<u>**IY**</u>KL<u>**W**</u>DDPSQS<u>S</u>ELLSEAKKLNDS<u></u>QAPK

AA – confer binding specificity
<u>AA</u> – alpha helix domains
C – site specific conjugation via thiol-maleimide chemistry

Figure 6.6 Site-specific conjugation of NOTA to Cys-Z09781. The complete amino acid sequence of Cys-Z09781 is provided on the right.

Imaging and biodistribution studies (Figures 6.7 and 6.8) showed that ^{68}Ga-Cys[NOTA]-Z09781 was predominantly excreted through the renal pathway, with the kidneys retaining majority of the radioactivity (96.1 ± 10.4 %ID/g at 2 h p.i.). The clearance profile is consistent with other affibodies used for imaging[149-154]. ^{68}Ga-Cys[NOTA]-Z09781 allowed for clear delineation of HT-29 tumour xenografts in PET/CT images. With the exception of the kidneys and bladder, the highest uptake of activity was observed in tumour (1.05 ± 0.15 %ID/g at 2 h p.i.). The corresponding tumour-to-muscle and tumour-to-blood ratios were 11.8 ± 3.35 and 9.78 ± 1.59 respectively. The uptake of ^{68}Ga-Cys[NOTA]-Z09781 in tumour was similar to that achieved with the ^{68}Ga-labeled sulfonamides in Chapter 5, but with improved contrast. However, when compared to the results previously obtained by Honarvar *et al.* (22.3 ± 3.2 and 9.7 ± 0.7 %ID/g at 1 and 4 h p.i. for with ^{99m}Tc-HEHEHE-ZCAIX:1 with SK-RC-52 tumours), we observed substantially lower uptake values[154]. Due to the biological processes that drive CA-IX expression in HT-29 (hypoxia dependent) and SK-RC-52 (hypoxia independent; constitutive), we anticipated lower uptake for this study. Additionally, although the introduction of a cysteine residue for site-specific chelator conjugation and radiolabeling is a robust strategy[269, 270], it is possible that the change in radiometal/chelator composition negatively affected tumour uptake.

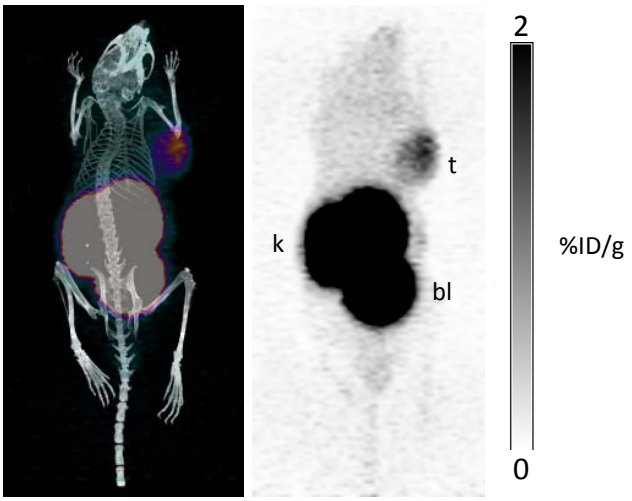

Figure 6.7 PET/CT images of ^{68}Ga-Cys[NOTA]-Z09781 at 2 h p.i. t = tumour; k = kidney; bl = bladder

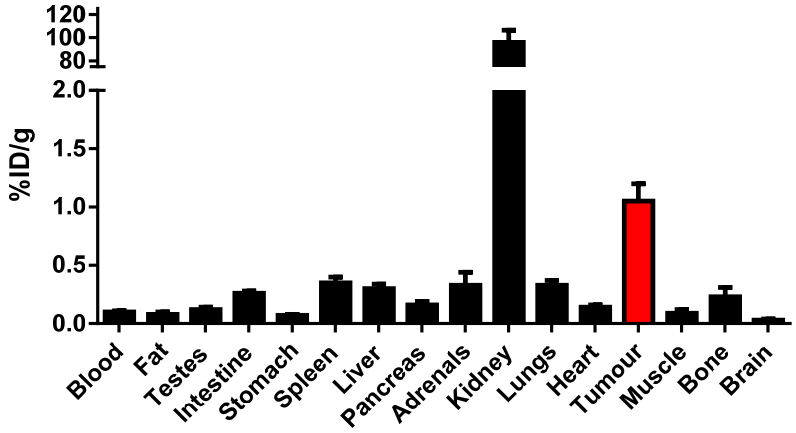

Figure 6.8 Biodistribution of ^{68}Ga-Cys[NOTA]-Z09781 in tumour and selected organs at 2 h p.i. (n=6).

6.4 Conclusion

In Chapter 6, we evaluated three novel mAbs as well as an affibody for CA-IX targeted SPECT and PET imaging. For each compound class, tracer pharmacokinetics and uptake was assessed in a human hypoxia cancer model. The mAbs were conjugated to *p*-SCN-Bn-DTPA and successfully radiolabeled with ^{111}In. ^{111}In-SCN-Bn-DTPA-Ab02 showed good tumour penetrance and yielded high contrast images as early as 24 h p.i. Conversely, neither Ab01 nor

Ab03 showed any significant accumulation in tumour compared to Ab02. As for affibody imaging, ^{68}Ga-Cys[NOTA]-Z09781 enabled clear visualization of HT-29 tumour xenografts with good contrast. Blocking studies are needed to determine tracer specificity of ^{68}Ga-Cys[NOTA]-Z09781.

Chapter 7: Conclusion

7.1 Summary of Study and Findings

Cancer is one of the leading causes of morbidity and mortality worldwide. According to the World Health Organization (WHO) 14.1 million individuals were diagnosed with cancer with 8.2 million succumbing to the disease in 2012, based on the most recent GLOBOCAN data[271]. By 2025, the incidence level is expected to increase to 20 million cases annually[271]. This global burden emphasizes the need for improved evidence-based strategies in cancer prevention, diagnosis and therapeutics. The goal of this thesis was to identify different molecular antigen recognition molecules that may serve as potential radiotracers for targeting CA-IX for cancer diagnosis. CA-IX is considered a surrogate marker for tumour hypoxia, and its expression is negatively correlated with patient survival. Hypoxic tumours can develop resistance to radiation and selected chemotherapies; therefore, the treatment for these cancers often involves combinatorial treatments especially at a disseminated stage. CA-IX represents a potential co-target, in synergy with other chemotherapies (ex. anti-VEGF therapies)[272]. We believe the establishment of a non-invasive companion diagnostic will accelerate the clinical adoption of CA-IX therapies.

In Chapters 2, 3, 4, and 5, we synthesized and evaluated a total of 12 small molecule inhibitors for imaging CA-IX expression in vivo. Initial efforts to image CA-IX expression based on literature-published inhibitors were unsuccessful due to tracer instability and lack of target specificity. Subsequently, we identified several $^{18}F/^{68}Ga$-labeled sulfonamide derivatives that effectively targeted CA-IX expressing tumour xenografts with good contrast. Isoform selectivity, the major challenge for the development of sulfonamide-based imaging agents, was achieved via a multivalent approach or by conjugating pharmacophores to polyaminocarboxylate chelators. In Chapter 6, we evaluated 3 high affinity mAbs raised against the extracellular domain of CA-IX, as well as a recently reported affibody for imaging studies. High and sustained uptake was observed for ^{111}In-SCN-Bn-Ab02, which yielded excellent contrast images as early as 24 h p.i. As an antibody mimetic, Z09781 generated good tumour to background ratios for imaging

hypoxia-induced CA-IX expression but absolute uptake was substantially lower than mAb-based imaging.

7.2 Strengths and Limitations of this Study

There were a number of strengths and limitations associated with this study. Our study represents a comprehensive evaluation of different antigen recognition molecules targeting CA-IX. With small molecule inhibitors, we explored two distinct strategies (valency and hydrophilicity) to confer CA-IX specificity. Through this process, we produced several tracers that not only enabled tumour visualization, but represented significant advancement over previous attempts. We pursued radiolabeling strategies that incorporated either ^{18}F or ^{68}Ga. Both radionuclides have short $t_{1/2}$, which are well-suited for biomolecules that display fast pharmacokinetics. Just as important, the general availability of ^{18}F (cyclotron) or ^{68}Ga (generator) suggests that these compounds can be readily adopted by other radiopharmaceutical facilities. Another strength in our research is the ability to guide development of emerging CA-IX therapeutics. SPECT imaging with ^{111}In-SCN-Bn-DTPA-mAbs provided meaningful information regarding targeting efficiency, tissue penetrance, and pharmacokinetics. Collectively, this thesis has strong translational components that can drive the growth of CA-IX diagnostics and therapeutics, which is important for personalizing medicine. As potential surrogates for hypoxia imaging, CA-IX tracers hold advantages for tumour-to-nontarget ratios and pharmacokinetics compared to established hypoxia PET agents (ex. FMISO, etc).

We used the HT-29 human colorectal cancer cell line for the evaluation of our radiotracers. Although this enabled us to compare our findings with previously published reports, further validation with additional cancer cell lines or patient derived xenograft (PDX) models are needed to confirm tracer utility. PDX models can better recapitulate the phenotype of cancer patients in terms of genomics, metastatic potential, and drug responsiveness; however, long tumour graft latency and variable engraftment rates may be limiting factors[273, 274]. In Chapter 5, we performed a longitudinal imaging study with ^{68}Ga-DOTA-AEBSA for one mouse and observed increase in focal uptake over three imaging sessions. We hypothesized that the non-homogeneous distribution of activity corresponded with CA-IX expression within hypoxic niches, but validation studies are required. Finally in Chapter 6, we evaluated three mAbs raised

against the extracellular domain of CA-IX as potential imaging agents. While promising results were obtained, the hybridoma cells producing the mAbs were low yielding and we did not have enough samples to complete analytical/imaging studies.

7.3 Overall Significance and Implications of Research Finding

Due to its role in mediating cell survival and distant metastasis under hypoxic conditions, CA-IX has emerged as a promising therapeutic and imaging biomarker. Although cG250 failed to meet primary endpoint in the phase III ARISER study, retrospective subset analysis revealed that patients with high CA-IX scores (> 2.0) experienced statistically significant improvement in disease-free survival after receiving treatment[172, 246]. CA-IX scoring for each patient was derived by multiplying staining intensity (1-3) by the fraction of positive cells (0-1). This finding highlights the potential effectiveness of anti-CA-IX therapies in the clinic, given proper patient stratification. Our research serves as a quantitative and non-invasive imaging platform for physicians to determine if patients' tumours express sufficiently high levels of CA-IX to make them candidates for treatments targeting this protein. Additionally, radiotracers may be useful for optimizing therapeutic dosage, and for assessing patients' response to treatments. Given the broad expression profile of CA-IX in solid cancers we anticipate that our findings will have a positive impact on cancer management leading to improved patient outcomes and quality of life.

7.4 Future Research Directions

7.4.1 Design of Cationic Sulfonamides

Leveraging the cell-surface expression of CA-IX, the design of CA-IX imaging agents has revolved around membrane impermeability. In this thesis, we pursued two approaches for developing cell-impermeable small molecule inhibitors. In Chapter 4, we used click chemistry to synthesize two trivalent sulfonamide inhibitors. The accumulation of MW served to limit passive perfusion into the cell. In Chapter 5, we conjugated a sulfonamide derivative to different polyaminocarboxylate chelators to enhance tracer hydrophilicity. With both strategies, we were able to observe uptake in HT-29 tumour xenografts with good visualization in PET images. A third strategy that we are interested in exploring is the introduction of a cationic motif onto

fluorinated sulfonamide derivatives. The transcellular uptake across the plasma membrane for charged or ionized species is generally limited[275]. Our collaborator, Dr. Supuran, reported the synthesis of several cationic sulfonamides using quaternary ammonium sulfates and observed favourable CA inhibition profiles[221, 222].

7.4.2 CA-IX Tracers as Surrogate Hypoxia Imaging Agents

One of the potential avenues for future research is to investigate if tracers designed for CA-IX imaging can be used as general hypoxia agents. One simple approach would be to take a CA-IX tracer (ex. ^{68}Ga-DOTA-AEBSA) and perform spatial correlation studies with ^{18}F-FMISO and determine if they co-localize in tumours (Figure 7.1). Another approach would be to evaluate changes in uptake and tumour-to-nontarget ratios under artificially induced conditions. Tumour-bearing mice can be divided into 4 groups prior in vivo studies (7% O_2 breathing, carbogen breathing + nicotinamide, 7% O_2 breathing followed by carbogen breathing + nicotinamide, non-treatment/control group). Mice in the 7% O_2 breathing group will represent the hypoxia-induced cohort, while mice assigned to carbogen breathing + nicotinamide treatment will represent the normoxia-induced cohort. The combination of carbogen breathing and nicotinamide administration has been used to reduce tumour hypoxia in clinical settings[276-278]. The third cohort of mice will be used to evaluate tracer uptake after reoxygenation (7% O_2 breathing followed by carbogen breathing + nicotinamide), while the last group will serve as baseline controls.

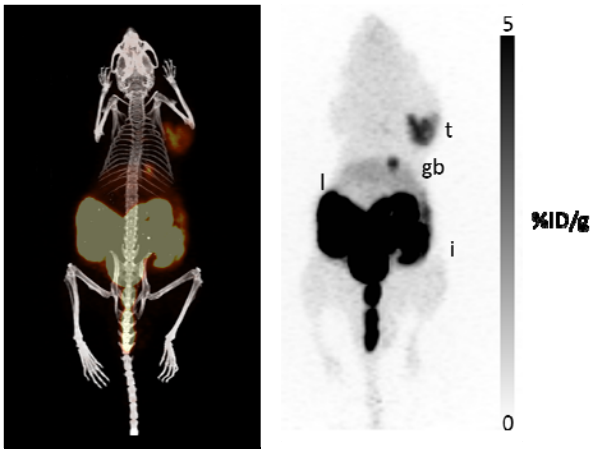

Figure 7.1 Maximal intensity projections of PET/CT (Left) and PET alone (Right) with ^{18}F-FMISO at 3 h p.i. Preliminary studies conducted with HT-29 tumour xenograft mice. t = tumour; gb = gallbladder; l = liver; i = gastrointestinal tract

7.4.3 Radiotherapy

Promising CA-IX tracers should be tested for their usefulness as radiotherapeutic agents. This can be done by replacing imaging radionuclides with therapeutic radionuclides. Alpha (α), beta (β^-), Auger electron emitters, and conversion electron emitters are classes of radionuclides that exert tumouricidal effects through radiation-induced DNA damage[279-286]. α-Particle emitters have the highest linear energy transfer (LET) and can cause more irreparable double-stranded DNA breaks[280]. They have a short tissue range (μm), which is advantageous for treating micro-metastasis where there are concerns of depositing energy beyond anatomical boundaries[280]. α-Particles are not dependent on tumour oxygenation[279], which is ideal considering CA-IX's expression in hypoxic niches. Although a higher concentration of β^- emitters is needed for comparable cell kill compared to α emitters, β^- emitters have a longer tissue range (mm)[281]. The long range of β^- emitters results in a "crossfire" effect where multiple cells can be targeted when only one binding event occurs[281]. Implicitly the crossfire effect decreases the need to target every cell, which is a challenge given the intrinsic heterogeneity of cancer. Auger electrons are low-energy electrons that are ejected from the atom in response to a downward transition of electrons within orbital shells[282, 283]. Since they have subcellular range (nm), Auger electrons must enter target cells to ensure proper delivery of radiation dose[282, 283]. Conversion electrons are monoenergetic orbital electrons that are ejected from unstable nuclei during the process of internal conversion. With high LET and a limited tissue range (nm), conversion electrons deliver high localized dose to diseased tissues[285, 287]. The radiometals used for therapy applications, ^{225}Ac, ^{212}Pb, and ^{213}Bi (α), ^{90}Y and ^{177}Lu (β^-), ^{111}In (Auger), and ^{114m}Sn (conversion electron) can be labeled onto CA-IX targeting moieties via bifunctional chelators[287-289]. For example, ^{111}In-SCN-Bn-DTPA-Ab02 investigated for SPECT imaging in Chapter 6 can be used for Auger-electron emitting therapy.

7.4.4 Clinical Translation of CA-IX Imaging Agents

To translate research findings into clinical setting, radiopharmaceuticals require dosimetry and acute toxicity studies for IND applications[290]. For dosimetry, biodistribution data can be used to estimate potential radiation absorbed doses for humans using the OLINDA/EXM software[291]. On the other hand, acute toxicity studies are more comprehensive. Healthy rats are

intravenously administered the radiotracer at 100-1000 times the expected human dose or saline solution (control group). Animals are monitored, weighed on a daily basis, with blood chemistry (complete blood cell count, hematocrit, hemoglobin, serum creatinine, and alanine aminotransferease) and necropsy performed after 14 days to discern potential differences between the treated and control groups[292]. We have an in-house Investigational Drug Program at the BCCA that is well-equipped to perform biodistribution and toxicology studies under GLP conditions. Pending optimization to prolong bioavailability to increase overall uptake and contrast, we believe that ^{68}Ga-DOTA-AEBSA discussed in Chapter 5 is an encouraging candidate for future clinical translation.

Bibliography

1. Weissleder R, Mahmood U. Molecular imaging. Radiology 2001;219(2): 316-33.
2. Cherry SR, Sorenson JA, Phelps ME. Physics in nuclear medicine. 4th ed. Philadelphia: Elsevier/Saunders, 2012.
3. Gambhir SS. Molecular imaging of cancer with positron emission tomography. Nat Rev Cancer 2002;2(9): 683-93.
4. Fani M, Maecke HR. Radiopharmaceutical development of radiolabelled peptides. Eur J Nucl Med Mol Imaging 2012;39 Suppl 1: S11-30.
5. Holland JP, Williamson MJ, Lewis JS. Unconventional nuclides for radiopharmaceuticals. Mol Imaging 2010;9(1): 1-20.
6. Seo Y, Mari C, Hasegawa BH. Technological development and advances in single-photon emission computed tomography/computed tomography. Semin Nucl Med 2008;38(3): 177-98.
7. Van Noorden R. Radioisotopes: The medical testing crisis. Nature 2013;504(7479): 202-4.
8. Iagaru A, Young P, Mittra E, Dick DW, Herfkens R, Gambhir SS. Pilot prospective evaluation of 99mTc-MDP scintigraphy, 18F NaF PET/CT, 18F FDG PET/CT and whole-body MRI for detection of skeletal metastases. Clin Nucl Med 2013;38(7): e290-6.
9. Subramanian G, McAfee JG, Blair RJ, Kallfelz FA, Thomas FD. Technetium-99m-methylene diphosphonate--a superior agent for skeletal imaging: comparison with other technetium complexes. J Nucl Med 1975;16(8): 744-55.
10. Zaret BL, Rigo P, Wackers FJ, et al. Myocardial perfusion imaging with 99mTc tetrofosmin. Comparison to 201Tl imaging and coronary angiography in a phase III multicenter trial. Tetrofosmin International Trial Study Group. Circulation 1995;91(2): 313-9.
11. Medrano R, Lowry RW, Young JB, et al. Assessment of myocardial viability with 99mTc sestamibi in patients undergoing cardiac transplantation. A scintigraphic/pathological study. Circulation 1996;94(5): 1010-7.
12. Baggish AL, Boucher CA. Radiopharmaceutical agents for myocardial perfusion imaging. Circulation 2008;118(16): 1668-74.
13. Nakamura K, Tukatani Y, Kubo A, et al. The behavior of 99mTc-hexamethylpropyleneamineoxime (99mTc-HMPAO) in blood and brain. Eur J Nucl Med 1989;15(2): 100-7.
14. DuBois SG, Matthay KK. Radiolabeled metaiodobenzylguanidine for the treatment of neuroblastoma. Nucl Med Biol 2008;35 Suppl 1: S35-48.
15. Carrasquillo JA, Chen CC. 131 I-MIBG Therapy. In: Strauss HW, Mariani G, Volterrani D, Larson SM, editors. Nuclear Oncology Pathophysiology and Clinical Applications. New York: Springer 2013:691-714.
16. Buck AK, Herrmann K, Stargardt T, Dechow T, Krause BJ, Schreyogg J. Economic evaluation of PET and PET/CT in oncology: evidence and methodologic approaches. J Nucl Med Technol 2010;38(1): 6-17.
17. Hillner BE, Siegel BA, Liu D, et al. Impact of positron emission tomography/computed tomography and positron emission tomography (PET) alone on expected management of patients with cancer: initial results from the National Oncologic PET Registry. J Clin Oncol 2008;26(13): 2155-61.

18. Garland S, Morrison A. Publicly Funded Uses of PET Scans in Canada. Environmental Scan. Ottawa, Canada: Canadian Agency for Drugs and Technologies in Health, 2015:1-11.
19. Kim JW, Dang CV. Cancer's molecular sweet tooth and the Warburg effect. Cancer Res 2006;66(18): 8927-30.
20. Nabi HA, Zubeldia JM. Clinical applications of (18)F-FDG in oncology. J Nucl Med Technol 2002;30(1): 3-9; quiz 10-1.
21. Pauwels EK, Sturm EJ, Bombardieri E, Cleton FJ, Stokkel MP. Positron-emission tomography with [18F]fluorodeoxyglucose. Part I. Biochemical uptake mechanism and its implication for clinical studies. J Cancer Res Clin Oncol 2000;126(10): 549-59.
22. Griffeth LK. Use of PET/CT scanning in cancer patients: technical and practical considerations. Proc (Bayl Univ Med Cent) 2005;18(4): 321-30.
23. Bauwens M, Wierts R, van Royen B, et al. Molecular imaging of brown adipose tissue in health and disease. Eur J Nucl Med Mol Imaging 2014;41(4): 776-91.
24. Sobic-Saranovic D, Artiko V, Obradovic V. FDG PET imaging in sarcoidosis. Semin Nucl Med 2013;43(6): 404-11.
25. Vorster M, Sathekge MM, Bomanji J. Advances in imaging of tuberculosis: the role of (1)(8)F-FDG PET and PET/CT. Curr Opin Pulm Med 2014;20(3): 287-93.
26. Glaudemans AW, de Vries EF, Galli F, Dierckx RA, Slart RH, Signore A. The use of (18)F-FDG-PET/CT for diagnosis and treatment monitoring of inflammatory and infectious diseases. Clin Dev Immunol 2013;2013: 623036.
27. Rohren EM, Turkington TG, Coleman RE. Clinical applications of PET in oncology. Radiology 2004;231(2): 305-32.
28. Mansour JC, Schwarz RE. Molecular mechanisms for individualized cancer care. J Am Coll Surg 2008;207(2): 250-8.
29. Harris TJ, McCormick F. The molecular pathology of cancer. Nat Rev Clin Oncol 2010;7(5): 251-65.
30. Hanahan D, Weinberg RA. The hallmarks of cancer. Cell 2000;100(1): 57-70.
31. Hanahan D, Weinberg RA. Hallmarks of cancer: the next generation. Cell 2011;144(5): 646-74.
32. Welcsh PL, King MC. BRCA1 and BRCA2 and the genetics of breast and ovarian cancer. Hum Mol Genet 2001;10(7): 705-13.
33. Meijers-Heijboer H, Brekelmans CT, Menke-Pluymers M, et al. Use of genetic testing and prophylactic mastectomy and oophorectomy in women with breast or ovarian cancer from families with a BRCA1 or BRCA2 mutation. J Clin Oncol 2003;21(9): 1675-81.
34. Sawyers C. Targeted cancer therapy. Nature 2004;432(7015): 294-7.
35. Cohen MH, Williams G, Johnson JR, et al. Approval summary for imatinib mesylate capsules in the treatment of chronic myelogenous leukemia. Clin Cancer Res 2002;8(5): 935-42.
36. Johnson JR, Bross P, Cohen M, et al. Approval summary: imatinib mesylate capsules for treatment of adult patients with newly diagnosed philadelphia chromosome-positive chronic myelogenous leukemia in chronic phase. Clin Cancer Res 2003;9(6): 1972-9.
37. Druker BJ. Imatinib and chronic myeloid leukemia: validating the promise of molecularly targeted therapy. Eur J Cancer 2002;38 Suppl 5: S70-6.
38. Neal JW, Sledge GW. Decade in review-targeted therapy: successes, toxicities and challenges in solid tumours. Nat Rev Clin Oncol 2014;11(11): 627-8.

39. Medical imaging in personalised medicine: a white paper of the research committee of the European Society of Radiology (ESR). Insights Imaging 2015;6(2): 141-55.
40. Gupta N, Price PM, Aboagye EO. PET for in vivo pharmacokinetic and pharmacodynamic measurements. Eur J Cancer 2002;38(16): 2094-107.
41. Quail DF, Joyce JA. Microenvironmental regulation of tumor progression and metastasis. Nat Med 2013;19(11): 1423-37.
42. Balkwill FR, Capasso M, Hagemann T. The tumor microenvironment at a glance. J Cell Sci 2012;125(Pt 23): 5591-6.
43. Mbeunkui F, Johann DJ, Jr. Cancer and the tumor microenvironment: a review of an essential relationship. Cancer Chemother Pharmacol 2009;63(4): 571-82.
44. Parks SK, Chiche J, Pouyssegur J. Disrupting proton dynamics and energy metabolism for cancer therapy. Nat Rev Cancer 2013;13(9): 611-23.
45. Blagosklonny MV. Antiangiogenic therapy and tumor progression. Cancer Cell 2004;5(1): 13-7.
46. Walsh JC, Lebedev A, Aten E, Madsen K, Marciano L, Kolb HC. The clinical importance of assessing tumor hypoxia: relationship of tumor hypoxia to prognosis and therapeutic opportunities. Antioxid Redox Signal 2014;21(10): 1516-54.
47. Bennewith KL, Dedhar S. Targeting hypoxic tumour cells to overcome metastasis. BMC Cancer 2011;11: 504.
48. Rockwell S, Dobrucki IT, Kim EY, Marrison ST, Vu VT. Hypoxia and radiation therapy: past history, ongoing research, and future promise. Curr Mol Med 2009;9(4): 442-58.
49. Yoshimura M, Itasaka S, Harada H, Hiraoka M. Microenvironment and radiation therapy. Biomed Res Int 2013;2013: 685308.
50. Grimes DR, Partridge M. A mechanistic investigation of the oxygen fixation hypothesis and oxygen enhancement ratio. Biomed Phys Eng Express 2015;1(4): 045209.
51. Bertout JA, Patel SA, Simon MC. The impact of O2 availability on human cancer. Nat Rev Cancer 2008;8(12): 967-75.
52. Gray LH, Conger AD, Ebert M, Hornsey S, Scott OC. The concentration of oxygen dissolved in tissues at the time of irradiation as a factor in radiotherapy. Br J Radiol 1953;26(312): 638-48.
53. Minchinton AI, Tannock IF. Drug penetration in solid tumours. Nat Rev Cancer 2006;6(8): 583-92.
54. Rohwer N, Cramer T. Hypoxia-mediated drug resistance: novel insights on the functional interaction of HIFs and cell death pathways. Drug Resist Updat 2011;14(3): 191-201.
55. Krohn KA, Link JM, Mason RP. Molecular imaging of hypoxia. J Nucl Med 2008;49 Suppl 2: 129S-48S.
56. McDonald PC, Dedhar S. Carbonic anhydrase IX (CAIX) as a mediator of hypoxia-induced stress response in cancer cells. Subcell Biochem 2014;75: 255-69.
57. Wilson WR, Hay MP. Targeting hypoxia in cancer therapy. Nat Rev Cancer 2011;11(6): 393-410.
58. Hockel M, Knoop C, Schlenger K, et al. Intratumoral pO2 predicts survival in advanced cancer of the uterine cervix. Radiother Oncol 1993;26(1): 45-50.
59. Fleming IN, Manavaki R, Blower PJ, et al. Imaging tumour hypoxia with positron emission tomography. Br J Cancer 2015;112(2): 238-50.
60. Mees G, Dierckx R, Vangestel C, Van de Wiele C. Molecular imaging of hypoxia with radiolabelled agents. Eur J Nucl Med Mol Imaging 2009;36(10): 1674-86.

61. Rajendran JG, Wilson DC, Conrad EU, et al. [(18)F]FMISO and [(18)F]FDG PET imaging in soft tissue sarcomas: correlation of hypoxia, metabolism and VEGF expression. Eur J Nucl Med Mol Imaging 2003;30(5): 695-704.
62. Harris AL. Hypoxia--a key regulatory factor in tumour growth. Nat Rev Cancer 2002;2(1): 38-47.
63. Carroll VA, Ashcroft M. Targeting the molecular basis for tumour hypoxia. Expert Rev Mol Med 2005;7(6): 1-16.
64. Potter C, Harris AL. Hypoxia inducible carbonic anhydrase IX, marker of tumour hypoxia, survival pathway and therapy target. Cell Cycle 2004;3(2): 164-7.
65. Pastorekova S, Zavadova Z, Kostal M, Babusikova O, Zavada J. A novel quasi-viral agent, MaTu, is a two-component system. Virology 1992;187(2): 620-6.
66. Pastorek J, Pastorekova S, Callebaut I, et al. Cloning and characterization of MN, a human tumor-associated protein with a domain homologous to carbonic anhydrase and a putative helix-loop-helix DNA binding segment. Oncogene 1994;9(10): 2877-88.
67. Alterio V, Di Fiore A, D'Ambrosio K, Supuran CT, De Simone G. Multiple binding modes of inhibitors to carbonic anhydrases: how to design specific drugs targeting 15 different isoforms? Chem Rev 2012;112(8): 4421-68.
68. Rafajova M, Zatovicova M, Kettmann R, Pastorek J, Pastorekova S. Induction by hypoxia combined with low glucose or low bicarbonate and high posttranslational stability upon reoxygenation contribute to carbonic anhydrase IX expression in cancer cells. Int J Oncol 2004;24(4): 995-1004.
69. Moroz E, Carlin S, Dyomina K, et al. Real-time imaging of HIF-1alpha stabilization and degradation. PLoS One 2009;4(4): e5077.
70. Kaluz S, Kaluzova M, Liao SY, Lerman M, Stanbridge EJ. Transcriptional control of the tumor- and hypoxia-marker carbonic anhydrase 9: A one transcription factor (HIF-1) show? Biochim Biophys Acta 2009;1795(2): 162-72.
71. He F, Deng X, Wen B, et al. Noninvasive molecular imaging of hypoxia in human xenografts: comparing hypoxia-induced gene expression with endogenous and exogenous hypoxia markers. Cancer Res 2008;68(20): 8597-606.
72. Olive PL, Aquino-Parsons C, MacPhail SH, et al. Carbonic anhydrase 9 as an endogenous marker for hypoxic cells in cervical cancer. Cancer Res 2001;61(24): 8924-9.
73. Morris MR, Hughes DJ, Tian YM, et al. Mutation analysis of hypoxia-inducible factors HIF1A and HIF2A in renal cell carcinoma. Anticancer Res 2009;29(11): 4337-43.
74. Li Z, Bao S, Wu Q, et al. Hypoxia-inducible factors regulate tumorigenic capacity of glioma stem cells. Cancer Cell 2009;15(6): 501-13.
75. Holmquist-Mengelbier L, Fredlund E, Lofstedt T, et al. Recruitment of HIF-1alpha and HIF-2alpha to common target genes is differentially regulated in neuroblastoma: HIF-2alpha promotes an aggressive phenotype. Cancer Cell 2006;10(5): 413-23.
76. Pastorekova S, Barathova M, Kopacek J, Pastorek J. Carbonic Anhydrase Inhibitors Targeting Cancer: Therapeutic, Immunologic, and Diagnostic Tools Targeting Isoforms IX and XII. In: Supuran CT, Winum JY, editors. Drug Design of Zinc-Enzyme Inhibitors: Functional, Structural, and Disease Applications. Hoboken, NJ, USA: John Wiley & Sons, Inc., 2009:193-222.
77. Alterio V, Hilvo M, Di Fiore A, et al. Crystal structure of the catalytic domain of the tumor-associated human carbonic anhydrase IX. Proc Natl Acad Sci U S A 2009;106(38): 16233-8.

78. Brahimi-Horn MC, Pouyssegur J. Hypoxia in cancer cell metabolism and pH regulation. Oxygen Sensing and Hypoxia-Induced Responses 2007;43: 165-78.
79. Boyer MJ, Tannock IF. Regulation of Intracellular Ph in Tumor-Cell Lines - Influence of Microenvironmental Conditions. Cancer Research 1992;52(16): 4441-47.
80. Parks SK, Chiche J, Pouyssegur J. pH Control Mechanisms of Tumor Survival and Growth. Journal of Cellular Physiology 2011;226(2): 299-308.
81. Hilvo M, Baranauskiene L, Salzano AM, et al. Biochemical characterization of CA IX, one of the most active carbonic anhydrase isozymes. J Biol Chem 2008;283(41): 27799-809.
82. Bartosova M, Parkkila S, Pohlodek K, et al. Expression of carbonic anhydrase IX in breast is associated with malignant tissues and is related to overexpression of c-erbB2. J Pathol 2002;197(3): 314-21.
83. Swietach P, Wigfield S, Cobden P, Supuran CT, Harris AL, Vaughan-Jones RD. Tumor-associated carbonic anhydrase 9 spatially coordinates intracellular pH in three-dimensional multicellular growths. J Biol Chem 2008;283(29): 20473-83.
84. Swietach P, Wigfield S, Supuran CT, Harris AL, Vaughan-Jones RD. Cancer-associated, hypoxia-inducible carbonic anhydrase IX facilitates CO2 diffusion. BJU Int 2008;101 Suppl 4: 22-4.
85. Lou Y, McDonald PC, Oloumi A, et al. Targeting tumor hypoxia: suppression of breast tumor growth and metastasis by novel carbonic anhydrase IX inhibitors. Cancer Res 2011;71(9): 3364-76.
86. Svastova E, Zilka N, Zat'ovicova M, et al. Carbonic anhydrase IX reduces E-cadherin-mediated adhesion of MDCK cells via interaction with beta-catenin. Exp Cell Res 2003;290(2): 332-45.
87. Shin HJ, Rho SB, Jung DC, Han IO, Oh ES, Kim JY. Carbonic anhydrase IX (CA9) modulates tumor-associated cell migration and invasion. J Cell Sci 2011;124(Pt 7): 1077-87.
88. Overall CM, Kleifeld O. Tumour microenvironment - opinion: validating matrix metalloproteinases as drug targets and anti-targets for cancer therapy. Nat Rev Cancer 2006;6(3): 227-39.
89. Kessenbrock K, Plaks V, Werb Z. Matrix metalloproteinases: regulators of the tumor microenvironment. Cell 2010;141(1): 52-67.
90. Hulikova A, Zatovicova M, Svastova E, et al. Intact intracellular tail is critical for proper functioning of the tumor-associated, hypoxia-regulated carbonic anhydrase IX. FEBS Lett 2009;583(22): 3563-8.
91. Ditte P, Dequiedt F, Svastova E, et al. Phosphorylation of carbonic anhydrase IX controls its ability to mediate extracellular acidification in hypoxic tumors. Cancer Res 2011;71(24): 7558-67.
92. Dorai T, Sawczuk IS, Pastorek J, Wiernik PH, Dutcher JP. The role of carbonic anhydrase IX overexpression in kidney cancer. Eur J Cancer 2005;41(18): 2935-47.
93. Zatovicova M, Sedlakova O, Svastova E, et al. Ectodomain shedding of the hypoxia-induced carbonic anhydrase IX is a metalloprotease-dependent process regulated by TACE/ADAM17. Br J Cancer 2005;93(11): 1267-76.
94. Zavada J, Zavadova Z, Zat'ovicova M, Hyrsl L, Kawaciuk I. Soluble form of carbonic anhydrase IX (CA IX) in the serum and urine of renal carcinoma patients. Br J Cancer 2003;89(6): 1067-71.

95. Kock L, Mahner S, Choschzick M, et al. Serum carbonic anhydrase IX and its prognostic relevance in vulvar cancer. Int J Gynecol Cancer 2011;21(1): 141-8.
96. Brown-Glaberman U, Marron M, Chalasani P, et al. Circulating Carbonic Anhydrase IX and Antiangiogenic Therapy in Breast Cancer. Dis Markers 2016;2016: 9810383.
97. Vidlickova I, Dequiedt F, Jelenska L, et al. Apoptosis-induced ectodomain shedding of hypoxia-regulated carbonic anhydrase IX from tumor cells: a double-edged response to chemotherapy. BMC Cancer 2016;16(1): 239.
98. Srinivasarao M, Galliford CV, Low PS. Principles in the design of ligand-targeted cancer therapeutics and imaging agents. Nat Rev Drug Discov 2015;14(3): 203-19.
99. Saarnio J, Parkkila S, Parkkila AK, et al. Immunohistochemistry of carbonic anhydrase isozyme IX (MN/CA IX) in human gut reveals polarized expression in the epithelial cells with the highest proliferative capacity. J Histochem Cytochem 1998;46(4): 497-504.
100. Karhumaa P, Kaunisto K, Parkkila S, et al. Expression of the transmembrane carbonic anhydrases, CA IX and CA XII, in the human male excurrent ducts. Mol Hum Reprod 2001;7(7): 611-6.
101. Kivela AJ, Parkkila S, Saarnio J, et al. Expression of transmembrane carbonic anhydrase isoenzymes IX and XII in normal human pancreas and pancreatic tumours. Histochem Cell Biol 2000;114(3): 197-204.
102. Tan EY, Yan M, Campo L, et al. The key hypoxia regulated gene CAIX is upregulated in basal-like breast tumours and is associated with resistance to chemotherapy. Br J Cancer 2009;100(2): 405-11.
103. Ilie M, Mazure NM, Hofman V, et al. High levels of carbonic anhydrase IX in tumour tissue and plasma are biomarkers of poor prognostic in patients with non-small cell lung cancer. Br J Cancer 2010;102(11): 1627-35.
104. Kim SJ, Rabbani ZN, Vollmer RT, et al. Carbonic anhydrase IX in early-stage non-small cell lung cancer. Clin Cancer Res 2004;10(23): 7925-33.
105. Korkeila E, Talvinen K, Jaakkola PM, et al. Expression of carbonic anhydrase IX suggests poor outcome in rectal cancer. Br J Cancer 2009;100(6): 874-80.
106. Hutchison GJ, Valentine HR, Loncaster JA, et al. Hypoxia-inducible factor 1alpha expression as an intrinsic marker of hypoxia: correlation with tumor oxygen, pimonidazole measurements, and outcome in locally advanced carcinoma of the cervix. Clin Cancer Res 2004;10(24): 8405-12.
107. Kim JY, Shin HJ, Kim TH, et al. Tumor-associated carbonic anhydrases are linked to metastases in primary cervical cancer. J Cancer Res Clin Oncol 2006;132(5): 302-8.
108. Choschzick M, Oosterwijk E, Muller V, et al. Overexpression of carbonic anhydrase IX (CAIX) is an independent unfavorable prognostic marker in endometrioid ovarian cancer. Virchows Arch 2011;459(2): 193-200.
109. Beasley NJ, Wykoff CC, Watson PH, et al. Carbonic anhydrase IX, an endogenous hypoxia marker, expression in head and neck squamous cell carcinoma and its relationship to hypoxia, necrosis, and microvessel density. Cancer Res 2001;61(13): 5262-7.
110. Hoogsteen IJ, Marres HA, Wijffels KI, et al. Colocalization of carbonic anhydrase 9 expression and cell proliferation in human head and neck squamous cell carcinoma. Clin Cancer Res 2005;11(1): 97-106.
111. Klatte T, Seligson DB, Rao JY, et al. Carbonic anhydrase IX in bladder cancer: a diagnostic, prognostic, and therapeutic molecular marker. Cancer 2009;115(7): 1448-58.

112. Bui MH, Seligson D, Han KR, et al. Carbonic anhydrase IX is an independent predictor of survival in advanced renal clear cell carcinoma: implications for prognosis and therapy. Clin Cancer Res 2003;9(2): 802-11.
113. Stillebroer AB, Mulders PF, Boerman OC, Oyen WJ, Oosterwijk E. Carbonic anhydrase IX in renal cell carcinoma: implications for prognosis, diagnosis, and therapy. Eur Urol 2010;58(1): 75-83.
114. Hussain SA, Ganesan R, Reynolds G, et al. Hypoxia-regulated carbonic anhydrase IX expression is associated with poor survival in patients with invasive breast cancer. Br J Cancer 2007;96(1): 104-9.
115. Haapasalo JA, Nordfors KM, Hilvo M, et al. Expression of carbonic anhydrase IX in astrocytic tumors predicts poor prognosis. Clin Cancer Res 2006;12(2): 473-7.
116. Fogh J, Fogh JM, Orfeo T. One hundred and twenty-seven cultured human tumor cell lines producing tumors in nude mice. J Natl Cancer Inst 1977;59(1): 221-6.
117. Ebert T, Bander NH, Finstad CL, Ramsawak RD, Old LJ. Establishment and characterization of human renal cancer and normal kidney cell lines. Cancer Res 1990;50(17): 5531-6.
118. Chrastina A, Zavada J, Parkkila S, et al. Biodistribution and pharmacokinetics of 125I-labeled monoclonal antibody M75 specific for carbonic anhydrase IX, an intrinsic marker of hypoxia, in nude mice xenografted with human colorectal carcinoma. Int J Cancer 2003;105(6): 873-81.
119. Ivanov SV, Kuzmin I, Wei MH, et al. Down-regulation of transmembrane carbonic anhydrases in renal cell carcinoma cell lines by wild-type von Hippel-Lindau transgenes. Proc Natl Acad Sci U S A 1998;95(21): 12596-601.
120. Liu Z, Smyth FE, Renner C, Lee FT, Oosterwijk E, Scott AM. Anti-renal cell carcinoma chimeric antibody G250: cytokine enhancement of in vitro antibody-dependent cellular cytotoxicity. Cancer Immunol Immunother 2002;51(3): 171-7.
121. Shuin T, Kondo K, Torigoe S, et al. Frequent somatic mutations and loss of heterozygosity of the von Hippel-Lindau tumor suppressor gene in primary human renal cell carcinomas. Cancer Res 1994;54(11): 2852-5.
122. Herman JG, Latif F, Weng Y, et al. Silencing of the VHL tumor-suppressor gene by DNA methylation in renal carcinoma. Proc Natl Acad Sci U S A 1994;91(21): 9700-4.
123. Scott AM, Allison JP, Wolchok JD. Monoclonal antibodies in cancer therapy. Cancer Immun 2012;12: 14.
124. Scott AM, Wolchok JD, Old LJ. Antibody therapy of cancer. Nat Rev Cancer 2012;12(4): 278-87.
125. Chrastina A, Pastorekova S, Pastorek J. Immunotargeting of human cervical carcinoma xenograft expressing CA IX tumor-associated antigen by 125I-labeled M75 monoclonal antibody. Neoplasma 2003;50(1): 13-21.
126. Wind TC, Messenger MP, Thompson D, Selby PJ, Banks RE. Measuring carbonic anhydrase IX as a hypoxia biomarker: differences in concentrations in serum and plasma using a commercial enzyme-linked immunosorbent assay due to influences of metal ions. Ann Clin Biochem 2011;48(Pt 2): 112-20.
127. Divgi CR, Uzzo RG, Gatsonis C, et al. Positron emission tomography/computed tomography identification of clear cell renal cell carcinoma: results from the REDECT trial. J Clin Oncol 2013;31(2): 187-94.

128. Stillebroer AB, Franssen GM, Mulders PF, et al. ImmunoPET imaging of renal cell carcinoma with (124)I- and (89)Zr-labeled anti-CAIX monoclonal antibody cG250 in mice. Cancer Biother Radiopharm 2013;28(7): 510-5.
129. Stillebroer AB, Zegers CM, Boerman OC, et al. Dosimetric analysis of 177Lu-cG250 radioimmunotherapy in renal cell carcinoma patients: correlation with myelotoxicity and pretherapeutic absorbed dose predictions based on 111In-cG250 imaging. J Nucl Med 2012;53(1): 82-9.
130. Firer MA, Gellerman G. Targeted drug delivery for cancer therapy: the other side of antibodies. J Hematol Oncol 2012;5: 70.
131. Supuran CT. Carbonic anhydrases: novel therapeutic applications for inhibitors and activators. Nat Rev Drug Discov 2008;7(2): 168-81.
132. Carta F, Maresca A, Scozzafava A, Supuran CT. Novel coumarins and 2-thioxo-coumarins as inhibitors of the tumor-associated carbonic anhydrases IX and XII. Bioorg Med Chem 2012;20(7): 2266-73.
133. Apte SD, Chin FT, Graves EE. Synthesis of a New PET Radiotracer Targeting Carbonic Anhydrase IX. Journal of Labelled Compounds and Radiopharmaceuticals 2009;52(S1): S408.
134. Lu G, Hillier SM, Maresca KP, et al. Synthesis and SAR of novel Re/99mTc-labeled benzenesulfonamide carbonic anhydrase IX inhibitors for molecular imaging of tumor hypoxia. J Med Chem 2013;56(2): 510-20.
135. Akurathi V, Dubois L, Celen S, et al. Development and biological evaluation of (9)(9)mTc-sulfonamide derivatives for in vivo visualization of CA IX as surrogate tumor hypoxia markers. Eur J Med Chem 2014;71: 374-84.
136. Akurathi V, Dubois L, Lieuwes NG, et al. Synthesis and biological evaluation of a 99mTc-labelled sulfonamide conjugate for in vivo visualization of carbonic anhydrase IX expression in tumor hypoxia. Nucl Med Biol 2010;37(5): 557-64.
137. Turkbey B, Lindenberg ML, Adler S, et al. PET/CT imaging of renal cell carcinoma with (18)F-VM4-037: a phase II pilot study. Abdom Radiol (NY) 2016;41(1): 109-18.
138. Peeters SG, Dubois L, Lieuwes NG, et al. [F]VM4-037 MicroPET Imaging and Biodistribution of Two In Vivo CAIX-Expressing Tumor Models. Mol Imaging Biol 2015.
139. Krall N, Pretto F, Mattarella M, Muller C, Neri D. A technetium 99m-labeled ligand of carbonic anhydrase IX selectively targets renal cell carcinoma in vivo. J Nucl Med 2016.
140. Lee S, Xie J, Chen X. Peptide-based probes for targeted molecular imaging. Biochemistry 2010;49(7): 1364-76.
141. Rolleman EJ, Melis M, Valkema R, Boerman OC, Krenning EP, de Jong M. Kidney protection during peptide receptor radionuclide therapy with somatostatin analogues. Eur J Nucl Med Mol Imaging 2010;37(5): 1018-31.
142. Vegt E, Melis M, Eek A, et al. Renal uptake of different radiolabelled peptides is mediated by megalin: SPECT and biodistribution studies in megalin-deficient mice. Eur J Nucl Med Mol Imaging 2011;38(4): 623-32.
143. Vegt E, de Jong M, Wetzels JF, et al. Renal toxicity of radiolabeled peptides and antibody fragments: mechanisms, impact on radionuclide therapy, and strategies for prevention. J Nucl Med 2010;51(7): 1049-58.
144. Askoxylakis V, Garcia-Boy R, Rana S, et al. A new peptide ligand for targeting human carbonic anhydrase IX, identified through the phage display technology. PLoS One 2010;5(12): e15962.

145. Rana S, Nissen F, Marr A, et al. Optimization of a novel peptide ligand targeting human carbonic anhydrase IX. PLoS One 2012;7(5): e38279.
146. Rana S, Nissen F, Lindner T, et al. Screening of a novel peptide targeting the proteoglycan-like region of human carbonic anhydrase IX. Mol Imaging 2013;12(8).
147. Lofblom J, Feldwisch J, Tolmachev V, Carlsson J, Stahl S, Frejd FY. Affibody molecules: engineered proteins for therapeutic, diagnostic and biotechnological applications. FEBS Lett 2010;584(12): 2670-80.
148. Tolmachev V, Orlova A, Nilsson FY, Feldwisch J, Wennborg A, Abrahmsen L. Affibody molecules: potential for in vivo imaging of molecular targets for cancer therapy. Expert Opin Biol Ther 2007;7(4): 555-68.
149. Orlova A, Magnusson M, Eriksson TL, et al. Tumor imaging using a picomolar affinity HER2 binding affibody molecule. Cancer Res 2006;66(8): 4339-48.
150. Tolmachev V, Friedman M, Sandstrom M, et al. Affibody molecules for epidermal growth factor receptor targeting in vivo: aspects of dimerization and labeling chemistry. J Nucl Med 2009;50(2): 274-83.
151. Orlova A, Hofstrom C, Strand J, et al. [99mTc(CO)3]+-(HE)3-ZIGF1R:4551, a new Affibody conjugate for visualization of insulin-like growth factor-1 receptor expression in malignant tumours. Eur J Nucl Med Mol Imaging 2013;40(3): 439-49.
152. Tolmachev V, Varasteh Z, Honarvar H, et al. Imaging of platelet-derived growth factor receptor beta expression in glioblastoma xenografts using affibody molecule 111In-DOTA-Z09591. J Nucl Med 2014;55(2): 294-300.
153. Orlova A, Malm M, Rosestedt M, et al. Imaging of HER3-expressing xenografts in mice using a (99m)Tc(CO) 3-HEHEHE-Z HER3:08699 affibody molecule. Eur J Nucl Med Mol Imaging 2014;41(7): 1450-9.
154. Honarvar H, Garousi J, Gunneriusson E, et al. Imaging of CAIX-expressing xenografts in vivo using 99mTc-HEHEHE-ZCAIX:1 affibody molecule. Int J Oncol 2015;46(2): 513-20.
155. Altai M, Perols A, Tsourma M, et al. Feasibility of Affibody-Based Bioorthogonal Chemistry-Mediated Radionuclide Pretargeting. J Nucl Med 2016;57(3): 431-6.
156. Honarvar H, Westerlund K, Altai M, et al. Feasibility of Affibody Molecule-Based PNA-Mediated Radionuclide Pretargeting of Malignant Tumors. Theranostics 2016;6(1): 93-103.
157. Luker GD, Luker KE. Optical imaging: current applications and future directions. J Nucl Med 2008;49(1): 1-4.
158. van Leeuwen FW, de Jong M. Molecular imaging: the emerging role of optical imaging in nuclear medicine. Eur J Nucl Med Mol Imaging 2014;41(11): 2150-3.
159. Muselaers CH, Stillebroer AB, Rijpkema M, et al. Optical Imaging of Renal Cell Carcinoma with Anti-Carbonic Anhydrase IX Monoclonal Antibody Girentuximab. J Nucl Med 2014;55(6): 1035-40.
160. Tafreshi NK, Bui MM, Bishop K, et al. Noninvasive detection of breast cancer lymph node metastasis using carbonic anhydrases IX and XII targeted imaging probes. Clin Cancer Res 2012;18(1): 207-19.
161. van Brussel AS, Adams A, Oliveira S, et al. Hypoxia-Targeting Fluorescent Nanobodies for Optical Molecular Imaging of Pre-Invasive Breast Cancer. Mol Imaging Biol 2015.
162. Groves K, Bao B, Zhang J, et al. Synthesis and evaluation of near-infrared fluorescent sulfonamide derivatives for imaging of hypoxia-induced carbonic anhydrase IX expression in tumors. Bioorg Med Chem Lett 2012;22(1): 653-7.

163. Bao B, Groves K, Zhang J, et al. In vivo imaging and quantification of carbonic anhydrase IX expression as an endogenous biomarker of tumor hypoxia. PLoS One 2012;7(11): e50860.
164. Wichert M, Krall N, Decurtins W, et al. Dual-display of small molecules enables the discovery of ligand pairs and facilitates affinity maturation. Nat Chem 2015;7(3): 241-9.
165. Lv PC, Roy J, Putt KS, Low PS. Evaluation of a Carbonic Anhydrase IX-Targeted Near-Infrared Dye for Fluorescence-Guided Surgery of Hypoxic Tumors. Mol Pharm 2016.
166. Berger A. Magnetic resonance imaging. BMJ 2002;324(7328): 35.
167. Gallagher FA. An introduction to functional and molecular imaging with MRI. Clin Radiol 2010;65(7): 557-66.
168. Kurhanewicz J, Vigneron DB, Brindle K, et al. Analysis of cancer metabolism by imaging hyperpolarized nuclei: prospects for translation to clinical research. Neoplasia 2011;13(2): 81-97.
169. Gallagher FA, Sladen H, Kettunen MI, et al. Carbonic Anhydrase Activity Monitored In Vivo by Hyperpolarized 13C-Magnetic Resonance Spectroscopy Demonstrates Its Importance for pH Regulation in Tumors. Cancer Res 2015;75(19): 4109-18.
170. Chen W, Han Y, Qian Y, Tang J, Hu H, Shen Y. Preparation and Imaging Study of Tumor-targeting MRI Contrast Agent Based on Fe3O4 Nanoparticles. Chem Lett 2015;44(12): 1771-73.
171. Rami M, Montero JL, Dubois L, et al. Carbonic anhydrase inhibitors: Gd(III) complexes of DOTA- and TETA-sulfonamide conjugates targeting the tumor associated carbonic anhydrase isozymes IX and XII. New J Chem 2010;34: 2139-44.
172. Belldegrun AS, Chamie K, Klopfer P, et al. ARISER: A randomized double blind phase III study to evaluate adjuvant cG250 treatment versus placebo in patients with high risk ccRCC - Results and implications for adjuvant clinical trials. ASCO Annual Meeting 2013, 2013:Abstract 4507.
173. Muselaers CH, Boers-Sonderen MJ, van Oostenbrugge TJ, et al. Phase 2 Study of Lutetium 177-Labeled Anti-Carbonic Anhydrase IX Monoclonal Antibody Girentuximab in Patients with Advanced Renal Cell Carcinoma. Eur Urol 2015.
174. Petrul HM, Schatz CA, Kopitz CC, et al. Therapeutic mechanism and efficacy of the antibody-drug conjugate BAY 79-4620 targeting human carbonic anhydrase 9. Mol Cancer Ther 2012;11(2): 340-9.
175. BAY 79-4620/12671 Clinical Study Report Bayer HealthCare Pharmaceuticals, Inc., 2014.
176. Supuran CT, Winum JY. Designing carbonic anhydrase inhibitors for the treatment of breast cancer. Expert Opin Drug Discov 2015;10(6): 591-7.
177. Dubois L, Peeters SG, van Kuijk SJ, et al. Targeting carbonic anhydrase IX by nitroimidazole based sulfamides enhances the therapeutic effect of tumor irradiation: a new concept of dual targeting drugs. Radiother Oncol 2013;108(3): 523-8.
178. Pacchiano F, Carta F, McDonald PC, et al. Ureido-substituted benzenesulfonamides potently inhibit carbonic anhydrase IX and show antimetastatic activity in a model of breast cancer metastasis. J Med Chem 2011;54(6): 1896-902.
179. Baker BR, Hurlbut JA. Irreversible enzyme inhibitors. 53. Proteolytic enzymes. XI. Inhibition of guinea pig complement by substituted phenoxyacetamides. J Med Chem 1969;12(3): 415-9.
180. Wilson AA, Dasilva JN, Houle S. Synthesis of two radiofluorinated cocaine analogues using distilled 2-[18F]fluoroethyl bromide. Appl Radiat Isot 1995;46(8): 765-70.

181. Gokce B, Gencer N, Arslan O, Turkoglu SA, Alper M, Kockar F. Evaluation of in vitro effects of some analgesic drugs on erythrocyte and recombinant carbonic anhydrase I and II. J Enzyme Inhib Med Chem 2012;27(1): 37-42.
182. Senturk M, Gulcin I, Beydemir S, Kufrevioglu OI, Supuran CT. In Vitro inhibition of human carbonic anhydrase I and II isozymes with natural phenolic compounds. Chem Biol Drug Des 2011;77(6): 494-9.
183. Guler OO, De Simone G, Supuran CT. Drug design studies of the novel antitumor targets carbonic anhydrase IX and XII. Curr Med Chem 2010;17(15): 1516-26.
184. Hendricks JA, Keliher EJ, Marinelli B, Reiner T, Weissleder R, Mazitschek R. In vivo PET imaging of histone deacetylases by 18F-suberoylanilide hydroxamic acid (18F-SAHA). J Med Chem 2011;54(15): 5576-82.
185. Kim KH, Isin EM, Yun CH, Kim DH, Guengerich FP. Kinetic deuterium isotope effects for 7-alkoxycoumarin O-dealkylation reactions catalyzed by human cytochromes P450 and in liver microsomes. Rate-limiting C-H bond breaking in cytochrome P450 1A2 substrate oxidation. FEBS J 2006;273(10): 2223-31.
186. Yamazaki H, Inoue K, Mimura M, Oda Y, Guengerich FP, Shimada T. 7-Ethoxycoumarin O-deethylation catalyzed by cytochromes P450 1A2 and 2E1 in human liver microsomes. Biochem Pharmacol 1996;51(3): 313-9.
187. Tewson TJ, Welch MJ. Preparation and preliminary biodistribution of "no carrier added" fluorine1-8 fluoroethanol. J Nucl Med 1980;21(6): 559-64.
188. Ling G, Gu J, Genter MB, Zhuo X, Ding X. Regulation of cytochrome P450 gene expression in the olfactory mucosa. Chem Biol Interact 2004;147(3): 247-58.
189. Pinard MA, Mahon B, McKenna R. Probing the surface of human carbonic anhydrase for clues towards the design of isoform specific inhibitors. Biomed Res Int 2015;2015: 453543.
190. McKenna R, Supuran CT. Carbonic anhydrase inhibitors drug design. Subcell Biochem 2014;75: 291-323.
191. Metayer B, Mingot A, Vullo D, Supuran CT, Thibaudeau S. New superacid synthesized (fluorinated) tertiary benzenesulfonamides acting as selective hCA IX inhibitors: toward a new mode of carbonic anhydrase inhibition by sulfonamides. Chem Commun (Camb) 2013;49(54): 6015-7.
192. Metayer B, Martin-Mingot A, Vullo D, Supuran CT, Thibaudeau S. Superacid synthesized tertiary benzenesulfonamides and benzofuzed sultams act as selective hCA IX inhibitors: toward understanding a new mode of inhibition by tertiary sulfonamides. Org Biomol Chem 2013;11(43): 7540-9.
193. Lin KS, Ding YS, Kim SW, Kil KE. Synthesis, enantiomeric resolution, F-18 labeling and biodistribution of reboxetine analogs: promising radioligands for imaging the norepinephrine transporter with positron emission tomography. Nucl Med Biol 2005;32(4): 415-22.
194. Yoshida Y, Sakakura Y, Aso N, Okada S, Tanabe Y. Practical and efficient methods for sulfonylation of alcohols using Ts(Ms)Cl/Et3N and catalytic Me3H·HCl as combined base: Promising alternative to traditional pyridine. Tetrahedron 1999;55(8): 2183-92.
195. Lipinski CA, Lombardo F, Dominy BW, Feeney PJ. Experimental and computational approaches to estimate solubility and permeability in drug discovery and development settings. Adv Drug Deliv Rev 2001;46(1-3): 3-26.

196. Pan J, Lau J, Mesak F, et al. Synthesis and evaluation of 18F-labeled carbonic anhydrase IX inhibitors for imaging with positron emission tomography. J Enzyme Inhib Med Chem 2014;29(2): 249-55.
197. Chiche J, Ilc K, Laferriere J, et al. Hypoxia-inducible carbonic anhydrase IX and XII promote tumor cell growth by counteracting acidosis through the regulation of the intracellular pH. Cancer Res 2009;69(1): 358-68.
198. Kniess T, Laube M, Bergmann R, et al. Radiosynthesis of a (1)(8)F-labeled 2,3-diarylsubstituted indole via McMurry coupling for functional characterization of cyclooxygenase-2 (COX-2) in vitro and in vivo. Bioorg Med Chem 2012;20(11): 3410-21.
199. Vasdev N, Dorff PN, O'Neil JP, Chin FT, Hanrahan S, VanBrocklin HF. Metabolic stability of 6,7-dialkoxy-4-(2-, 3- and 4-[18F]fluoroanilino)quinazolines, potential EGFR imaging probes. Bioorg Med Chem 2011;19(9): 2959-65.
200. Liu H, Liu S, Miao Z, et al. Development of 18F-labeled picolinamide probes for PET imaging of malignant melanoma. J Med Chem 2013;56(3): 895-901.
201. Cai LS, Shuiyu L, Pike VW. Chemistry with [18F]Fluoride Ion. Eur J Org Chem 2008;2008(17): 2853-73.
202. Liu Z, Pourghiasian M, Radtke MA, et al. An organotrifluoroborate for broadly applicable one-step (18) f-labeling. Angew Chem Int Ed Engl 2014;53(44): 11876-80.
203. Geers C, Gros G. Carbon dioxide transport and carbonic anhydrase in blood and muscle. Physiol Rev 2000;80(2): 681-715.
204. Liu Z, Radtke MA, Wong MQ, Lin KS, Yapp DT, Perrin DM. Dual Mode Fluorescent F-PET Tracers: Efficient Modular Synthesis of Rhodamine-[cRGD]-[F]-Organotrifluoroborate, Rapid, and High Yielding One-Step F-Labeling at High Specific Activity, and Correlated in Vivo PET Imaging and ex Vivo Fluorescence. Bioconjug Chem 2014.
205. Liu Z, Pourghiasian M, Benard F, Pan J, Lin KS, Perrin DM. Preclinical evaluation of a high-affinity 18F-trifluoroborate octreotate derivative for somatostatin receptor imaging. J Nucl Med 2014;55(9): 1499-505.
206. Sarathi Addy P, Saha B, Pradeep Singh ND, et al. 1,3,5-Trisubstituted benzenes as fluorescent photoaffinity probes for human carbonic anhydrase II capture. Chem Commun (Camb) 2013;49(19): 1930-2.
207. Ahlskog JK, Dumelin CE, Trussel S, Marlind J, Neri D. In vivo targeting of tumor-associated carbonic anhydrases using acetazolamide derivatives. Bioorg Med Chem Lett 2009;19(16): 4851-6.
208. Dubois L, Douma K, Supuran CT, et al. Imaging the hypoxia surrogate marker CA IX requires expression and catalytic activity for binding fluorescent sulfonamide inhibitors. Radiother Oncol 2007;83(3): 367-73.
209. Wilkinson BL, Bornaghi LF, Houston TA, Innocenti A, Supuran CT, Poulsen SA. A novel class of carbonic anhydrase inhibitors: glycoconjugate benzene sulfonamides prepared by "click-tailing". J Med Chem 2006;49(22): 6539-48.
210. Cecchi A, Hulikova A, Pastorek J, et al. Carbonic anhydrase inhibitors. Design of fluorescent sulfonamides as probes of tumor-associated carbonic anhydrase IX that inhibit isozyme IX-mediated acidification of hypoxic tumors. J Med Chem 2005;48(15): 4834-41.
211. Dubois L, Peeters S, Lieuwes NG, et al. Specific inhibition of carbonic anhydrase IX activity enhances the in vivo therapeutic effect of tumor irradiation. Radiother Oncol 2011;99(3): 424-31.

212. Liu Z, Radtke MA, Wong MQ, Lin KS, Yapp DT, Perrin DM. Dual mode fluorescent (18)F-PET tracers: efficient modular synthesis of rhodamine-[cRGD]2-[(18)F]-organotrifluoroborate, rapid, and high yielding one-step (18)F-labeling at high specific activity, and correlated in vivo PET imaging and ex vivo fluorescence. Bioconjug Chem 2014;25(11): 1951-62.
213. Vullo D, Franchi M, Gallori E, et al. Carbonic anhydrase inhibitors: inhibition of the tumor-associated isozyme IX with aromatic and heterocyclic sulfonamides. Bioorg Med Chem Lett 2003;13(6): 1005-9.
214. Thiry A, Ledecq M, Cecchi A, et al. Ligand-based and structure-based virtual screening to identify carbonic anhydrase IX inhibitors. Bioorg Med Chem 2009;17(2): 553-7.
215. Temperini C, Innocenti A, Scozzafava A, Parkkila S, Supuran CT. The coumarin-binding site in carbonic anhydrase accommodates structurally diverse inhibitors: the antiepileptic lacosamide as an example and lead molecule for novel classes of carbonic anhydrase inhibitors. J Med Chem 2010;53(2): 850-4.
216. Pastorekova S, Zatovicova M, Pastorek J. Cancer-associated carbonic anhydrases and their inhibition. Curr Pharm Des 2008;14(7): 685-98.
217. Carlin S, Khan N, Ku T, Longo VA, Larson SM, Smith-Jones PM. Molecular targeting of carbonic anhydrase IX in mice with hypoxic HT29 colorectal tumor xenografts. PLoS One 2010;5(5): e10857.
218. Rami M, Dubois L, Parvathaneni NK, et al. Hypoxia-targeting carbonic anhydrase IX inhibitors by a new series of nitroimidazole-sulfonamides/sulfamides/sulfamates. J Med Chem 2013;56(21): 8512-20.
219. Neri D, Supuran CT. Interfering with pH regulation in tumours as a therapeutic strategy. Nat Rev Drug Discov 2011;10(10): 767-77.
220. Lau J, Liu Z, Lin KS, et al. Trimeric Radiofluorinated Sulfonamide Derivatives to Achieve In Vivo Selectivity for Carbonic Anhydrase IX-Targeted PET Imaging. J Nucl Med 2015;56(9): 1434-40.
221. Casey JR, Morgan PE, Vullo D, Scozzafava A, Mastrolorenzo A, Supuran CT. Carbonic anhydrase inhibitors. Design of selective, membrane-impermeant inhibitors targeting the human tumor-associated isozyme IX. J Med Chem 2004;47(9): 2337-47.
222. Scozzafava A, Briganti F, Ilies MA, Supuran CT. Carbonic anhydrase inhibitors: synthesis of membrane-impermeant low molecular weight sulfonamides possessing in vivo selectivity for the membrane-bound versus cytosolic isozymes. J Med Chem 2000;43(2): 292-300.
223. Rami M, Cecchi A, Montero JL, et al. Carbonic anhydrase inhibitors: design of membrane-impermeant copper(II) complexes of DTPA-, DOTA-, and TETA-tailed sulfonamides targeting the tumor-associated transmembrane isoform IX. ChemMedChem 2008;3(11): 1780-8.
224. Rami M, Winum JY, Innocenti A, Montero JL, Scozzafava A, Supuran CT. Carbonic anhydrase inhibitors: copper(II) complexes of polyamino-polycarboxylamido aromatic/heterocyclic sulfonamides are very potent inhibitors of the tumor-associated isoforms IX and XII. Bioorg Med Chem Lett 2008;18(2): 836-41.
225. Dilworth JR, Pascu SI, Waghorn PA, et al. Synthesis of sulfonamide conjugates of Cu(II), Ga(III), In(III), Re(V) and Zn(II) complexes: carbonic anhydrase inhibition studies and cellular imaging investigations. Dalton Trans 2015;44(11): 4859-73.
226. Fani M, Andre JP, Maecke HR. 68Ga-PET: a powerful generator-based alternative to cyclotron-based PET radiopharmaceuticals. Contrast Media Mol Imaging 2008;3(2): 67-77.

227. Berry DJ, Ma Y, Ballinger JR, et al. Efficient bifunctional gallium-68 chelators for positron emission tomography: tris(hydroxypyridinone) ligands. Chem Commun (Camb) 2011;47(25): 7068-70.
228. Maecke HR, Hofmann M, Haberkorn U. (68)Ga-labeled peptides in tumor imaging. J Nucl Med 2005;46 Suppl 1: 172S-8S.
229. Mukai T, Suwada J, Sano K, Okada M, Yamamoto F, Maeda M. Design of Ga-DOTA-based bifunctional radiopharmaceuticals: two functional moieties can be conjugated to radiogallium-DOTA without reducing the complex stability. Bioorg Med Chem 2009;17(13): 4285-9.
230. Singh AN, Liu W, Hao G, et al. Multivalent bifunctional chelator scaffolds for gallium-68 based positron emission tomography imaging probe design: signal amplification via multivalency. Bioconjug Chem 2011;22(8): 1650-62.
231. Lin KS, Pan J, Amouroux G, et al. In vivo radioimaging of bradykinin receptor b1, a widely overexpressed molecule in human cancer. Cancer Res 2015;75(2): 387-93.
232. Burleigh A, McKinney S, Brimhall J, et al. A co-culture genome-wide RNAi screen with mammary epithelial cells reveals transmembrane signals required for growth and differentiation. Breast Cancer Research 2015;17.
233. Kassamali R, Sica DA. Acetazolamide: a forgotten diuretic agent. Cardiol Rev 2011;19(6): 276-8.
234. Carlin S, Zhang H, Reese M, Ramos NN, Chen Q, Ricketts SA. A comparison of the imaging characteristics and microregional distribution of 4 hypoxia PET tracers. J Nucl Med 2014;55(3): 515-21.
235. Lau J, Pan J, Zhang Z, et al. Synthesis and evaluation of (18)F-labeled tertiary benzenesulfonamides for imaging carbonic anhydrase IX expression in tumours with positron emission tomography. Bioorg Med Chem Lett 2014;24(14): 3064-8.
236. Sneddon D, Poulsen SA. Agents described in the Molecular Imaging and Contrast Agent Database for imaging carbonic anhydrase IX expression. J Enzyme Inhib Med Chem 2014;29(5): 753-63.
237. Peeters SG, Dubois L, Lieuwes NG, et al. [(18)F]VM4-037 MicroPET Imaging and Biodistribution of Two In Vivo CAIX-Expressing Tumor Models. Mol Imaging Biol 2015;17(5): 615-9.
238. Kohler G, Milstein C. Continuous cultures of fused cells secreting antibody of predefined specificity. Nature 1975;256(5517): 495-7.
239. Peters C, Brown S. Antibody-drug conjugates as novel anti-cancer chemotherapeutics. Biosci Rep 2015;35(4).
240. Larson SM, Carrasquillo JA, Cheung NK, Press OW. Radioimmunotherapy of human tumours. Nat Rev Cancer 2015;15(6): 347-60.
241. Seidel UJ, Schlegel P, Lang P. Natural killer cell mediated antibody-dependent cellular cytotoxicity in tumor immunotherapy with therapeutic antibodies. Front Immunol 2013;4: 76.
242. Lachmann P. Complement before molecular biology. Mol Immunol 2006;43(6): 496-508.
243. Gul N, van Egmond M. Antibody-Dependent Phagocytosis of Tumor Cells by Macrophages: A Potent Effector Mechanism of Monoclonal Antibody Therapy of Cancer. Cancer Res 2015;75(23): 5008-13.

244. Oosterwijk E, Ruiter DJ, Hoedemaeker PJ, et al. Monoclonal antibody G 250 recognizes a determinant present in renal-cell carcinoma and absent from normal kidney. Int J Cancer 1986;38(4): 489-94.
245. Oosterwijk-Wakka JC, Boerman OC, Mulders PF, Oosterwijk E. Application of monoclonal antibody G250 recognizing carbonic anhydrase IX in renal cell carcinoma. Int J Mol Sci 2013;14(6): 11402-23.
246. Chamie K, Klopfer P, Bevan P, et al. Carbonic anhydrase-IX score is a novel biomarker that predicts recurrence and survival for high-risk, nonmetastatic renal cell carcinoma: Data from the phase III ARISER clinical trial. Urol Oncol 2015;33(5): 204 e25-33.
247. Surfus JE, Hank JA, Oosterwijk E, et al. Anti-renal-cell carcinoma chimeric antibody G250 facilitates antibody-dependent cellular cytotoxicity with in vitro and in vivo interleukin-2-activated effectors. J Immunother Emphasis Tumor Immunol 1996;19(3): 184-91.
248. Ahlskog JK, Schliemann C, Marlind J, et al. Human monoclonal antibodies targeting carbonic anhydrase IX for the molecular imaging of hypoxic regions in solid tumours. Br J Cancer 2009;101(4): 645-57.
249. Xu C, Lo A, Yammanuru A, et al. Unique biological properties of catalytic domain directed human anti-CAIX antibodies discovered through phage-display technology. PLoS One 2010;5(3): e9625.
250. Chang DK, Moniz RJ, Xu Z, et al. Human anti-CAIX antibodies mediate immune cell inhibition of renal cell carcinoma in vitro and in a humanized mouse model in vivo. Mol Cancer 2015;14: 119.
251. Zatovicova M, Jelenska L, Hulikova A, et al. Carbonic anhydrase IX as an anticancer therapy target: preclinical evaluation of internalizing monoclonal antibody directed to catalytic domain. Curr Pharm Des 2010;16(29): 3255-63.
252. Abrahmsen L, Hoiden-Guthenberg I, Gunneriusson E. New polypeptides. Sweden, 2014.
253. Nuttall SD, Walsh RB. Display scaffolds: protein engineering for novel therapeutics. Curr Opin Pharmacol 2008;8(5): 609-15.
254. Vosjan MJ, Perk LR, Visser GW, et al. Conjugation and radiolabeling of monoclonal antibodies with zirconium-89 for PET imaging using the bifunctional chelate p-isothiocyanatobenzyl-desferrioxamine. Nat Protoc 2010;5(4): 739-43.
255. Buckley RG, Searle F. An efficient method for labelling antibodies with 111In. FEBS Lett 1984;166(1): 202-4.
256. Fairweather DS, Bradwell AR, Dykes PW, Vaughan AT, Watson-James SF, Chandler S. Improved tumour localisation using indium-111 labelled antibodies. Br Med J (Clin Res Ed) 1983;287(6386): 167-70.
257. Vallabhajosula S, Kuji I, Hamacher KA, et al. Pharmacokinetics and biodistribution of 111In- and 177Lu-labeled J591 antibody specific for prostate-specific membrane antigen: prediction of 90Y-J591 radiation dosimetry based on 111In or 177Lu? J Nucl Med 2005;46(4): 634-41.
258. Pan MH, Gao DW, Feng J, et al. Biodistributions of 177Lu- and 111In-labeled 7E11 antibodies to prostate-specific membrane antigen in xenograft model of prostate cancer and potential use of 111In-7E11 as a pre-therapeutic agent for 177Lu-7E11 radioimmunotherapy. Mol Imaging Biol 2009;11(3): 159-66.
259. Kong G, Johnston V, Ramdave S, Lau E, Rischin D, Hicks RJ. High-administered activity In-111 octreotide therapy with concomitant radiosensitizing 5FU chemotherapy for treatment of

neuroendocrine tumors: preliminary experience. Cancer Biother Radiopharm 2009;24(5): 527-33.
260. Costantini DL, Bateman K, McLarty K, Vallis KA, Reilly RM. Trastuzumab-resistant breast cancer cells remain sensitive to the auger electron-emitting radiotherapeutic agent 111In-NLS-trastuzumab and are radiosensitized by methotrexate. J Nucl Med 2008;49(9): 1498-505.
261. Williams SP. Tissue distribution studies of protein therapeutics using molecular probes: molecular imaging. AAPS J 2012;14(3): 389-99.
262. Mukai T, Namba S, Arano Y, et al. Synthesis and evaluation of a monoreactive DOTA derivative for indium-111-based residualizing label to estimate protein pharmacokinetics. J Pharm Pharmacol 2002;54(8): 1073-81.
263. Misri R, Saatchi K, Ng SS, Kumar U, Hafeli UO. Evaluation of (111)In labeled antibodies for SPECT imaging of mesothelin expressing tumors. Nucl Med Biol 2011;38(6): 885-96.
264. Fang J, Nakamura H, Maeda H. The EPR effect: Unique features of tumor blood vessels for drug delivery, factors involved, and limitations and augmentation of the effect. Adv Drug Deliv Rev 2011;63(3): 136-51.
265. Brouwers AH, van Eerd JE, Frielink C, et al. Optimization of radioimmunotherapy of renal cell carcinoma: labeling of monoclonal antibody cG250 with 131I, 90Y, 177Lu, or 186Re. J Nucl Med 2004;45(2): 327-37.
266. Brouwers A, Verel I, Van Eerd J, et al. PET radioimmunoscintigraphy of renal cell cancer using 89Zr-labeled cG250 monoclonal antibody in nude rats. Cancer Biother Radiopharm 2004;19(2): 155-63.
267. Cheal SM, Punzalan B, Doran MG, et al. Pairwise comparison of 89Zr- and 124I-labeled cG250 based on positron emission tomography imaging and nonlinear immunokinetic modeling: in vivo carbonic anhydrase IX receptor binding and internalization in mouse xenografts of clear-cell renal cell carcinoma. Eur J Nucl Med Mol Imaging 2014;41(5): 985-94.
268. Hoeben BA, Kaanders JH, Franssen GM, et al. PET of hypoxia with 89Zr-labeled cG250-F(ab')2 in head and neck tumors. J Nucl Med 2010;51(7): 1076-83.
269. Altai M, Perols A, Karlstrom AE, et al. Preclinical evaluation of anti-HER2 Affibody molecules site-specifically labeled with 111In using a maleimido derivative of NODAGA. Nucl Med Biol 2012;39(4): 518-29.
270. Ahlgren S, Wallberg H, Tran TA, et al. Targeting of HER2-expressing tumors with a site-specifically 99mTc-labeled recombinant affibody molecule, ZHER2:2395, with C-terminally engineered cysteine. J Nucl Med 2009;50(5): 781-9.
271. Stewart BN, Wild CP. World Cancer Report 2014. Lyon, France: International Agency for Research on Cancer, 2014.
272. McIntyre A, Patiar S, Wigfield S, et al. Carbonic anhydrase IX promotes tumor growth and necrosis in vivo and inhibition enhances anti-VEGF therapy. Clin Cancer Res 2012;18(11): 3100-11.
273. Siolas D, Hannon GJ. Patient-derived tumor xenografts: transforming clinical samples into mouse models. Cancer Res 2013;73(17): 5315-9.
274. Tentler JJ, Tan AC, Weekes CD, et al. Patient-derived tumour xenografts as models for oncology drug development. Nat Rev Clin Oncol 2012;9(6): 338-50.
275. Basavaraj S, Betageri GV. Can formulation and drug delivery reduce attrition during drug discovery and development-review of feasibility, benefits and challenges. Acta Pharm Sin B 2014;4(1): 3-17.

276. Laurence VM, Ward R, Dennis IF, Bleehen NM. Carbogen breathing with nicotinamide improves the oxygen status of tumours in patients. Br J Cancer 1995;72(1): 198-205.
277. Robinson SP, Howe FA, Stubbs M, Griffiths JR. Effects of nicotinamide and carbogen on tumour oxygenation, blood flow, energetics and blood glucose levels. Br J Cancer 2000;82(12): 2007-14.
278. Janssens GO, Rademakers SE, Terhaard CH, et al. Accelerated radiotherapy with carbogen and nicotinamide for laryngeal cancer: results of a phase III randomized trial. J Clin Oncol 2012;30(15): 1777-83.
279. Wulbrand C, Seidl C, Gaertner FC, et al. Alpha-particle emitting 213Bi-anti-EGFR immunoconjugates eradicate tumor cells independent of oxygenation. PLoS One 2013;8(5): e64730.
280. Mulford DA, Scheinberg DA, Jurcic JG. The promise of targeted {alpha}-particle therapy. J Nucl Med 2005;46 Suppl 1: 199S-204S.
281. Ercan MT, Caglar M. Therapeutic radiopharmaceuticals. Curr Pharm Des 2000;6(11): 1085-121.
282. O'Donoghue JA. Strategies for selective targeting of Auger electron emitters to tumor cells. J Nucl Med 1996;37(4 Suppl): 3S-6S.
283. O'Donoghue JA, Wheldon TE. Targeted radiotherapy using Auger electron emitters. Phys Med Biol 1996;41(10): 1973-92.
284. Krishnamurthy GT, Swailem FM, Srivastava SC, et al. Tin-117m(4+)DTPA: pharmacokinetics and imaging characteristics in patients with metastatic bone pain. J Nucl Med 1997;38(2): 230-7.
285. Srivastava SC. The role of electron-emitting radiopharmaceuticals in the palliative treatment of metastatic bone pain and for radiosynovectomy: applications of conversion electron emitter Tin-117m Braz Arch Biol Technol 2007;50: 49-62.
286. Srivastava SC, Atkins HL, Krishnamurthy GT, et al. Treatment of metastatic bone pain with tin-117m Stannic diethylenetriaminepentaacetic acid: a phase I/II clinical study. Clin Cancer Res 1998;4(1): 61-8.
287. Stevenson NR, St. George G, Simon J, et al. Methods of producing high specific activity Sn-117m with commercial cyclotrons. J Radioanal Nucl Chem 2015;305: 99-108.
288. Price EW, Orvig C. Matching chelators to radiometals for radiopharmaceuticals. Chem Soc Rev 2014;43(1): 260-90.
289. Atkins HL, Mausner LF, Srivastava SC, Meinken GE, Cabahug CJ, D'Alessandro T. Tin-117m(4+)-DTPA for palliation of pain from osseous metastases: a pilot study. J Nucl Med 1995;36(5): 725-9.
290. Holbein ME. Understanding FDA regulatory requirements for investigational new drug applications for sponsor-investigators. J Investig Med 2009;57(6): 688-94.
291. Stabin MG, Sparks RB, Crowe E. OLINDA/EXM: the second-generation personal computer software for internal dose assessment in nuclear medicine. J Nucl Med 2005;46(6): 1023-7.
292. Lam K, Chan C, Done SJ, Levine MN, Reilly RM. Preclinical pharmacokinetics, biodistribution, radiation dosimetry and acute toxicity studies required for regulatory approval of a Clinical Trial Application for a Phase I/II clinical trial of (111)In-BzDTPA-pertuzumab. Nucl Med Biol 2015;42(2): 78-84.

Appendix

This appendix lists awards received, and publications that were published, were accepted, or currently under review, for my graduate degree.

AWARDS AND SCHOLARSHIPS

2015	BC Cancer Agency Lloyd Skarsgard Research Excellence Prize
2015	UBC Interdisciplinary Graduate Student Network Travel Award
2014	UBC Faculty of Graduate Studies Travel Award
2014	World Molecular Imaging Congress Student Travel Stipend
2014	UBC Faculty of Medicine Graduate Award
2014-2017	UBC Four Year Doctoral Fellowship
2014-2016	CIHR Doctoral Award - Frederick Banting and Charles Best Canada Graduate Scholarships
2013	Canadian Cancer Society Research Institute Travel Award
2013	CIHR Institute of Cancer Research Travel Award
2013	BC Cancer Foundation John Jambor Knowledge Fund
2013	International Symposium on Radiopharmaceutical Sciences Travel Bursary
2013	CIHR Institute Community Support Travel Award
2013	UBC Interdisciplinary Oncology Program Travel Award
2013	UBC College for Interdisciplinary Studies Graduate Award
2012-2016	RIX Family Leading Edge Student Award
2011	UBC Graduate Entrance Scholarship

PUBLICATIONS

Published Refereed Journal Articles

1) **Lau J**†, Zhang Z†, Jenni S, Kuo HT, Liu Z, Vullo D, Supuran CT, Dedhar S, Lin KS, Bénard F. "PET imaging of carbonic anhydrase IX expression in HT29 tumour xenograft mice with ^{68}Ga-labeled benzenesulfonamides," *Molecular Pharmaceutics,* 2016, 13(3): 1137–1146.
2) Zhang Z, Jenni S, Zhang C, Merkens H, **Lau J**, Liu Z, Perrin DM, Bénard F, Lin KS. "Synthesis and evaluation of ^{18}F-trifluoroborate derivatives of triphenlyphosphonium for myocardial perfusion imaging," *Bioorganic & Medicinal Chemistry Letters,* 2016; 26(7):1675-1679.
3) Zhang Z, **Lau J**, Kuo HT, Zhang C, Hundal-Jabal N, Colpo N, Bénard F, Lin KS. "Synthesis and evaluation of ^{18}F-labeled 4-nitrobenzyl derivatives for imaging tumor hypoxia with positron emission tomography: comparison of 2-[^{18}F]fluoroethyl carbonate and 2-[^{18}F]fluoroethyl carbamate," *Bioorganic & Medicinal Chemistry Letters*, 2016; 26(2): 584-588.
4) **Lau J**†, Liu Z†, Lin KS, Pan J, Zhang Z, Vullo D, Supuran CT, Perrin DM, Bénard F. "Trimeric radiofluorinated sulfonamide derivatives to achieve in vivo selectivity for carbonic anhydrase IX-targeted PET imaging," *Journal of Nuclear Medicine*, 2015; 56(9): 1434-1440.

5) Lin KS, Amouroux G, Pan J, Zhang Z, Jenni S, **Lau J**, Liu Z, Hundal-Jabal N, Colpo N, Bénard F. "Comparative Studies of Three Gallium-68-labeled [des-Arg^{10}]Kallidin Derivatives for Imaging Bradykinin B1 Receptor Expression with Positron Emission Tomography," *Journal of Nuclear of Medicine*, 2015; 56(4): 622-627.
6) Lin KS, Pan J, Amouroux G, Turashvili G, Mesak F, Hundal-Jabal N, Pourghiasian M, **Lau J**, Jenni S, Aparicio SJ, Bénard F. "*In vivo* imaging of bradykinin receptor B1 using radiolabeled peptides," *Cancer Research*, 2015; 75(2): 387- 393.
7) Liu Z, Amouroux G, Zhang Z, Pan J, Hundal-Jabal N, Colpo N, **Lau J**, Perrin DM, Bénard F, Lin KS. "^{18}F-Trifluoroborate Derivatives of [Des-Arg^{10}]Kallidin for Imaging Bradykinin B1 Receptor Expression with Positron Emission Tomography," *Molecular Pharmaceutics*, 2015; 12(3): 974-982.
8) Liu Z, Pourghiasian M, Radtke A, **Lau J**, Pan J, Dias GM, Yapp D, Lin KS, Bénard F, Schaffer P, Perrin DM. "An Organotrifluoroborate for Broadly Applicable One-step ^{18}F-labelling," *Angewandte Chemie International Edition*, 2014; 53(44): 11876-11880.
9) **Lau J**, Pan J, Zhang Z, Hundal N, Liu Z, Bénard F, Lin KS. "Synthesis and evaluation of ^{18}F-labeled tertiary sulfonamides for imaging carbonic anhydrase IX expression in tumours with positron emission tomography," *Bioorganic & Medicinal Chemistry Letters*, 2014; 24(14): 3064-3068.
10) Pan J, **Lau J**, Mesak F, Hundal N, Pourghiasian M, Liu Z, Bénard F, Shoukat D, Supuran C, Lin KS. "Synthesis and evaluation of 18F-labeled carbonic anhydrase IX inhibitors for imaging with positron emission tomography," *Journal of Enzyme Inhibition and Medicinal Chemistry*, 2014; 29(2): 249-255.
11) Pan J, Pourghiasian M, Hundal N, **Lau J**, Bénard F, Shoukat D, Lin KS. "2-[18F]Fluoroethanol and 3-[18F]fluoropropanol: facile preparation, biodistribution in mice, and their application as nucleophiles in the synthesis of [18F]fluoroalkyl aryl ester and ether PET tracers," *Nuclear Medicine and Biology*, 2013; 40(6): 850-857.
12) Li Y, Liu Z, Harwig CW, Pourghiasian M, **Lau J**, Lin KS, Schaffer P, Bénard F, Perrin DM. "18F-Click Labeling of a Bombesin Antagonist with an Alkyne-18F-ArBF3-: in vivo PET Imaging of Tumors Expressing the GRP-Receptor," *American Journal of Nuclear Medicine and Molecular Imaging*, 2013; 3(1):57-70.

Manuscript in Review

13) Zhang C, Pan J, Lin KS, Dude I, **Lau J**, Merkens H, Jenni S, Guérin B, Bénard F. "Targeting the neuropeptide Y1 receptor for cancer imaging by positron emission tomography using novel novel truncated peptides," submitted to *Molecular Pharmaceutics*.
14) Croucher DR, Iconomou M, Hastings JF, Kennedy SP, Shearer RF, McKenna J, Wan A, **Lau J**, Aparicio S, Saunders DN. "Bimolecular complementation affinity purification (BiCAP) reveals dimer-specific protein interactions for ERBB2 dimers," submitted to *Science Signalling*.
15) Zhang Z, Kuo HT, **Lau J**, Jenni S, Zhang C, Zeisler J, Bénard F, Lin KS. "Design, synthesis and evaluation of ^{18}F-labeled bradykinin B1 receptor-targeting small molecules for PET imaging," submitted to *Bioorganic & Medicinal Chemistry Letters*.

16) Zhang Z, Zhang C, **Lau J**, Colpo N, Bénard F, Lin KS. "One-step synthesis of 4-[^{18}F]fluorobenzyltriphenylphosphonium cation for imaging with positron emission tomography," submitted to *Journal of Labelled Compounds and Radiopharmaceuticals*.

† Denotes shared first author

Accepted Abstracts

1) **Lau J**, Kuo HT, Pan J, Zhang C, Lin KS, Bénard F. "Synthesis and evaluation of a ^{68}Ga-labeled affibody for imaging carbonic anhydrase IX expression," accepted to The Annual Congress of the European Association of Nuclear Medicine, Barcelona, Spain, 2016.
2) Kuo HT, Pan J, Merkens H, **Lau J**, Zhang C, Liu Z, Perrin DM, Bénard F, Lin KS. "Synthesis and comparative evaluation of three ^{18}F-AmBF$_3$ derivatives of Glu-ureido-Lys for imaging PSMA expression in prostate cancer with positron emission tomography," submitted to The Annual Congress of the European Association of Nuclear Medicine, Barcelona, Spain, 2016.
3) **Lau J**, Pan J, Kuo HT, Hundal-Jabal N, Lin KS, Bénard F. "Exploration of hyperbranched polyglycerols as an imaging scaffold for targeting CA-IX expression with SPECT," accepted to The Annual Meeting of Society of Nuclear Medicine and Molecular Imaging, San Diego, California, USA, 2016.
4) Pan J, Nakai M, **Lau J**, Storr T, Bénard F, Lin KS. "Design, synthesis, and evaluation of technetium-99m labeled sulfocoumarin and benzenesulfonamide derivatives for imaging carbonic anhydrase IX expression with single-photon emission computed tomography," accepted to The Annual Meeting of Society of Nuclear Medicine and Molecular Imaging, San Diego, California, USA, 2016.
5) Zhang Z, Jenni S, Zhang C, **Lau J**, Merkens H, Liu Z, Perrin DM, Bénard F, Lin KS. "Synthesis and comparative evaluation of four ^{18}F-trifluoroborate derivatives of triphenylphosphonium for myocardial perfusion imaging," accepted to The Annual Meeting of Society of Nuclear Medicine and Molecular Imaging, San Diego, California, USA, 2016.
6) Zhang C, Pan J, Lin KS, Dude I, **Lau J**, Merkens H, Jenni S, Guérin B, Bénard F. "Targeting the neuropeptide Y1 receptor with novel truncated peptides using positron emission tomography," accepted to The Annual Meeting of Society of Nuclear Medicine and Molecular Imaging, San Diego, California, USA, 2016.
7) Kuo HT, Pan J, Lin KS, Merkens H, **Lau J**, Zhang C, Liu Z, Perrin DM, Bénard F. "Synthesis and Evaluation of ^{18}F-AmBF$_3$-PSMA Derivatives as PET Imaging Agents for Prostate Cancer," accepted to The Annual Meeting of Society of Nuclear Medicine and Molecular Imaging, San Diego, California, USA, 2016.
8) Kuo HT, Pan J, Zhang C, Rousseau J, **Lau J**, Bénard F, Lin KS. "A novel AmBF$_3$-succinimide prosthetic group for facile ^{18}F-labeling of biomolecules," accepted to The Annual Meeting of Society of Nuclear Medicine and Molecular Imaging, San Diego, California, USA, 2016.
9) Kuo HT, Zhang Z, Jenni S, **Lau J**, Zhang C, Bénard F, Lin KS. "Synthesis and evaluation of an ^{18}F-labeled bradykinin B1 receptor-targeting small molecule for PET imaging," accepted to The Annual Meeting of Society of Nuclear Medicine and Molecular Imaging, San Diego, California, USA, 2016.

10) Rousseau J, Dias GM, Ramogida CF, **Lau J**, English W, Vuckovic M, Lin KS, Schaffer P, Bénard F. "Optimizing conditions to minimize antibody requirements for ^{89}Zr radiolabeling," accepted to The Annual Meeting of Society of Nuclear Medicine and Molecular Imaging, San Diego, California, USA, 2016.
11) Lin KS, Pan J, Zhang Z, **Lau J**, Jenni S, Hundal-Jabal N, Colpo N, Liu Z, Perrin DM, Bénard F. "Application of the ^{18}F-^{19}F isotope exchange reaction on an ammoniomethyl trifluoroborate moiety for the design of tumor-targeting PET tracers," accepted to the International Chemical Congress of Pacific Basin Societies, Honolulu, Hawaii, 2015.
12) Zhang Z, **Lau J**, Colpo N, Bénard F, Lin KS. "Radiosynthesis and evaluation of 2-[^{18}F]fluoroethyl 4-nitrobenzyl carbonate for imaging tumor hypoxia with positron emission tomography," accepted to the European Association of Nuclear Medicine, Hamburg, Germany, 2015
13) **Lau J**, Pan J, Zhang C, Zhang Z, Colpo N, Lin KS, Bénard F. "Synthesis and biological evaluation of a novel ^{18}F-labeled sulfonamide for imaging carbonic anhydrase IX expression with PET," accepted to the World Molecular Imaging Congress, Honolulu, Hawaii, 2015.
14) Zhang Z, **Lau J**, Colpo N, Bénard F, Lin KS. "Radiosynthesis and evaluation of 4-nitrobenzyl N-2-[18F]fluoroethyl carbamate for imaging tumor hypoxia with positron emission tomography," accepted to the World Molecular Imaging Congress, Honolulu, Hawaii, 2015.
15) Zhang C, Pan J, **Lau J**, Colpo N, Jenni S, Park S, Lin KS, Bénard F. "In vitro and in vivo evaluation of a novel BVD15 analogue for neuropeptide Y receptor imaging with positron emission tomography," accepted to the World Molecular Imaging Congress, Honolulu, Hawaii, 2015.
16) Dias GM, **Lau J**, Jenni S, Colpo N, Lin KS, Bénard F. "Antibody radiolabeing: Improving tumour contrast in vivo by blocking the neonatal Fc receptor with IgG," accepted to the World Molecular Imaging Congress, Hawaii, USA, 2015.
17) Pan J, **Lau J**, Hundal-Jabal N, Zhang Z, Zhang C, Bénard F, Lin KS. "Synthesis and evaluation of a ^{18}F-labled 1,3,5-triazine-substituted benzenesulfonamide for imaging carbonic anhydrase IX expression in tumors with positron emission tomography," accepted to the World Molecular Imaging Congress, Hawaii, USA, 2015.
18) **Lau J**, Liu Z, Pan J, Zhang Z, Perrin DM, Lin KS, Bénard F. "Trimeric ^{18}F-AmBF_3-sulfonamides for imaging carbonic anhydrase IX expression," accepted to Society of Nuclear Medicine and Molecular Imaging Annual Meeting, Baltimore, USA, 2015.
19) Perrin DM, Lin KS, Benard F, Yapp DT, Liu Z, Pourghiasian M, **Lau J**, Zhang Z, Jenni S. "A new ^{18}F-RBF_3 radioprosthetic for one step aqueous labeling of peptides and other ligands: meeting the challenge of radiosynthetic ease and preclinical impact i.e. high specific activity and high T:NT ratios," accepted to Society of Nuclear Medicine and Molecular Imaging Annual Meeting, Baltimore, USA, 2015.
20) **Lau J**, Pan J, Mesak F, Hundal N, Pourghiasian M, Dias G, Dedhar S; Supuran C, Bénard F, Lin, KS. "Hyperbranched polyglycerols as a vector for molecular targeted imaging of carbonic anhydrase IX expression with SPECT," accepted to World Molecular Imaging Conference, Seoul, Korea, 2014
21) **Lau J**, McDonald PC, Dias GM, Dedhar S, Lenferink A, Lin KS, O'Connor M, Bénard F."SPECT imaging with novel ^{111}In labeled anti-carbonic anhydrase IX monoclonal

antibodies:comparison between internalizing and non-internalizing antibodies," accepted to Society of Nuclear Medicine and Molecular Imaging Annual Meeting, St. Louis, USA, 2014.

22) **Lau J**, Zhang Z, Hundal-Jabal N, Liu Z, Bénard F, Lin KS. "Synthesis and evaluation of monomeric, dimeric and trimeric benzenesulfonamide derivatives for imaging carbonic anhydrase IX with PET," accepted to Society of Nuclear Medicine and Molecular Imaging Annual Meeting, St. Louis, USA, 2014.
23) Dias GM, Zhang Z, **Lau J**, Bénard F, Lin KS. "Diethylenetriaminetetrahydroxamic acid: a potential chelator for labeling antibody with Zr-89 for PET imaging," accepted to Society of Nuclear Medicine and Molecular Imaging Annual Meeting, St. Louis, USA, 2014.
24) Dias GM, **Lau J**, Bénard F, Lin KS. "99mTc(CO)3-DTPA-ABSA2: synthesis and evaluation for imaging carbonic anhydrase IX expression in hypoxic tumors with SPECT," accepted to Society of Nuclear Medicine and Molecular Imaging Annual Meeting, St. Louis, USA, 2014.
25) **Lau J**, Pan J, Zhang Z, Hundal N, Liu Z, Bénard F, Lin KS. "Synthesis and evaluation of 18Flabeled tertiary sulfonamides for imaging carbonic anhydrase IX expression in tumors with positron emission tomography," accepted to European Symposium on Radiopharmacy and Radiopharmaceuticals, Pamplona, Spain, 2014.
26) **Lau J**, Pan J, Zhang Z, Hundal N, Jenni S, Bénard F, Lin KS. "Radiosynthesis and biological evaluation of 3-[18F]fluoroabiraterone for imaging CYP17A1 expression with positron emission tomography," accepted to European Symposium on Radiopharmacy and Radiopharmaceuticals, Pamplona, Spain, 2014.
27) **Lau J**, Pan J, Hundal N, Pourghiasian M, Liu Z, Bénard F, Lin KS. "Radiosynthesis and biological evaluation of an 18F-labeled tertiary substituted benzenesulfonamide for targeting carbonic anhydrase IX with positron emission tomography," accepted to Canadian Cancer Research Conference, Toronto, Canada, 2013.
28) Zhang Z, **Lau J**, Hundal N, Pourghiasian M, Jenni S, Dias G, Liu Z, Bénard F, Lin KS. "Radiosynthesis and biological evaluation of 68Ga-NOTGA-(AEBSA)3 for diagnostic molecular-targeted imaging of carbonic anhydrase IX in cancers," accepted to Canadian Cancer Research Conference, Toronto, Canada, 2013.
29) Liu Z, Amouroux G, Pan J, Pourghiasian M, Hundal N, **Lau J**, Zhang Z, Bénard F, Lin KS, Perrin D. "The first PET imaging study of an ^{18}F-labeled B1R-targeting ligands via a "kit" [^{18}F]B-F bond formation," accepted to Canadian Cancer Research Conference, Toronto, Canada, 2013
30) **Lau J**, Zhang Z, Hundal N, Algara T, Liu Z, Bénard F, Lin KS. "Radiosynthesis and biological evaluation of ^{68}Ga-DOTA-AEBSA for imaging carbonic anhydrase IX expression with positron emission tomography," accepted to World Molecular Imaging Conference, Savannah, Georgia, USA, 2013.
31) Liu Z, **Lau J**, Pan J, Pourghiasian M, Algara T, Perrin D, Bénard F, Lin KS. "Facile synthesis and biological evaluation of an ^{18}F-labeled 4-(2-minoethyl)benzenesulfonamide (AEBS) trimer for imaging carbonic anhydrase IX expression with positron emission tomography," accepted to World Molecular Imaging Conference, Savannah, Georgia, USA, 2013.

32) Liu Z, Amouroux G, Pan J, Pourghiasian M, Hundal N, **Lau J**, Dias G, Zhang Z, Bénard F, Lin KS, Perrin D. "First biological evaluation and facile radiosynthesis of an F-18 labeled peptide for imaging bradykinin B1 receptor expression with positron emission tomography," accepted to World Molecular Imaging Conference, Savannah, Georgia, USA, 2013.
33) Pourghiasian M, Pan J, **Lau J**, Dias G, Hundal N, Liu Z, Bénard F, Lin KS. "Trapping of 2-[18F]fluoroacetyl-CoA in the cell: a promising strategy for imaging enzymatic activity with positron emission tomography," accepted to World Molecular Imaging Conference, Savannah, Georgia, USA, 2013.
34) Pourghiasian M, Pan J, Hundal N, **Lau J**, Bénard F, Lin KS. "Zr-75 cell line: a promising tumor model for imaging somatostatin receptor SST2a expression in breast cancer by positron emission tomography," accepted to World Molecular Imaging Conference, Savannah, Georgia, USA, 2013.
35) Zhang Z, Pourghiasian M, Pan J, **Lau J**, Hundal N, Bénard F, Lin KS. "Synthesis and evaluation of 21-[18F]fluoro-17α-hydroxyprogesterone for imaging the activity of CYP17A1 with positron emission tomography," accepted to Annual Congress of the European Association of Nuclear Medicine, Lyon, France, 2013.
36) Pan J, Mesak F, Pourghiasian M, Hundal N, **Lau J**, Bénard F, Lin KS. "Successful imaging of human bradykinin B1 receptor expression in tumor xenografts in mice with positron emission tomography," *Journal of Nuclear Medicine*, 2013; 54: 19P.
37) Pan J, **Lau J**, Hundal N, Pourghiasian M, Dedhar S, Supuran C, Bénard F, Lin KS. "Synthesis and evaluation of an 18F-labeled sulfonamide inhibitor for imaging carbonic anhydrase IX expression in cancers," *Journal of Nuclear Medicine,* 2013; 54: 215P.
38) Pourghiasian M, Pan J, **Lau J**, Hundal N, Jenni S, Bénard F, Lin KS. "2-[18F]Fluoroethanol and 3-[18F]fluoropropanol: facile preparation, biodistribution in mice, and their application in the radiosynthesis of PET tracers," *Journal of Nuclear Medicine*, 2013; 54: 221-222P.
39) Pan J, Mesak F, Pourghiasian M, Hundal N, **Lau J**, Bénard F, Lin KS. "Design, synthesis and evaluation of a gallium-68-labeled bradykinin derivative for imaging B1 receptor expression in cancers with positron emission tomography," *Journal of Labelled Compounds and Radiopharmaceuticals*, 2013; 56: S393.
40) **Lau J**, Pan J, Mesak F, Hundal N, Pourghiasian M, Dias G, Dedhar S; Supuran C, Bénard F, Lin, KS. "Synthesis and evaluation of an 18F-labelled coumarin derivative for imaging carbonic anhydrase IX expression in cancers with Positron Emission Tomography," *Journal of Labelled Compounds and Radiopharmaceuticals*, 2013; 56: S405.

Oral Presentations

1) "Imaging carbonic anhydrase IX expression in hypoxic niches with different antigen recognition molecules". Thursday Oncology Training Seminars, BC Cancer Research Centre, Vancouver, Canada, December 4th 2015.
2) "Trimeric ^{18}F-AmBF$_3$-sulfonamides for imaging carbonic anhydrase IX expression". Society of Nuclear Medicine and Molecular Imaging Annual Meeting, Baltimore, USA, June 10th 2015.

3) “Targeting tumour microenvironment: Development of carbonic anhydrase IX imaging agents”. Thursday Oncology Training Seminars, BC Cancer Research Centre, Vancouver, Canada, November 20th 2014.
4) “Synthesis and evaluation of monomeric, dimeric and trimeric benzenesulfonamide derivatives for imaging carbonic anhydrase IX with PET”. Society of Nuclear Medicine and Molecular Imaging Annual Meeting, St. Louis, USA, June 10th 2014.
5) “Targeting carbonic anhydrase IX expression non-invasively using PET/CT and SPECT/CT modalities”. Thursday Oncology Training Seminars, BC Cancer Research Centre, Vancouver, Canada, May 1st 2014.
6) “Synthesis and evaluation of 18F-labeled tertiary sulfonamides for imaging carbonic anhydrase IX expression in tumors with positron emission tomography”. European Symposium on Radiopharmacy and Radiopharmaceuticals, Pamplona, Spain, April 25th 2014.
7) “Radiosynthesis and biological evaluation of 3-[18F]fluoroabiraterone for imaging CYP17A1 expression with positron emission tomography”. European Symposium on Radiopharmacy and Radiopharmaceuticals, Pamplona, Spain, April 25th 2014.
8) “Molecular Targeted Imaging of Carbonic Anhydrase IX with Positron Emission Tomography”. Knowledge Translation Seminar, BC Cancer Research Centre, Vancouver, Canada, April 4th 2013.